Fast crashes of the central electron temperature during ECCD experiments at W7-X

vorgelegt von
M.Sc.
Marco Zanini
ORCID: 0000-0002-8717-1106

von der Fakultät II - Mathematik und Naturwissenschaften
der Technischen Universität Berlin
zur Erlangung des akademischen Grades
Doktor der Naturwissenschaften
- Dr.rer.nat. -
genehmigte Dissertation

Promotionsausschuss:
Vorsitzende: Prof. Dr. Kathy Lüdge
Gutachter: Prof. Dr. Dieter Breitschwerdt
Gutachter: Prof. Dr. Robert Wolf
Gutachter: Prof. Dr. Hartmut Zohm
Tag der wissenschaftlichen Aussprache: 16. September 2021

Berlin, 2021

"Ci hanno davvero preso tutto!"
Offlaga Disco Pax - *Tatranky*

Abstract

Electron Cyclotron Current Drive (ECCD) experiments have been conducted at the superconducting stellarator Wendelstein 7-X, with the aim of assessing the capabilities of ECCD for strikeline control operation and the stability of the magnetic configuration to localised current. The toroidal current in a stellarator like W7-X evolves on a timescale of tens of seconds, thus moving the strikelines on the divertor as the current itself (and therefore the rotational transform) evolves. The strikeline control is crucial for future operations, in order not to damage the components which are not suited to withstand high heat fluxes. However, during ECCD experiments, sawtooth-like crashes were observed. These sawtooth-like crashes are characterised by a fast drop of the central electron temperature, as a result of the hot core expulsion.

ECCD calculations performed with the ray-tracing code TRAVIS show that the rotational transform $\iota\!\!\!-$ is modified in such a way that low order rational values are crossed.

The analysis of experimental data shows that up to two different types of crashes, with different affected volumes and amplitudes, can be recognised. The joint analysis of Electron Cyclotron Emission (ECE) and soft x-ray tomography (XMCTS) shows that the temperature crash is preceded by a fast displacement of the plasma core, consistent with a $(m, n) = (1, 1)$ mode. The size of the crashes is not constant and a dependence on the toroidal current was found. The toroidal current evolves and shifts the resonance outwards, thus making the instability affecting a larger plasma volume. Sawtooth-like crashes are found in different magnetic configurations and for different heating schemes.

A very limited amount of ECCD experiments with relatively high toroidal current is related to a strong decrease of the confined energy and in some cases even to the fast and premature termination of the experiment. It was not possible to fully understand the dynamics of these events, however several indications point in the direction of a strong increase of impurities in the plasma, probably due to the ionisation of impurities caused by the expelled core. The energy loss is mainly caused by radiation and did not threaten the device integrity.

Kurzzusammenfassung

Experimente zur Untersuchung des Elektronen-Zyklotron-Stromtrieb (ECCD) wurden am supraleitenden Stellarator Wendelstein 7-X durchgeführt, um die Möglichkeiten des Stromtriebs für die Strikelinekontrolle und die Stabilität der magnetischen Konfiguration in Bezug auf lokalisierten Stromtrieb zu bewerten. Der toroidale Strom in einem Stellarator, wie dem W7-X, entwickelt sich in einer Zeitspanne von zehn Sekunden. In dieser Zeit werden die Strikelines auf dem Divertor vom entstandenen Strom bzw. vor der sich ändernden Rotationstransformation bewegt. Die Kontrolle der Strikelines ist entscheidend für zukünftige Experimente, um die Komponenten, die nicht höheren Wärmeflüssen widerstehen können, nicht zu beschädigen. Sogenannte Sawtooth Crashes wurden während den ECCD-Experimenten beobachtet. Sie sind an einem Abfall der Elektronentemperatur und damit verbunden an dem Auswurf des heißen Zentralplasmas zu erkennen.

Die Berechnungen des ECCD wurden von dem Ray-Tracing Code TRAVIS durchgeführt. Sie zeigen, dass die Rotationstransformation mit Stromtrieb niedrig rationale Werte annimmt.

Zwei Typen von Sawtooth Crashes können unterschieden werden. Sie weisen unterschiedliche Amplituden und betroffene Volumina auf. Die Analyse von Elektronen-Zyklotron-Emission (ECE) und Soft X-ray-Tomographie zeigt, dass der Elektronentemperaturenabfall einer schnellen Verschiebung des Zentralplasmas vorausgeht, was im Einklang mit einer $(m, n) = (1, 1)$ Mode ist. Die Amplitude der Crashes ist nicht konstant, sondern hängt vom toroidalen Strom ab. Der sich mit der Zeit entwickelnde toroidale Strom verschiebt die Resonanzposition nach außen, weshalb das betroffene Plasmavolumen zunimmt. Sawtooth Crashes wurden in verschiedenen magnetischen Konfigurationen und mit verschiedenen Heizkonfigurationen beobachtet.

Eine sehr begrenzte Anzahl von ECCD-Experimenten mit relativ hohem toroidalen Plasmastrom war mit einer starken Abnahme der Plasmaenergie und in einigen Fällen sogar mit einem schnellen und vorzeitigen Abbruch des

Experiments verbunden. Eine schlüssige Erklärung ist bisher nicht möglich, aber Hinweise deuten darauf hin, dass der Auswurf des Zentralplasmas und die damit verbundene Wandbelastung zu einem unkontrollierten Anstieg von Verunreinigungen und damit verbunden von Strahlungsleistung führt, die dann das Plasma beenden.

Contents

Chapter 1.

Introduction

1.1. Nuclear Fusion

The atomic age starts in 1945 with the Trinity test and the following nuclear bombings of Hiroshima and Nagasaki. The first nuclear fission power plant generated electricity in 1954 and several generations of power plants have been conceived during the years. Nonetheless, nuclear fission has not been able to fulfil the promise of a clean, safe and inexhaustible source of energy. A series of incidents, the most infamous being the Černobyl and Fukushima ones, along with the unsolved problem of radioactive waste storage, led several countries to reduce or dismiss their nuclear programs. Therefore, in the framework of an increasing global demand of CO2-free energy, the development of alternative sources is to be pursued. Nuclear fusion could play an important role as a safe, constant and almost inexhaustible source of energy [1].

Nuclear fusion reactions are among the most important phenomena in the universe, being the energy source of stars and having played a fundamental role in the nucleosynthesis. Nuclear fusion consists in binding together two light nuclei to create an heavier nucleus and, for exothermic reactions, the difference of binding energy is equal to the produced energy. Being the Coulomb repulsion between nuclei very strong, it is possible to fuse two particles by reaching kinetic energies high enough to overcome the potential energy barrier.

The advantages of a fusion power plant with respect to a fission one are numerous. The nuclear fusion technology does not rely on the chain reaction of the fuel, allowing for a safer control of the process and reactions do not produce long-lived products as for nuclear fission[1]. On the other hand, several parameters, such as particle energy, density and confinement, need to be fulfilled at the same time, which makes the development of a fusion power plant challenging.

On Earth, two main approaches have been developed to confine and ignite particles, in order to reach reactor relevant parameters: inertial and magnetic confinement. The first approach will not be treated in this work, but, for completeness, suffice it to say that it relies on the heating and compression of solid pellet via powerful lasers or particle beams [2]. The high kinetic energies and densities allow the fuel to fuse. The second approach consists in the confinement of an hot plasma, by means of magnetic fields. Although several exothermic fusion reactions are known, the $\mathrm{D} + \mathrm{T} \rightarrow^4 \mathrm{He} + n$ reaction is the easiest to achieve in terms of cross-section and required ion temperatures. For this reason the first generation of commercial reactor is foreseen to operate with a mixture of D-T. Deuterium is largely present in water, while tritium is a $\beta-$ unstable radioactive isotope with a short lifetime (12 years). Tritium breeding from a lithium blanket is a viable option for reactors: thanks to the interaction between lithium and fusion produced neutrons, tritium can be produced on-site.

In order to be used as an energy source, the fusion fuel not only needs to be energetic enough to allow fusion reactions to take place, but it also needs to be sufficiently abundant and confined for a sufficiently long time. Confining properties can also be described by the so called *triple product*, defined as $n\tau_{\mathrm{E}}T$, where n is the ion density, τ_{E} is the energy confinement time (ratio between the plasma energy and the input power) and T is the plasma ion temperature. The triple product can be used to estimate under which plasma properties *ignition* can be reached. In this condition, the plasma itself, through the produced α particles is able to compensate the losses and sustain the nuclear reactions. For D-T fuel[3] ignition is reached if $n\tau_{\mathrm{E}}T \approx 3 \times 10^{21}\ \mathrm{m}^{-3}$keVs, for ion temperature in the range of $10-20$keV. A high triple product requires therefore good and stable confining properties and efficient plasma heating methods. These factors are briefly reviewed in the following chapters.

[1] However, neutronic reactions can still cause the activation of the device structure.

1.2. Toroidal Magnetic Confinement

A plasma can be described as a globally neutral but locally charged system. Therefore, charged particles will gyrate around magnetic field lines. The most promising magnetic confinement approach is represented by toroidal devices, in which the magnetic field is closed. Due to the curvature and inhomogeneities of the magnetic field, the toroidal magnetic field (B_{tor}) is not sufficient for plasma confinement and an additional poloidal field component (B_{pol}) is necessary. The configuration results in helical magnetic field lines around the torus and lying on the so called *magnetic surfaces*. The magnetic field line winding can be expressed in terms of the *rotational transform* $\iota/2\pi = \bar{\iota}$:

$$\frac{\iota}{2\pi} = \frac{\mathrm{d}\psi}{\mathrm{d}\Phi} \tag{1.1}$$

where ψ,Φ are respectively the poloidal and toroidal magnetic flux. According to [4], equation (1.1) can be decomposed into two terms, respectively created by external magnetic fields ($\bar{\iota}_{\mathrm{cf}}$) or toroidal currents ($\bar{\iota}_{\mathrm{curr}}$)

$$\bar{\iota} = \bar{\iota}_{\mathrm{cf}} + \bar{\iota}_{\mathrm{curr}} = -\frac{S_{12}}{S_{11}} + \frac{\mu_0 I(r)_{\mathrm{tor}}}{S_{11}\Phi'} \tag{1.2}$$

where $I(r)_{\mathrm{tor}}$ is the toroidal current current enclosed in a surface of radius r, S_{ij} are the elements of the susceptance matrix, which depends on the external coil geometry and Φ' is the radial derivative of the toroidal flux. The existence of finite values of the rotational transform is a direct consequence of the superposition of a toroidal and a poloidal magnetic field. The rotational transform can be seen as an indicator of the number of poloidal transits a magnetic field lines completes during a toroidal transit. Irrational rotational transform values mean that a single magnetic field would transit around the magnetic surface infinite times before reaching the position where it started. Conversely, a magnetic field line lying on a magnetic surface with a rational value would reach the starting position in m poloidal and n toroidal transit. Surfaces with a rational value of the rotational transform ($\bar{\iota} = n/m$) are sensitive to perturbations, since they are not ergodically covered by the magnetic field lines. These surfaces are labelled as *resonant magnetic surfaces*.

Different toroidal configurations have been developed, differing mainly in the way magnetic fields are produced. The most promising configurations

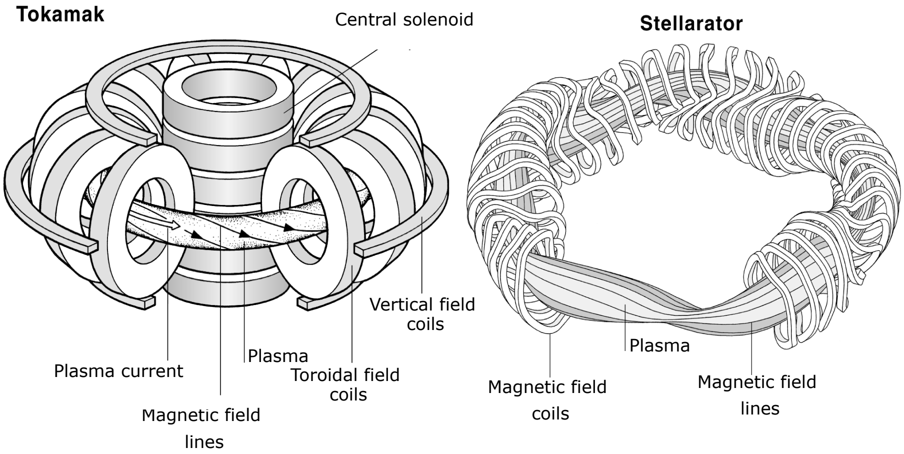

Figure 1.1.: Schematic representation of a tokamak (left) and a (modular) stellarator (right) (© IPP).

are the *tokamak* and the *stellarator*. A tokamak (figure 1.1, left) presents an axisymmetric configuration of the magnetic field. The toroidal magnetic field is generated by external coils, while the poloidal field is generated by an inductive toroidal current flowing in the plasma, which is generated by a central solenoid. In a tokamak the toroidal current plays a two-fold role: the toroidal current heats up the plasma, especially at low temperatures and being $S_{12} \sim 0$ (equation 1.2) it is necessary for plasma confinement. The necessity of sustaining the toroidal current makes the tokamak a pulsed operation machine, although several experimental efforts are pursued to maintain the confinement through non-inductive currents, which can be generated by external systems [5] and by the plasma itself due to neoclassical effects (*bootstrap current*) [6, 7]. Additionally, the toroidal current is a source of free energy which can destabilise the plasma, thus limiting the achievable performances.

Stellarators (figure 1.1, right) instead do not rely on a toroidal current for plasma confinement and can operate in steady state without any current drive. Both the poloidal and the toroidal magnetic fields are created by the external coils, which results in a non-axisymmetric configuration. Early stellarators had the magnetic field created by a set of toroidal coils and a set of helical windings, but this approach has almost been abandoned since it was demonstrated they possess a high neoclassical transport and there are generally unconfined particle orbits [8]. In modern stellarator the helical and toroidal coils are combined together in one system of modular coils and resulting in a more complex coil geometry than in tokamaks. This approach gives the possibility to optimise the coil design for the magnetic field to fulfil a series of requirements, such as the achievement of a lower neoclassical transport [9]. It was estimated by A. Boozer that the number of degrees of freedom for non-axisymmetric configurations is about 50 (conversely, it is about 4 for axisymmetric configurations) [10]. Two main types of configuration optimised to improve the confinement of collisionless and trapped particles are the *quasi-symmetric* stellarator and the *quasi-isodynamic* stellarator. An excellent review is provided by [11]. Wendelstein 7-X (W7-X) is quasi-isodynamic stellarator and will be introduced in section 1.5. In the next sections, we will describe how an equilibrium is achieved and the conditions under which the plasma stability can be lost.

1.3. Magnetohydrodynamic

A plasma can be described as a quasi-neutral fluid which interacts with electromagnetic fields. This assumption is valid when the system is close to the thermodynamic equilibrium, i.e. when the spatial scales of the system are large compared to the mean free path of the particles composing the fluid. This assumption is not always fulfilled along the magnetic field lines, since the collisionality in a hot plasma is very small and therefore the mean free path becomes large. However, for the direction perpendicular to the magnetic field $\mathbf{B}$, the mean free path is about the Larmor radius r_{L} [2], which is typically very small, making the fluid approximation valid. The system can, therefore, be investigated in the framework of the magnetohydrodynamic (MHD), which is "a fluid model that describes the macroscopic equilibrium and stability properties of a plasma" [12] and can be studied by combining Euler's equations, Maxwell's equations and the Ohm's law. If we neglect some terms, such as the high-frequency response in the Ampere's law or corrective factors in the Ohm's law and we add the adiabatic equation of state, we can write the set of equations as follows:

[2] $r_{\mathrm{L}} = v_{\perp}/\omega_c$, where $v_{\perp}$ is the thermal velocity perpendicular to the magnetic field and ω_c is the cyclotron frequency.

$$\frac{\partial \rho}{\partial t} + \nabla \cdot (\rho \mathbf{v}) = 0 \tag{1.3}$$

$$\rho \left[\frac{\partial \mathbf{v}}{\partial t} + (\mathbf{v} \cdot \nabla)\mathbf{v} \right] = -\nabla p + \mathbf{j} \times \mathbf{B} \tag{1.4}$$

$$\mathbf{E} + \mathbf{v} \times \mathbf{B} = \eta \mathbf{j} \tag{1.5}$$

$$\nabla \times \mathbf{B} = \mu_0 \mathbf{j} \tag{1.6}$$

$$\nabla \cdot \mathbf{B} = 0 \tag{1.7}$$

$$\nabla \times \mathbf{E} = -\frac{\partial \mathbf{B}}{\partial t} \tag{1.8}$$

$$\frac{\mathrm{d}}{\mathrm{d}t} \left(\frac{p}{\rho^\gamma} \right) = 0 \tag{1.9}$$

where ρ is the mass density, $\mathbf{v}$ the fluid velocity, $\mathbf{j}$ the current density, $\mathbf{B}$ and $\mathbf{E}$ the magnetic and electric field.

Considering a stationary state ($\partial/\partial t \to 0$) without flows ($\mathbf{v} = 0$), equation (1.4) becomes

$$\nabla p = \mathbf{j} \times \mathbf{B} \tag{1.10}$$

which describes how the magnetic force balances the force given by the plasma pressure. An important consequence is that $\mathbf{B} \cdot \nabla p = 0$ and $\mathbf{j} \cdot \nabla p = 0$, which means the magnetic field lines and current lines lie on surfaces of constant pressure. The magnetic field is generated by external coils and by the toroidal current (if present, see equation (1.2)) but it is modified by the plasma currents that arise to maintain the force balance (equation 1.10). The current $\mathbf{j}$ has components both perpendicular and parallel to the magnetic field and can be expressed as $\mathbf{j} = j_\parallel \hat{\mathbf{b}} + \mathbf{j}_\perp$, where $\hat{\mathbf{b}}$ is the unit vector in the direction of the magnetic field. The perpendicular component is necessary for producing a magnetic force $\mathbf{j} \times \mathbf{B} = \nabla p$ and can be expressed as $\mathbf{j}_\perp = (\mathbf{B} \times \nabla p) / B^2$. In addition, the current $\mathbf{j}$ has to fulfil the condition $\nabla \cdot \mathbf{j} = 0$ which generally requires an additional parallel current $j_\parallel^{\mathrm{PS}}$ (known as *Pfirsch-Schlüter* current), proportional to the pressure gradient. The parallel current is given by two terms $j_\parallel = j_\parallel^{\mathrm{PS}} + \langle j_\parallel B \rangle \mathbf{B}/(B^2)$, where the second term on the right hand side represents the Ohmic current, the bootstrap current and any non-inductively driven current and brackets $\langle ... \rangle$ indicate the average over the magnetic surface [11]. The Pfirsch-Schlüter current depends on the plasma pressure and has a dipole character (the direction of the current is different for inboard and outboard sides), which generates a vertical magnetic field that shifts the central magnetic surfaces towards the outboard side of the torus (*Shafranov shift*). A large Shafranov shift limits the maximum achievable plasma pressure.

The solution of equation 1.10 consists of a function whose curves describe the magnetic surfaces of the system. An example is provided in figure 1.2, where the magnetic surfaces of the stellarator W7-X at three different toroidal positions are plotted. As it was previously mentioned, stellarators are not axisymmetric, but have instead a discrete symmetry. The lack of a continuous symmetry has important consequences on the magnetic surface topology and the so-called *magnetic islands* are created in correspondence of the resonant surfaces [11, 13]. Magnetic islands (zoom in figure 1.3) are

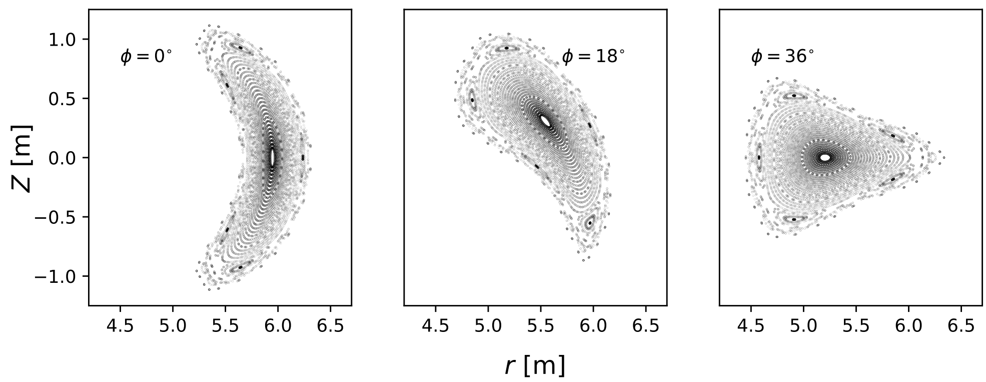

Figure 1.2.: Examples of magnetic surfaces of W7-X at different toroidal locations ($\phi = 0°$, $\phi = 18°$, $\phi = 36°$).

topologically separated by a surface called *separatrix*, with the two parts of it meeting at the *X-point*. The magnetic lines within the separatrix are nested around a new magnetic axis, called *O-point*, which generally lies at the same position of the resonant surface. In a magnetic island, different radial regions of the plasma are connected along the island field lines. Since the transport is much larger along a field line than across it, the connection of magnetic lines at different radial position creates larger heat and particle fluxes and thus a reduction of the confinement [14]. Flat temperature and density profiles are generally detected inside the islands. Additionally, islands at different resonant surfaces can also overlap and create a region of ergodic magnetic field, in which the magnetic surfaces are destroyed and confinement is strongly reduced.

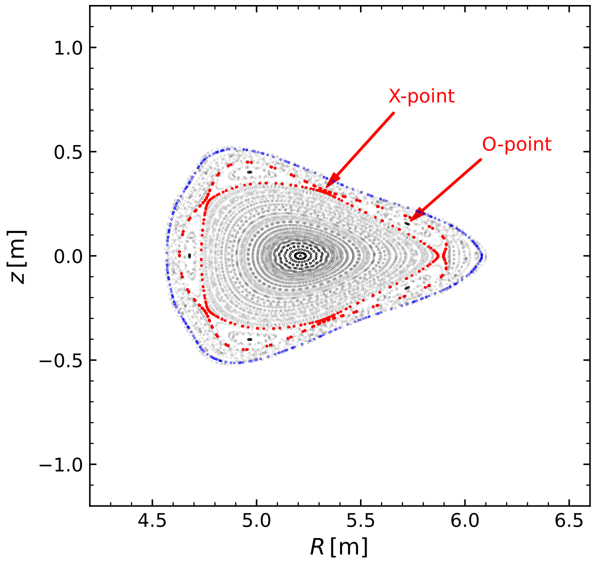

Figure 1.3.: Sketch of an island chain at W7-X. The islands are divided from the confined region by the separatrix (red).

If we combine equations (1.5) and (1.8), we obtain

$$\frac{\partial \mathbf{B}}{\partial t} = \frac{\eta}{\mu_0}\nabla^2\mathbf{B} + \nabla \times (\mathbf{v} \times \mathbf{B}) \tag{1.11}$$

which describes the dynamics of magnetic and fluid velocity fields.

If the resistivity η of the plasma can be neglected, the system can be described in the framework of *ideal* MHD and magnetic field evolves on the Alfvén timescale ($\tau_A = a\sqrt{\mu_0\rho}/B$)[3]. It can be proved that the total magnetic flux within an ideal MHD plasma is conserved [12]. An important consequence is that the magnetic flux is *frozen*, which means the topology of

[3] a, ρ and B are the typical scale of the system, the mass density and the magnetic field

the magnetic field cannot change. The approximation of ideal MHD is valid for a wide range of parameters and applications. Nevertheless, situations where the resistivity has to be taken into account can be encountered and such as in regions where the term $\nabla \times (\mathbf{v} \times \mathbf{B})$ becomes negligible with respect to the term $\frac{\eta}{\mu_0}\nabla^2\mathbf{B}$. In this latter case, the resistivity allows the magnetic field lines to diffuse on the resistive time scale $(\tau_\eta = \mu_0 a^2/\eta)$[4] and a rearrangement of the magnetic topology is possible. This process is known as *magnetic reconnection* and can occur in regions where the magnetic field changes sign. In a toroidal plasma, a similar situation occurs due the shear of the magnetic field in proximity of a resonant surface with $\iota = n/m$ [14] and it is schematically presented in 1.4. The magnetic field lines on the resonant surface define a helix. Considering the poloidal angle θ and the toroidal angle ϕ, it possible to define the coordinate $\chi = \theta - (m/n)\phi$, which is an angular coordinate orthogonal to the helix. The projection of the equilibrium magnetic field onto this orthogonal direction can be written as the helical magnetic field $B^* \approx B_{\mathrm{pol}}(r) - B_{\mathrm{pol}}(r_{\mathrm{res}})(r/r_{\mathrm{res}})$, where r_{res} it the radial position of the resonant surface. It can be seen that $B^* > 0$ if $r < r_{\mathrm{res}}$, $B^* < 0$ if $r > r_{\mathrm{res}}$ and $B^* \to 0$ for $r \to r_{\mathrm{res}}$. In proximity of the resonant surface the helical magnetic field B^* changes sign (1.4 (a)) and, due to the presence of a finite resistivity η, the frozen magnetic flux condition does not hold any more and the rearrangement of the magnetic field lines is possible. This generally requires a perturbation with the same helicity of the resonant surface.

The effects a perturbation can have on a plasma is discussed in the next section.

1.3.1. Plasma Instabilities

The existence of an equilibrium does not reflect its stability. A hot plasma contains several sources of free energy and the system itself will approach a condition of stability with lower stored energy. This means that plasmas are subject to instabilities that can have different effects on the plasma performance [15]. Plasma instabilities can lower plasma performance or, in the case of violent instabilities, such as disruptions, can lead to the total loss of the plasma. Conversely, instabilities can also be used to improve plasma

[4] where η is the plasma resistivity

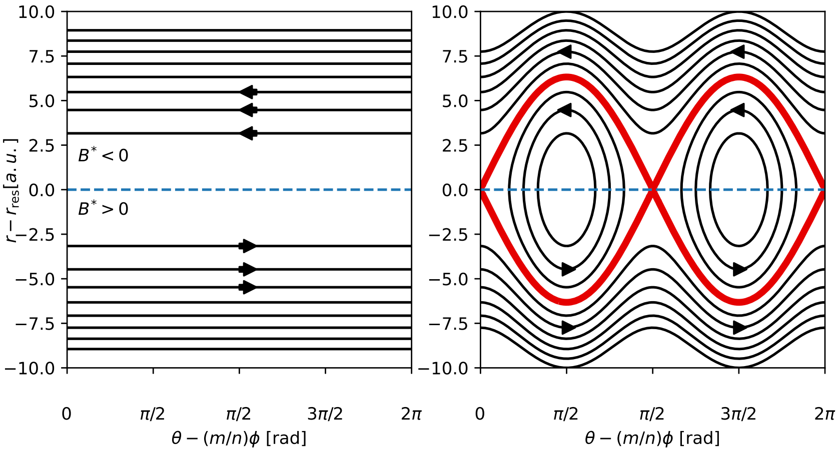

Figure 1.4.: Sketch of the magnetic reconnection. The x- and the y-axes represent the helical angle and the distance from resonance. The left plot shows that the helical field B^* changes sign in proximity of a resonance. In presence of a finite resistivity, the rearrangement of the magnetic field lines is possible resulting in the formation of magnetic islands.

performance, such as by avoiding impurity accumulation in the core.

Instabilities are related to perturbations of the plasma equilibrium and can be characterised by mode frequency (ω), poloidal (m),toroidal (n) mode numbers, growth rate (γ) and displacement (ξ). The mode frequency ω indicates the rotation frequency of the perturbation, which rotates poloidally and/or toroidally, the helicity being defined by the mode numbers m and n [16]. The growth rate indicates how fast the instability grows or decays and the displacement ξ represents the shift of the magnetic field lines from the equilibrium, which can be written as:

$$\xi(r, \theta, \phi, t) = \xi_r \cdot \cos(m\theta - n\phi + \omega t) \cdot e^{\gamma t} \tag{1.12}$$

where ξ_r is the radial displacement component.

The plasma stability can be assessed using the energy principle [17]. Here an overview is presented in order to highlight the major drives for the instabilities. A proper discussion can be found in [12, 14] and references therein. It is possible to study the stability of the system under a small perturbation such that $A \rightarrow A_0 + A_1$ where the subscripts 0 and 1 represent the unperturbed and perturbed values. It is possible to define the displacement vector as:

$$\boldsymbol{\xi}(r) = \int_0^t \mathbf{v_1} \mathrm{d}\tau \tag{1.13}$$

where $\mathbf{v_1}$ is the perturbation of the velocity field. The energy change caused by a displacement $\boldsymbol{\xi}$ and the force $\mathbf{F}(\xi)$ arising from it is defined as:

$$\delta W = -\frac{1}{2} \int_0^t \boldsymbol{\xi} \cdot \mathbf{F} \mathrm{d}\,\tau. \tag{1.14}$$

The system is *stable* if $\delta W > 0$ and *unstable* if $\delta W < 0$. The term δW is given by the sum of two components $\delta W = \delta W_{\mathrm{vac}} + \delta W_{\mathrm{plasma}}$, which represent the energy increase in the vacuum magnetic field due to the displacement and the contribution to the plasma energy given by the displacement. They can be written as:

$$\delta W_{\mathrm{vacuum}} = \int_{\mathrm{V}} \frac{\mathbf{B}^2_{\mathrm{vacuum}}}{2\mu_0} \mathrm{d}V \tag{1.15}$$

$$\begin{aligned}\delta W_{\mathrm{plasma}} = \frac{1}{2} \int_{\mathrm{V}} [|\mathbf{B_1}_\perp|^2/\mu_0 + (\mathbf{B_0}^2)/\mu_0 |\nabla \cdot \xi_\perp + 2\xi_\perp \cdot \kappa|^2 + \gamma p_0 |\nabla \cdot \xi|^2 + \\ - 2(\xi_\perp \cdot \nabla p_0)(\kappa \cdot \xi_\perp) - j_\parallel (\xi_\perp \times \hat{\mathbf{B}}) \cdot \mathbf{B_1}_\perp \mathrm{d}V\end{aligned} \tag{1.16}$$

where $\kappa = (\hat{\mathbf{B}} \cdot \nabla)\hat{\mathbf{B}}$ is the curvature of the equilibrium magnetic field $\mathbf{B_0} = B_0 \hat{\mathbf{B}}$ and the subscripts ($\|$) and ($\perp$) refer to the direction of $\mathbf{B_0}$. The terms in the first line of 1.16 are always non negative and therefore have a stabilising effect. They represent the energy required to bend the magnetic field, to compress the magnetic field and to compress the plasma. The terms in the second line of 1.16 can be negative and drive the plasma unstable. The component $-2(\xi_\perp \cdot \nabla p_0)(\kappa \cdot \xi_\perp)$ is related to pressure gradient, while the component $j_\parallel(\xi_{perp} \times \hat{\mathbf{B}}) \cdot \mathbf{B_1}_\perp$ is related to the plasma current parallel to the magnetic field.

If the first term is dominant, the instability is said to be *pressure driven*, while in the second case it is defined as *current driven*.

The term $\delta W_{\mathrm{plasma}}$ in equation (1.16) was obtained by the linearisation of the ideal MHD equations. Non-ideal terms, such as resistivity, can influence the stability condition and can destabilise a mode that was predicted to be ideal MHD stable. Therefore plasma instabilities can be *ideal* or *non-ideal*, depending on whether they would occur even if the plasma were perfectly conducting. Ideal instabilities evolve on the Alfvén timescale τ_A and are generally characterised by a fast movement of the plasma column and magnetic surface distortion. Resistive instabilities evolves on the resistive timescale τ_η slower than Alfvén timescale and may results in rearrangement of the magnetic field lines and creation of magnetic islands. A typical ideal instability is the *kink instability* [18, 19], named after the kinking effect of the magnetic surfaces and of the plasma boundary. Typical non-ideal current driven instabilities in toroidal devices are the *tearing modes* (TM) [20] and *neoclassical tearing modes* (NTM) [21], which result in magnetic reconnection and formation of magnetic islands. A sketch of the magnetic surface perturbation due to an internal ideal kink and a tearing mode is depicted in figure 1.5.

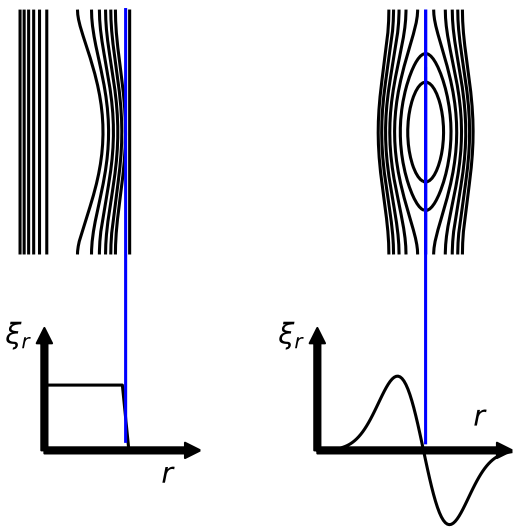

Figure 1.5.: Sketch of the perturbed magnetic surfaces,the radial component of the displacement ξ_r for an internal $(m, n) = (1, 1)$ ideal kink and tearing mode. The internal ideal kink ξ_r is non zero within $\iota\!\!\!- = 1$ and zero outside. For the tearing mode, ξ_r changes sign.

Good MHD stability is a crucial parameter for every machine. Instabilities cannot only hamper the plasma performances but can also damage the device itself. In the following, we will briefly discuss two phenomena related to plasma instability: sawtooth crashes and disruptions.

1.3.2. Sawtooth instability

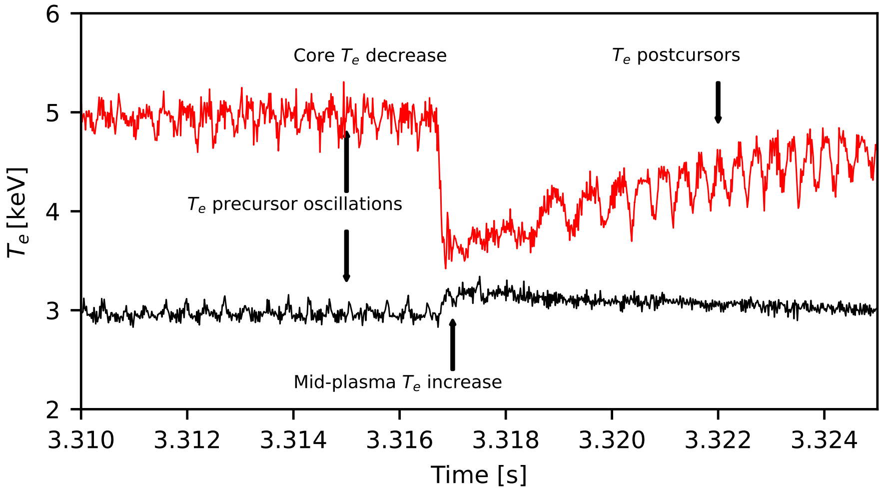

Figure 1.6.: Example of a sawtooth crash. The red time trace represents the central electron temperature T_e and the black one represents electron temperature in the mid-plasma region. The sawtooth is characterised by a fast crash of T_e and a small increase in the mid-plasma T_e. Sawtooth crashes can be preceded by T_e oscillations (*precursors*). T_e oscillations can also be present after the crash (*postcursors*).

The sawtooth instability is a periodic relaxation of the plasma core temperature and density [22, 23]. An example is shown in figure 1.6. Sawteeth are characterised by a fast collapse of the central temperature and a small temperature increase in the external region and are often preceded by a $(m, n) = (1, 1)$ precursor MHD mode activity. The first theoretical model to explain these oscillations was proposed by Kadomtsev in 1975 [24] in which a $(m, n) = (1, 1)$ kink is destabilised due to the presence of a $\iota\!\!\!- = 1$ magnetic surface in the plasma and drives magnetic reconnection between magnetic surfaces with the same helicity. Due to the magnetic reconnection,

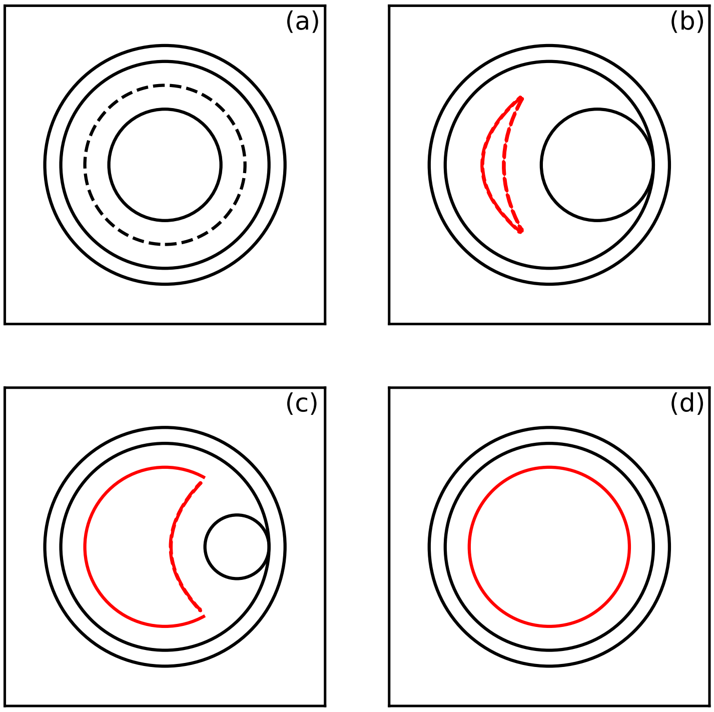

Figure 1.7.: Sketch of the Kadomtsev's model. (b) The growth of the island displaces the core. The island grows (c) until the reconnection process is completed (d).

a magnetic island is created (b) and the core is displaced inside the $\iota = 1$ surface. The island grows (c) until full reconnection between the old core and the outer part is completed (d). The O-point of the magnetic islands becomes the new magnetic axis and a flat temperature profile is obtained in the centre and being the core expelled. The rotational transform at the magnetic axis relaxes to unity. According to this model, the crash time is on the order of $\tau_C \sim (\tau_\eta \tau_\mathrm{A})^{1/2}$, where τ_A is the Alfvén time and τ_η the resistive time. Initially, the observed crash times were in agreement with estimated τ_C, but it turned out that data from larger tokamaks could not be explained by the Kadomtsev model.

Several corrections have been proposed, in order to include different effects and mechanism such as resistive two fluid MHD [25], collisionless effects [26], magnetic stochastisation [27], chaos [28], triggering of secondary instabilities [29].

Another issue is the assumption of complete reconnection. Several experiments have measured $\iota\!\!\!- > 1$ throughout the whole sawtooth crash. This measurement is consistent with the observation of the so-called *postcursors*, i.e. electron temperature and/or electron density fluctuations after the crash with the same mode numbers of the precursors (figure 1.6). The postcursor existence indicates the reconnection process stopped before the core has been completely expelled. Additionally, it has to be noted that the condition $\iota\!\!\!- > 1$ is not often sufficient for the instability onset. An heuristic model [30] was successfully developed by Porcelli. According to this model, several factors (such as trapped ions, diamagnetic rotation and fast ions) can contribute to the stabilisation or destabilisation of the instability. A review regarding the sawtooth physics can be found in [31, 32].

Sawtooth physics and dynamics is of concern for the nuclear fusion devices. Small amplitude sawteeth with high period can be beneficial since they might have a positive impact on impurity accumulation [33]. Conversely, large amplitude sawteeth can strongly decrease plasma performances by flattening and reducing the core temperature, can provide a seeding for NTMs [34, 35] or can couple with $m > 1$ harmonics, thus extending the perturbation to the plasma edge and causing loss of plasma energy at each event [30]. For this reason the understanding of the trigger conditions is crucial for tokamaks operations. Localised non-inductive current, like Electron Cyclotron Current Drive (ECCD, chapter 1.4.3), is a common tool used for the suppression of strong sawteeth. Since ECCD is very localised, it can change the rotational transform in the core, thus reducing the amplitude of the sawteeth. Sawtooth oscillations have already been observed in several current-carrying stellarators.

Stellarator MHD instabilities play a minor role than in tokamaks. This occurs due to a lower net toroidal current and to the possibility of optimising the magnetic field, in order to assess good MHD stability properties. For instance, it is either possible to avoid low order rational values (such as in Wendelstein 7-X) or to have an high shear (such as in the Large Helical Device (LHD)). Nevertheless non-inductive currents, be it the intrinsic bootstrap current or external applied current drive, can locally modify the profile of the rotational transform, thus making the configuration subject to MHD instabilities. Examples of sawtooth-like activity has been observed in LHD [36], TJ-II [37] and Wendelstein 7-AS [38].

1.3.3. Disruptions

Disruptions are events in which the plasma confinement is lost [23]. Disruptions have long been observed in tokamaks and pose a hard operational limit for certain plasma parameters, such as I_{tor} and n, thus constraining the operational space. Disruptions can have different causes [39], although they generally result in the same process which eventually ends the plasma discharge. Disruptions in tokamaks are generally initiated by a specific event, such as the growth of MHD modes, the reaching of the density limit [40] and so on. Whatever the cause, the so-called thermal quench phase occurs, in which the temperature decreases and the plasma volume shrinks. The shrinking causes an increase in the destabilising current gradient inside the $\iota\!\!-= 1/2$ surface, which triggers instabilities [23]. Finally, the plasma confinement is destroyed in a short time. The sudden temperature drop causes in turn a sudden increase in the plasma resistance and therefore of the toroidal electric field. The increased electric field may accelerate electrons to relativistic energies (*runaway electrons*), which can damage the machine wall. Additionally, the fast dissipation of the plasma energy and current is the main cause of concerns, as it can induce strong electromagnetic forces on the vessel. In fact, during this process the vertical stability can be lost [41] and the plasma column is vertically displaced. The plasma column comes in contact with the vessel, thus producing a thermal stress and driving large poloidal currents in the vessel itself. This in turn generates strong $\mathbf{j} \times \mathbf{B}$ forces, which can potentially damage the device. In tokamaks, active control is performed both to avoid disruptions and to mitigate their effects on the device.

Stellarators, conversely, do not rely on I_{tor} for the plasma confinement, which is assured by the external magnetic coils and therefore the I_{tor} can be orders of magnitude smaller. For this reason disruption-like events are not routinely observed [42]. An example of disruptive events is given by W7-AS [38, 43], in which strong MHD modes were induced by means of a large I_{tor}, leading to the plasma loss. It has to be noted that in most of the cases, being I_{tor} several order of magnitudes lower than that of comparable size tokamaks, the induced electromagnetic forces are extremely reduced, thus limiting the potential damages in case of a sudden dissipation of I_{tor}.

1.4. Plasma Heating

Plasma needs to be heated up to about 10 keV for fusion reactions to occur. In tokamaks, an important contribution is provided by the inductive current, heating the plasma through Ohmic dissipation. However, since the plasma resistivity scales with $T_e^{-3/2}$, the plasma becomes less resistive as the temperature increases, thus making the ohmic heating less effective and leading to the requirement for external heating systems.[5]. External heating systems are regularly used in modern tokamaks and stellarators. A brief description is provided in this chapter, while a detailed treatment can be found in [23, 45].

- **Neutral beam injection** is based on the acceleration and injection of neutral particles into the plasma. Injected particles are ionised due to collisions within the plasma and transfer their energy to the plasma itself until they are thermalised. The electron heating is dominant for high injected particle energies. Then, as the beam ions are slowed down, the heating is transferred to the plasma ions. The energy of the injected beams depends on the properties of the device. The injection can occur perpendicular or tangential to the magnetic field. Tangential injection can also be used to drive non inductive current in the plasma.

- **Ion cyclotron resonance heating** (ICRH) relies on electromagnetic waves with frequencies in the range of the ion cyclotron frequency (ω_{ci}), generally between 30 and 120 MHz. Waves are injected from the outboard part of the torus, where the magnetic field strength has its minimum and then propagate as a fast magnetosonic waves until the ion resonance condition is reached. For a single ion species plasmas the injected frequency has to match the second ion cyclotron harmonic. Another possibility is given by the so-called *minority heating* scheme which occurs in a two ion species plasma, with the resonance condition depending on the ratio of the two species. Wave launchers are generally placed inside the vessel, facing the plasma.

[5] Compact experiments at high B in which the Ohmic heating is envisaged to play a major role in reaching ignition conditions have been proposed. An example is given in [44].

- **Lower hybrid** waves are produced by *klystrons* at frequencies from $1-8$ GHz in a tangential direction with respect to the magnetic field, although, due to the accessibility condition, only off-axis heating is possible. Energy is ceded due to *Landau damping.* According to this phenomenon, an electron travelling parallel to the magnetic field with a velocity equal to the phase velocity of the wave will be accelerated by the electric field of the wave itself. Lower hybrid waves are mainly used to drive current in the plasma.

- **Electron cyclotron resonance heating** consists on the injection of electromagnetic waves at the electron cyclotron resonance frequency. Microwave beams are generated by means of *gyrotrons* (see [46] for a review). Electrons are heated directly,then transfer their energy to ions through collisions. Since ECRH is the main heating method of W7-X a more extensive description is provided below.

1.4.1. Electron cyclotron resonance heating and current drive

In this section, we provide a brief summary of wave propagation in a magnetised plasma, in order to highlight the main features of the electron cyclotron resonance heating. A full treatment regarding the physics of waves in plasma can be found in [47].

The frequency range used for ECRH is $10-200$ GHz. In this range the ion contribution to dispersion and absorption can be neglected. Let us consider the propagation of a plane wave into the plasma. The electric field of a plane monochromatic wave can be expressed as:

$$\mathbf{E}(\mathbf{r},t) = \hat{\mathbf{E}}(\mathbf{k},\omega)\exp(i\mathbf{k}\cdot\mathbf{r} - \omega t). \tag{1.17}$$

In order to obtain the dispersion relation for such a perturbation, let us consider the following Maxwell's equations:

$$\nabla\times\mathbf{E} = -\frac{\partial\mathbf{B}}{\partial t} \quad , \quad \nabla\times\mathbf{B} = \mu_0\left(\mathbf{j} + \epsilon_0\frac{\partial\mathbf{E}}{\partial t}\right). \tag{1.18}$$

This combination yields:

$$\nabla\times(\nabla\times\mathbf{E}) = -\frac{1}{c^2}\frac{\partial^2\mathbf{E}}{\partial t^2} - \mu_0\frac{\partial\mathbf{j}}{\partial t} \tag{1.19}$$

where the relation $\mu_0\epsilon_0 = 1/c^2$ was used. Using the Ohm's law ($\mathbf{j}(\omega) = \sigma(\omega)\cdot\mathbf{E}(\omega)$) and from equation 1.17 we obtain:

$$\mathbf{k}\times(\mathbf{k}\times\hat{\mathbf{E}}) = -\frac{\omega^2}{c^2}\hat{\mathbf{E}} - \mathrm{i}\omega\mu_0\sigma(\omega)\cdot\hat{\mathbf{E}} = -\frac{\omega^2}{c^2}\boldsymbol{\epsilon}(\omega)\hat{\mathbf{E}} \tag{1.20}$$

where $\boldsymbol{\epsilon}(\omega) = \mathbf{1} + \mathrm{i}\sigma(\omega)/\omega\epsilon_0$ is the dielectric tensor. Using the formalism developed by Stix [47] and considering only the electron contribution, the dielectric tensor can be written as:

$$\boldsymbol{\epsilon} = \begin{pmatrix} S & -iD & 0 \\ iD & S & 0 \\ 0 & 0 & P \end{pmatrix} \tag{1.21}$$

where

$$S \equiv \frac{1}{2}(R+L)\ , \quad D \equiv \frac{1}{2}(R-L) \tag{1.22}$$

and

$$R \equiv 1 - \frac{\omega_{\mathrm{pe}}^2}{\omega^2}\left(\frac{\omega}{\omega-\omega_{\mathrm{pe}}}\right)\ ,\ L \equiv 1 - \frac{\omega_{\mathrm{pe}}^2}{\omega^2}\left(\frac{\omega}{\omega+\omega_{\mathrm{pe}}}\right)\ ,\ P \equiv 1 - \frac{\omega_{\mathrm{pe}}^2}{\omega^2} \tag{1.23}$$

where $\omega_{\mathrm{pe}} = \sqrt{(n_e e^2/\epsilon_0 m_e)}$ is the electron plasma frequency. We emphasize again that these quantities refer to a plasma in which the contribution of ions and collisions has been neglected. Introducing $\mathbf{N} = \mathbf{k}c/\omega$ and defining θ as the angle between the mangetic field $B = \hat{\mathbf{z}}B_0$ and N, the equation becomes

$$\begin{pmatrix} S - N^2\cos^2\theta & -iD & N^2\cos\theta\sin\theta \\ iD & S - N^2 & 0 \\ N^2\cos\theta\sin\theta & 0 & P - N^2\sin^2\theta \end{pmatrix}\begin{pmatrix} E_x \\ E_y \\ E_z \end{pmatrix} = 0 \tag{1.24}$$

Equation (1.24) represents the general dispersion relation for waves in a magnetised plasma. The solution is given by the values for which the determinant is zero:

$$AN^4 - BN^2 + C = 0 \tag{1.25}$$

where

$$A = S\sin^2\theta + P\cos^2\theta \tag{1.26}$$

$$B = RL\sin^2\theta + PS(1+\cos^2\theta) \tag{1.27}$$

$$C = PRL. \tag{1.28}$$

Finally, solutions can be obtained as:

$$N^2 = \frac{B \pm \sqrt{B^2 - 4AC}}{2A} \tag{1.29}$$

We will restrict the discussion to the case of perpendicular injection, i.e. for $\theta = 0$. Therefore the solutions of equation (1.29) are $N^2 = RL/S$ and $N^2 = P$. It can be proved that the two solutions refer to a different polarization of the electric field. The first solution corresponds to a wave whose electric field is perpendicular to the magnetic field (*extra-ordinary wave* or X-wave), while for the second solution, the electric field is parallel to the magnetic field (*ordinary wave* or O-wave). The different polarisations have important consequences for wave propagation and absorption. Let us introduce the concepts of *cut-off* and *resonance*. The first occurs when $N^2 \to 0$. The wave at the cut-off cannot propagate anymore and can also be reflected. The second occurs for $N^2 \to \infty$ and the wave can be absorbed by the plasma.

The O-mode has a cut-off frequency for $N^2 = P = 0$ ($\omega^2 = \omega_{pe}^2$). The X-mode has two cut-offs ω_L and ω_R, either for $L = 0$ or $R = 0$, which can be expressed as:

$$\begin{aligned} \omega_\mathrm{L} &= \frac{1}{2}\left[-\omega_{ce} + (\omega_{ce}^2 + 4\omega_{pe}^2)^{1/2}\right] \\ \omega_\mathrm{R} &= \frac{1}{2}\left[+\omega_{ce} + (\omega_{ce}^2 + 4\omega_{pe}^2)^{1/2}\right] \end{aligned} \tag{1.30}$$

The X-mode resonance ($S \to \infty$) occurs at the so-called *upper hybrid* frequency ω_uh, defined as:

$$\omega_\mathrm{uh}^2 = \omega_{pe}^2 + \omega_{ce}^2. \tag{1.31}$$

A more detailed description can be obtained by including warm-plasma corrections. In particular, the introduction of a *finite Larmor radius* allows to increase the number of resonances by adding the electron cyclotron resonances ($\omega = n\omega_{ce}$) for both modes.

The Clemmow-Mullay-Allis (CMA) diagram (figure 1.8) can be used to study the accessibility conditions for inhomogeneous plasmas, i.e. where

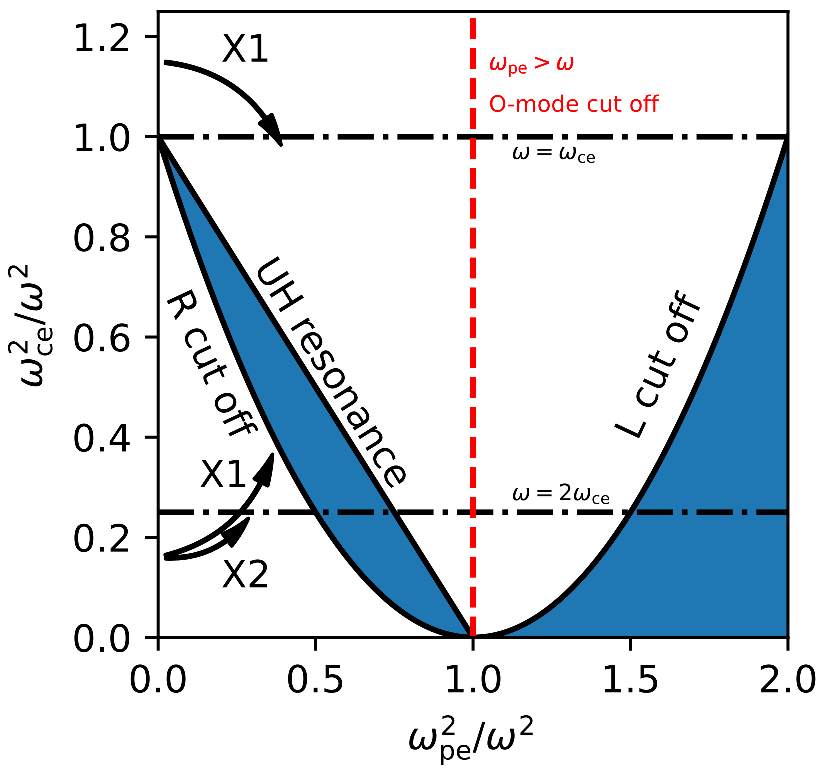

Figure 1.8.: Sketch of CMA diagram, adapted from [48]. The x- and y-axes are proportional to n_e and B^2, respectively. The horizontal dashed lines represent the first and second electron cyclotron resonances. An X1 wave injected from the low field side (LFS) encounters the R cut-off before reaching either the upper hybrid resonance or the first electron cyclotron resonance. Resonances are instead accessible for an X1 wave injected from the HFS or for an X2 wave injected from the LFS.

both the magnetic field and the electron density are not constant. This is the case for fusion relevant magnetic confinement devices, where the magnetic field depends on the distance from the major axis of the torus[6]. We define as low field side (LFS) the outboard part of the torus and as

[6] A $B \sim I/R$ dependence, with B and R being the magnetic toroidal field and distance from the major axis, is a good approximation for tokamaks. In stellarators this is not always true and the relation could vary for different toroidal positions.

high field side (HFS) the inboard part. In the CMA diagram the x-axis and the y-axis are proportional to n_e and to B^2, respectively, therefore the path of the wave moves upwards for LFS injection and downwards for HFS injection. Let us first consider the case of perpendicular injection. For the first harmonic of the O-mode, the wave propagates and reaches the resonance $\omega = \omega_{ce}$ for both HFS and LFS injection. This is not the case for X-mode polarised wave in which, for LFS injection, the wave encounters the low density cut-off before reaching the resonance position and is reflected. Conversely, the resonance can be reached for HFS injection. It is interesting to analyse the case for higher harmonic numbers n, $\{n \in \mathbb{N}\}$. For an O-mode polarised wave, the accessibility condition is given by $\omega_{\mathrm{p}} < n^2\omega_{\mathrm{ce}}^2$. In case of an X-mode polarised wave, the resonance layer becomes now accessible for both LFS and HFS injection. In case of oblique injection, the cut-off density limit is given by the condition $N_\perp = 0$, for fixed $N_\parallel$, making the accessibility condition for X-mode waves more restrictive, but the description is qualitatively similar to the case of perpendicular injection [48].

1.4.2. Wave absorption

ECR heating is based on the transmission of energy from waves to electrons, which occurs when the resonance condition is satisfied.

$$\omega = n\frac{\omega_{ce}}{\gamma} + k_\parallel v_\parallel \tag{1.32}$$

where γ represents the relativistic factor and $v_\parallel$ the velocity of electrons parallel to the magnetic field. The term $k_\parallel v_\parallel$ represents the Doppler shift and is zero for exactly perpendicular injection. ECRH mainly increases the perpendicular energy of resonant electrons, although parallel momentum increase can happen for strongly relativistic electrons. The energy transfer efficiency depends on several factors, such as the optical properties of the plasma, the wave polarisation and the harmonic frequency. Optical properties of the plasma are described by the optical thickness τ, which influences the power absorption in a single beam pass. High optical thickness values are desired, in order to increase the heating efficiency. The optical thickness strongly depends on the harmonic number n , T_e , n_e and the injection angle. For instance, for $n = 2$, the optical thickness of a X-mode polarised

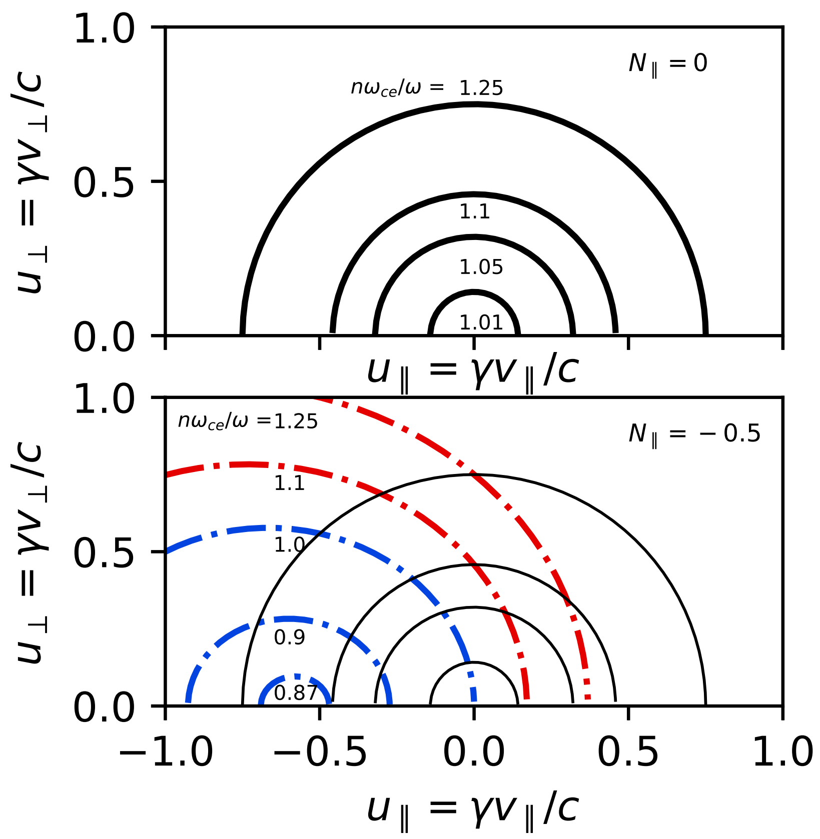

Figure 1.9.: Resonance ellipses for $N_\parallel = 0$ (top plot) and $N_\parallel = -0.5$ (bottom plot). Adapted from [48]. In top plot, the resonance ellipses coincide with the curves of constant energy. In the bottom plot, the resonance ellipses and the curves of constant energy do not coincide. This results in an asymmetric electron heating.

wave scales as $(T_e/mc^2)^{n-1}$, while for quasi-perpendicular injected O-mode, the scaling changes to $(T_e/mc^2)^n$. This dependence makes the absorption of the second harmonic X-mode waves better than the absorption for the second harmonic of O-mode. Nonetheless, O-mode (or the third harmonic of X-mode) can be absorbed at higher densities, which makes them interesting for reactor-size devices.

A wave with frequency ω can interact only with electrons whose velocity components $(v_{\parallel}, v_{\perp})$ satisfy equation (1.32). The absorption process is not isotropic and strongly depends on $k_{\parallel}$ and $\omega_{\rm ce}$ which vary along the path of the injected ray. For this reason, let us introduce the concept of the resonance curves. Considering the case where $|N_{\parallel}| < 1$, the resonance condition can be represented by an ellipse equation in the velocity space. Introducing $u = \gamma v/c$ and defining the extremes of the ellipses as $u_{\parallel\pm} = u_{\parallel 0} \pm \alpha_{\parallel}$, we obtain:

$$\frac{\left(u_{\parallel} - u_{\parallel 0}\right)^2}{\alpha_{\parallel}^2} + \frac{u_{\perp}^2}{\alpha_{\perp}^2} = 1 \tag{1.33}$$

where

$$\begin{aligned} u_{\parallel 0} &= N_{\parallel} \frac{n\omega_{ce}/\omega}{1 - N_{\parallel}^2} \\ \alpha_{\parallel} &= \frac{\sqrt{N_{\parallel}^2 + (n\omega_{ce}/\omega)^2 - 1}}{1 - N_{\parallel}^2} \\ \alpha_{\perp} &= \frac{\sqrt{N_{\parallel}^2 + (n\omega_{ce}/\omega)^2 - 1}}{\sqrt{1 - N_{\parallel}^2}}. \end{aligned} \tag{1.34}$$

Resonance ellipses for $N_{\parallel} = 0$,$(N_{\parallel} = -0.5)$ are plotted in figure 1.9. Let us start by analysing the perpendicular injection ($N_{\parallel} = 0$). In this case, equation 1.33 becomes the equation of the circle. In this condition, the energy absorption occurs only if $\omega \leq n\omega_e$. Four resonance ellipses for different $\gamma = n\omega_{\rm ce}/\omega$ values are plotted in figure 1.9. Let us consider the path of a ray propagating from the LFS. The ray propagates into the plasma, but no absorption occurs until the ray reaches the position where $\omega = n\omega_e/\gamma$ is satisfied. The wave energy is primarily transferred to low energy electrons and the energy of resonant electrons increases with the distance from the resonance layer. Conversely, if the injection occurs from the HFS, high energy electrons are primarily heated and the energy of resonant electrons decreases with the distance from the resonance layer. If the electromagnetic beam is obliquely injected ($|N_{\parallel}| > 0$) the contribution given by the Doppler shift term needs to be taken into account. Let us consider the case $N_{\parallel} = -0.5$, displayed in figure 1.9, where the blue and red curves represent the resonance ellipses and the black solid circles the regions in the parameter space of equal energy. The velocity space can be divided into three regions. On the low field side for $n\omega_e/\omega < 1 - N_\parallel^2$ a region exists, where no absorption occurs. In the limit $n\omega_e/\omega \to 1 - N_\parallel^2$, the ellipse collapses to the point $(u_\parallel, u_\perp) = (u_{\parallel 0}, 0)$ and absorption can occur in the high field side of it. The second region extends for $1 - N_\parallel < (n\omega_e/\omega)^2 < 1$ and the resonance ellipse (in blue) lies in the negative range of parallel velocities. It can be easily seen that in this region the condition $\omega > n\omega_e$ is satisfied, which represents the up-shifted absorption. Finally, the third region is given for $\omega < n\omega_e$ which represents the down-shifted absorption (in red). In this region, the resonant ellipse lies both in the positive and negative range of $u_\parallel$. In particular, the extreme $u_{\parallel +}$ is closer to the origin than the extreme $u_{\parallel -}$. For a Maxwellian distribution function, which is expected for a plasma at the thermal equilibrium, the population of high energy electrons strongly decreases as the energy increases, therefore the main contribution to the absorption comes from resonant electrons with $u_\parallel \sim u_{\parallel +}$. In this case the absorption starts with high energy electrons with a preferential velocity, thus creating an asymmetry in the distribution function. The main difference between perpendicular and oblique injection from the LFS relies on the energy of electrons involved in the power absorption. In the first case, energy is mainly transferred to bulk electrons, while in the latter case the absorption starts with high energy electrons moving in one direction. Such a difference is fundamental for the generation of a net toroidal current in the plasma.

1.4.3. Electron cyclotron current drive

Electron cyclotron current drive (ECCD) is a non-inductive current. It relies, like the Low Hybrid Current Drive (LHCD), on the distortion of the electron distribution function, although it is not generated by a direct increase in the electron parallel momentum. Two mechanisms are responsible for the generation of current: the Fisch-Boozer mechanism [49] and the Ohkawa mechanism [50]. A sketch is depicted in figure 1.10. The Fisch-Boozer mechanism relies on the generation of an "asymmetric plasma resistance". Let us consider a thermal plasma whose electrons display a Maxwellian distribution function. If oblique injection takes place, the energy transfer will begin with the electrons whose parallel velocities $v_\parallel$ match the resonance condition (equation (1.32)). These electrons are accelerated

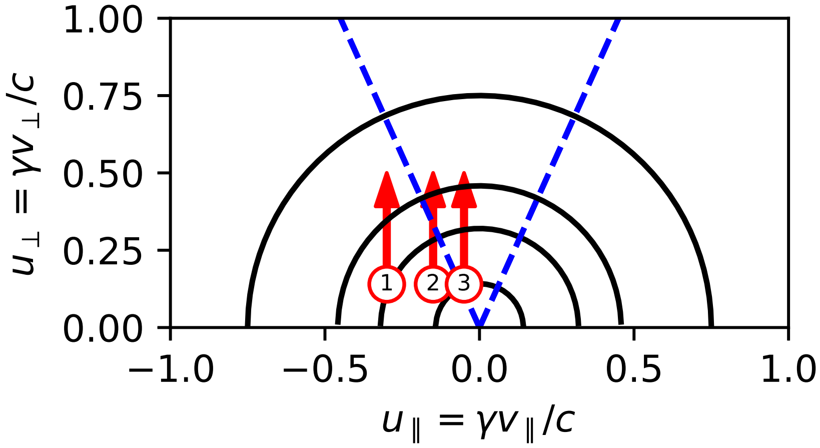

Figure 1.10.: Sketch of the different ECCD mechanisms. The region within the blue dashed lines represents the trapped particle region in the velocity space. (1) represents the Fisch-Boozer mechanism. (2) represents the Ohkawa mechanism. (3) represents the increase in parallel energy for a trapped electron, where no ECCD is generated.

to higher energies and therefore to a less collisional location in the velocity space, since the charged particle collisionality scales as $v^{-3} \sim T^{-3/2}$. The low collision frequency rate makes the isotropisation of high electrons slower than the isotropisation of the lower energy location they come from. This creates an asymmetric modification of the electron distribution function and hence a net toroidal current (case 1 in figure 1.10).

The Ohkawa mechanism consists in moving electrons with velocity $v_\parallel$ from the passing region to the trapped region. The momentum isotropisation due to the bouncing motion of trapped electrons is faster than the momentum isotropisation due to Coulomb collisions, thus creating a depletion of electrons at energies inferior than the resonance energy. This results in a current with an opposite sign with respect to the Fisch-Boozer mechanism (case 2 in figure 1.10). A discussion regarding the two mechanism can be found in [51].

Electron current drive efficiency depends on the plasma collisionality. High T_e increases the ECCD efficiency, while high n_e decreases it. Also the effect of trapped particles has to be taken into account, since they can strongly affect the maximum achievable current. In fact, due to their fast bounce motion, trapped particles do not possess any privileged parallel velocity. Any increase in the parallel momentum of trapped particles will be immediately isotropised by their bouncing motion (case 3 in figure 1.10) and no net current will be produced. Finally, electrons that lie in the velocity space away from the trapped particle cone can decrease the efficiency of the current drive. ECCD is an excellent tool for the generation of non-inductive current drive. The toroidal current produced in this way is also well localised and has successfully been used in tokamaks for plasma instability control, such as sawtooth amplitude control or neoclassical tearing mode suppression [52]. The stabilisation is achieved by shaping the current density profile inside the resonant surface or by depositing power and current inside the formed magnetic islands. In stellarators ECCD is used to compensate the intrinsic bootstrap current or to study the influence of shear on confinement and stability [53]. An overview of ECCD experiments conducted in several machine is reported in [48], while an introduction to the main findings of ECCD experiments at W7-X is presented in the next chapter, along with the description of the main properties of W7-X.

1.5. Wendelstein 7-X

Wendelstein 7-X (W7-X) is presently the most advanced stellarator and started operation in 2015, with the aim to demonstrate that stellarators offer an attractive configuration for fusion reactors [54]. W7-X is a five-period stellarator whose magnetic field coil system is composed of 50 superconductive non-planar coils and 20 superconductive planar coils [55, 56]. In addition 10 normal-conducting control coils are installed inside the plasma vacuum vessel to control the divertor strikeline position. Finally, 5 normal-conducting coils, named trim coils, are installed outside the cryostat vessel in order to correct magnetic field errors [57]. The coil system has been optimised in order to provide good confinement for fast particles, good magnetohydrodynamic stability, reduced neoclassical transport, small bootstrap current and suppressed Shafranov shift [58, 59, 60, 61, 62, 63]. Plasma heating is provided by ECRH (up to 7.5 MW of heating power) and NBI (up to 2.7 MW for up to 10 s). ICRH is foreseen to be installed in the future. The ECRH system [64, 65] is composed of 10 gyrotrons at 140 GHz able to

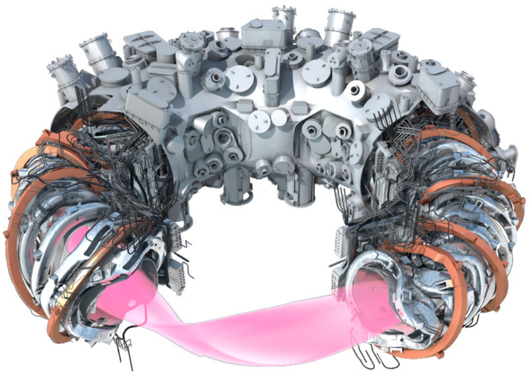

Figure 1.11.: Representation of W7-X. It is possible to notice the 20 superconducting planar coils (orange) and the 50 non-planar coils (silver) (© IPP).

operate in O-mode and X-mode at the second harmonic (for $B = 2.5\,\mathrm{T}$) or third harmonic (for $B \sim 1.7\,\mathrm{T}$). Injection occurs in the proximity of the bean-shaped plane (figure 1.2) where the magnetic field gradient is stronger and therefore the beam absorption is well localised. The typical plasma parameters achieved during the first experimental phases are reported in table 1.1.

W7-X is a low shear stellarator relying on the island divertor concept [66, 54, 67]. The majority of the operational magnetic configurations have been designed to avoid rational values in the rotational transform profile. Rational values are instead reached at the plasma edge, where large magnetic islands are formed and intersect the divertor. The intersection produces a scrape-off layer, that represents the boundary between the confinement region and the target elements, where the power flowing out from the confinement region is deposited. For this reason the control of the edge rotational transform is crucial for safe operations since a misalignment of the strikelines on the divertor plates can seriously damage components that have not been designed to sustain strong heatfluxes. For this purpose, the main concern is represented by the evolution of the toroidal current, such as the bootstrap current. The current does not develop suddenly, but according to

$$I_{\mathrm{tor}}(t) = I_{\mathrm{tor}}(t \to \infty)(1 - e^{-t/\tau}) \tag{1.35}$$

where $\tau = L/R$ and L and R are the plasma inductance and resistance, respectively. For W7-X, $\tau \sim 10 - 30\,\mathrm{s}$. As the toroidal current evolves, the rotational transform at the edge changes (equation 1.2) in time [68]. To provide additional protection, the so-called *scraper elements* were introduced [69]. They are positioned in front of divertor and are designed to receive the heat-loads in case of large strikeline misalignment. Alternatively, the shift of the strikelines can be compensated by the use of external control coils, which changes the rotational transform at the edge or by driving a non-inductive current, such as ECCD [53]. For this scope ECCD has already been used successfully in two different ways. The first one relies on driving current with a reverse sign of the bootstrap current, in order to achieve $I_{\mathrm{tor}} \sim 0$. The second one relies on a fast ramp-up of the toroidal current, in which ECCD is used to accelerate the development of the toroidal current to the value of stationary bootstrap current. As the bootstrap current builds up the ECCD is ramped down. This way, the necessity for constantly driving a current is avoided. In such a way the exposure of fragile components to strong heat-flux can be significantly reduced and controlled.

However, temperature crashes, similar to sawtooth crashes, have been observed during ECCD experiments at W7-X [55, 70]. Figure 1.12 shows the central T_e in experiments with co-ECCD (blue) and counter-ECCD (red) during the first operation phase, where fast T_e can easily be distinguished in both cases. This phenomenon was unexpected at W7-X and this thesis aims to provide a first study and characterisation of this phenomenon.

Tor. Magnetic field (axis)	$B = 2.52\,\mathrm{T}$
Major radius	$R_0 = 5.5\,\mathrm{m}$
Minor radius	$a = 0.5\,\mathrm{m}$
Electron Temperature (axis)	$T_e = 5\,\mathrm{keV}$
Ion Temperature (axis)	$T_i = 1\,\mathrm{keV}$
Line int. density	$< n_e >= 2 - 5 \cdot 10^{19}\,\mathrm{m}^{-3}$

Table 1.1.: Typical parameters for W7-X experiments during the first operational phases

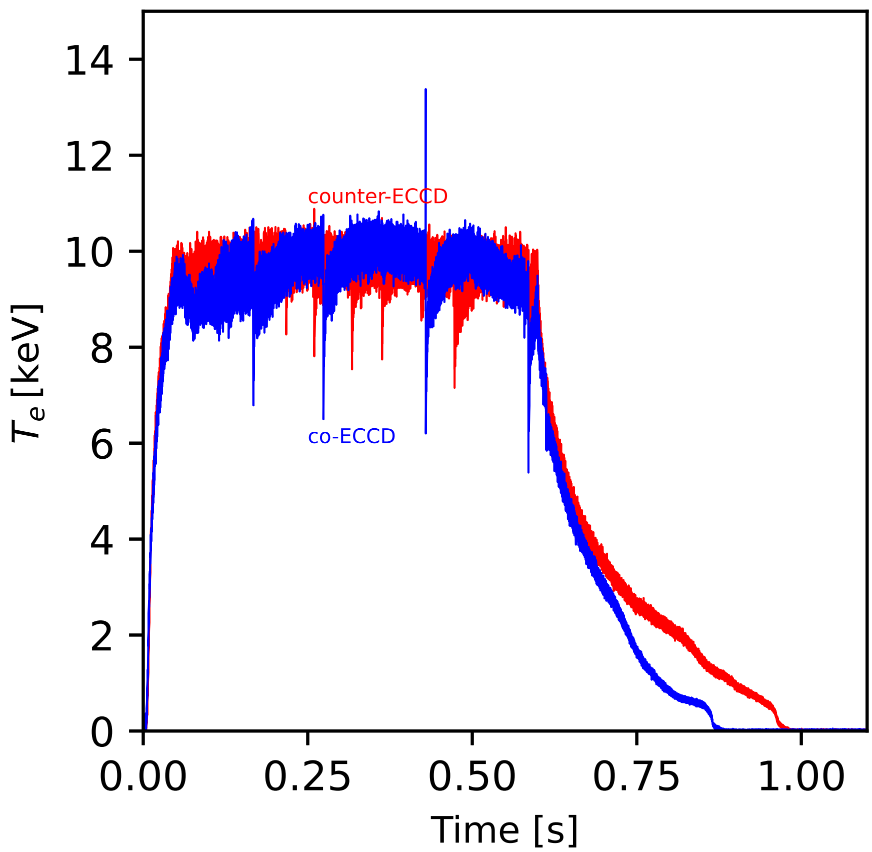

Figure 1.12.: Temperature crashes detected during the first experimental campaign of W7-X. The timetraces show the central T_e measured by the electron cyclotron emission during co-ECCD (blue) and counter-ECCD (red) experiments.

1.6. Aim of the thesis

In this work we started the characterisation and the study of the sawtooth crashes at W7-X. The understanding of the sawteeth at W7-X is therefore crucial for future operations, in order to avoid plasma performance issues. At the same time a study is necessary to investigate the possibility to control the sawteeth crashes and use them for different purposes, such as impurity control or improvement of the plasma fuelling.

The work is organised as follows: the main diagnostic tools which were used for this work are described in the second chapter. In the third chapter we present current diffusion calculations, in order to show how the current itself can locally change the rotational transform and we compare the typical timescales for the stability onset with the calculation results. The analysis of the sawtooth crashes is presented in the fourth chapter. Here we start characterising long plasma discharges, in order to highlight the main features of the sawtooth crashes at W7-X. In the fifth chapter we will present some events which were observed at relatively high toroidal current. During these events, a sudden raise of electron density was detected and was in certain cases followed by a termination of the experiment. Finally, in the sixth chapter, a summary is presented and conclusions and further developments for the next experimental phase are discussed.

Chapter 2.

Diagnostics and data analysis tools

2.1. Plasma diagnostics

W7-X is equipped with several plasma diagnostics [71]. In this section, a description of the main diagnostic tools used for the data analysis in this thesis is presented (figure 2.1). A more detailed description regarding plasma diagnostics in general can be found in [72], while reference papers for every used diagnostic are provided in the corresponding sections.

2.1.1. Electron cyclotron emission

Electron cyclotron emission (ECE) measures the T_e [73] profile along a 1-D line of sight. Electrons rotate around magnetic field lines, with a cyclotron frequency $\omega_\mathrm{c} = eB/(\gamma m)$, where e is the charge of the electron, B is the magnetic field, γ is the relativistic factor and m is the mass of the electron. For a basic explanation a toroidally symmetric arrangement may be considered. In a 3D confinement device as it is a stellarator there may be differences, e.g. in the triangular plane of W7-X the magnetic field is nearly flat. In a axisymmetric configuration, the magnetic field scales as $B(r) \approx B_0/(R_0 + r)$, where B_0 is the magnetic field at the magnetic axis, R_0 is the major radius and r is the minor radius. Therefore, in case of an inhomogeneous magnetic field, it is possible to relate a certain frequency to a certain radial position. The spectrum of the radiation from gyrating

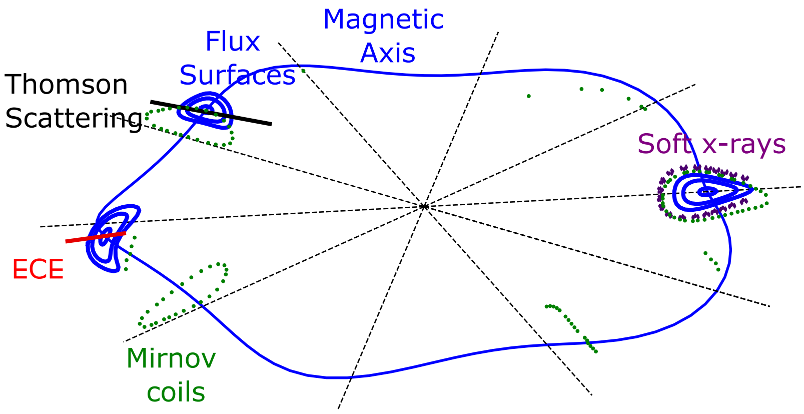

Figure 2.1.: Positions of some of the main diagnostics used in this work. The blue line represents the magnetic axis, the blue curves represent the flux surfaces in correspondence of the Electron Cyclotron Emission (line of sight in red), Thomson scattering (line of sight in black) and the soft x-ray cameras (in purple). The green points represent the Mirnov coils.

electrons is composed of a series of discrete harmonics:

$$\omega_l = \frac{l\,\omega_{ce}}{1 - \beta_{\parallel}\,cos\theta} \tag{2.1}$$

where $\beta_{\parallel} = v_{\parallel}/c$ and θ is the angle between the direction of the observation and the magnetic field line. For the typical plasma parameters of W7-X, the plasma is optically thick in the plasma core (for $T_e >> 200\,\mathrm{eV}$) for the second harmonic ($l = 2$), i.e. the optical thickness $\tau_l >> 1$. This means the plasma emits as a black body. Therefore, according to the Rayleight-Jeans

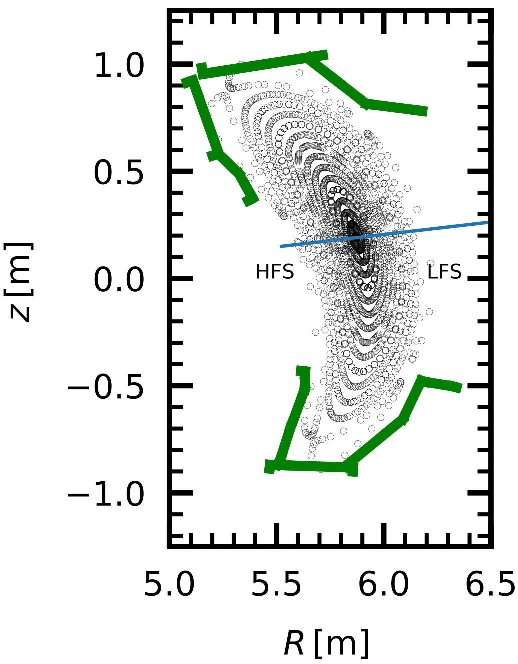

Figure 2.2.: Representation of the ECE line-of-sight at W7-X.

approximation, the intensity I of the radiation emitted by electrons with gyrating frequency ω_0 is:

$$I(\omega_0) \approx \frac{\omega_0^2 T_e}{8\pi c^2} \tag{2.2}$$

The observed intensity is a function of T_e, which is a local parameter of the plasma at the resonant position and not a line integrated parameter. The ECE radiometer at W7-X [74] is composed of 32 channels, each one detecting a different frequency of the second harmonic of the X-mode. All channels are absolutely calibrated with a sampling rate between 200 kHz and 1 MHz, which allows detecting fast changes of the temperature profiles. The ECE channels are mapped to the effective radius $r_{\text{eff}} = \sqrt{\langle A \rangle / \pi}$ using the following definition: channels detecting at the outboard region of the plasma, namely the low field side (LFS), are labelled with negative radial

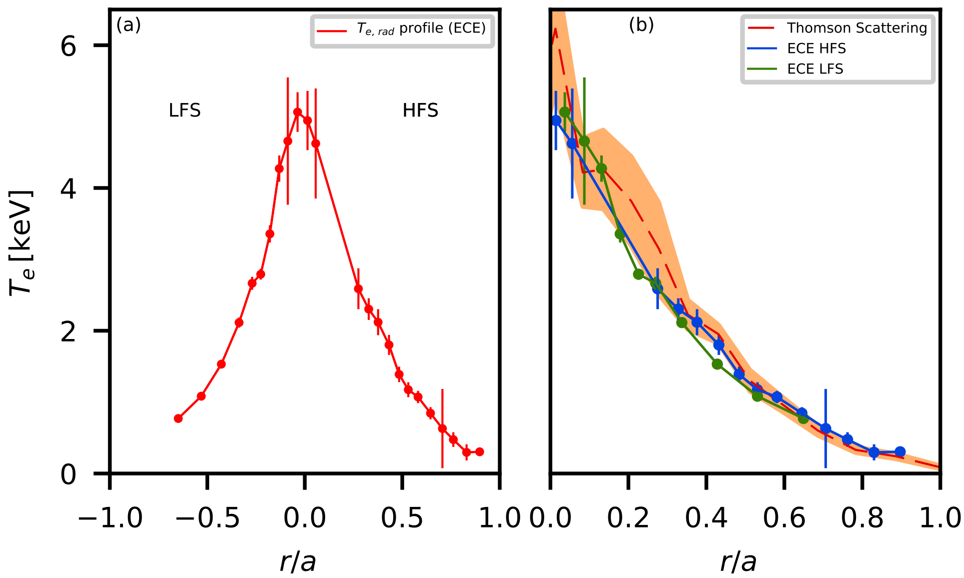

Figure 2.3.: Left: Typical T_e profile, mapped to the radial position. Right: ECE profiles (blue for HFS and green for LFS) against a Thomson scattering profile (red).

position, while inboard (high field side, HFS) channels with a positive value. The mapping is performed taking into account diamagnetic effects, the Shafranov shift and the finite emission layer.

The T_e spectrum is estimated with a Bayesian model [75]. In figure 2.3a a typical T_e profile is plotted, while in figure 2.3b ECE data are compared to the Thomson scattering data. Both sides of the ECE profile agree with the Thomson scattering profile, especially at lower temperatures. At higher temperatures the HFS and LFS channels present some discrepancies which are however within the errorbars. In [76], the contribution of the second harmonic of the O-mode, coming from the plasma core, to the detected signal was analysed. For the electron density values which were generally detected in the experiments we analysed in this work ($n_e \sim 2-4\cdot 10^{19}\,\mathrm{m}^{-3}$) the O-mode contribution influences mainly the LFS channels. This often resulted in weakly asymmetric temperature profiles. The dominant uncertainty of the measurement is given by calibration errors, which are plotted in figure 2.3(a) along with the temperature profile itself. Calibration errors are much higher than the noise contribution, which is relatively small (less than 6 %). In this work we analysed the sawtooth crashes by using the relative changes of T_e (usually within 30 and 60 %) and in such a way the measurement was not affected by the calibration errors. A more detailed explanation is provided in section 2.3.2. Additionally, information regarding the nature of the precursor MHD activity can be assessed, as explained in section 2.3.1.

2.1.2. Soft x-ray tomography system

The x-ray multicamera tomographic system (XMCTS) detects the soft x-ray radiation in the range of 1 keV – 12 keV. The energy spectrum is composed of continuum contribution and line radiation [77]. The first term is given by free-free emission (bremsstrahlung) and free-bound emission (recombination), while the line radiation is given by bound-bound emission, as a consequence of the de-excitation of atomic excited states. The bremsstrahlung emission is line integrated and proportional to $T_e^{1/2} n_e^2 Z_{\text{eff}}$, therefore the interpretation of signal changes is more difficult than for the ECE signal. However, it is often assumed that the position the dominant contribution comes from is the tangential point between the line of sight (LOS) and the flux surface and therefore it is possible to assign a radial position to each LOS. Additionally, soft x-rays also provide information about the impurity transport and dynamics. The Soft x-ray tomography system [78] is composed of an array of 20 pinhole cameras, each one with 18 lines of sight and a sampling rate of 2 MHz. The camera array is situated at the so-called triangular plane, as depicted in figure 2.4. The ten upper cameras and the ten lower cameras are symmetrically distributed around the horizontal mid-plane of the plasma. The diagnostic allows to reconstruct the 2-D emissivity plasma profile in the poloidal plane. The tomographic inversion is obtained using the minimum Fisher regularised inversion, as presented in [79].

The XMCTS was used as a complementary diagnostic to ECE for the study of the crashes, although it was not always possible to detect the weaker sawtooth crashes. Singular value decomposition (SVD, see appendix A.1) was applied to the tomographic reconstruction to identify the dominant poloidal number m of the crash precursors.

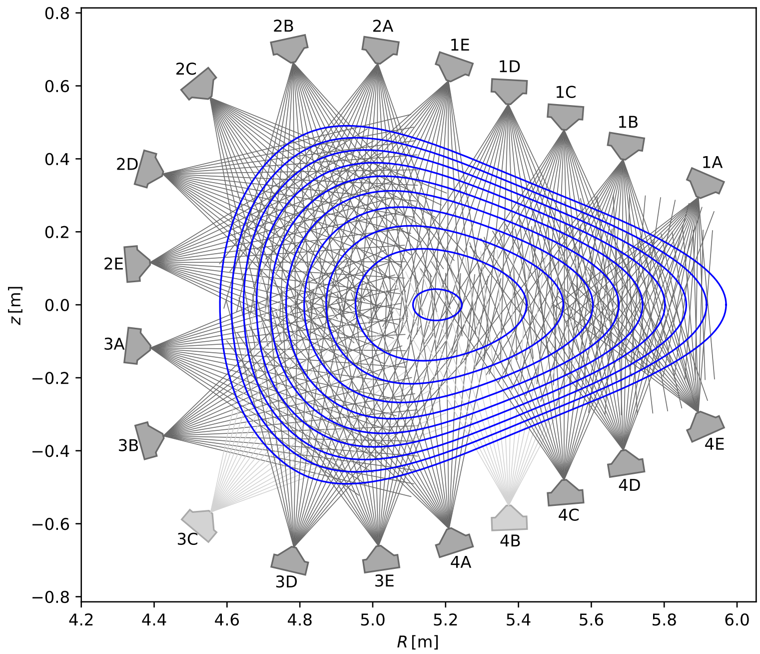

Figure 2.4.: Overview of the x-ray camera line of sights.

2.1.3. Dispersion interferometer

The line integrated electron density is measured at W7-X by a single channel dispersion interferometer [80]. Interferometry is based on the refraction of an electromagnetic wave entering the plasma. Before entering the plasma, a laser beam passes through a frequency doubling crystal, thus resulting in a laser beam containing two "colours" ω and 2ω. If the plasma frequency ω_p is smaller than the frequency of the electromagnetic wave ω_0, the refrective index N of the plasma depends on the electron density:

$$N \approx 1 - \frac{1}{2}\left(\frac{\omega_p^2}{l\omega^2}\right) = 1 - \frac{e^2}{2\epsilon_0 m_e \omega_l} n_e \tag{2.3}$$

where $l = 1, 2$ represents the harmonics. Due to different beam frequencies, the two harmonics propagate with a different refractive index and information regarding the electron density can be obtained by the phase delay between the first and the second harmonic. The phase shift can be written as:

$$\phi_p = \frac{3e^2\lambda}{4\pi c_0^2 \epsilon_0 m_e} \int n_e(l)\,\mathrm{d}l \tag{2.4}$$

from which the line integrated density can be obtained. The measurement is not spatially resolved, but it is used to have a global overview on the n_e trend and detect fast changes, with a sample rate of 100 kHz.

2.1.4. Thomson scattering

The Thomson scattering measures the electron temperature T_e and the electron density n_e. It is based on the elastic scattering ($\hbar\omega \ll m_e c^2$) of electromagnetic radiation by a free electron. One interpretation is that a laser beam, which is injected into the plasma, accelerates the electrons, which act as dipoles and radiate. Ions can be neglected due to their higher inertia. The T_e is calculated from the degree of Doppler broadening of the scattered radiation. Additionally, the radiation intensity is proportional to the electron density n_e, thus providing a measurement of T_e and n_e together. At W7-X [81, 82] three pulsed Nd:YAG lasers with a wavelength of 1064.14 nm are used. Each laser has a repetition rate of 10 Hz and therefore in standard operation the sampling frequency is up to 30 Hz. Since the temporal resolution is generally too low to study the dynamics of T_e and n_e during the observed temperature crashes, the data have been used either for magnetic equilibria reconstruction or as a crosscheck for the ECE data (figure 2.3).

2.1.5. Extreme ultraviolet spectroscopy

Passive spectroscopy is used to measure the line radiation of impurities. Impurities are either released due to plasma-wall interaction (Be, B, C, O, Si,metals) or added on purpose (He, N, Ne, Ar) for diagnostic purposes. For the typical W7-X plasma parameters, the strongest spectral lines of the impurities like carbon, oxygen and nitrogen are in the range of the vacuum ultraviolet/extreme ultraviolet wavelength range ($1 - 200$ nm). The observation of the emission from different ionisation stages can provide information regarding both the impurity concentration and transport properties. At W7-X the High Efficiency Extreme Ultraviolet Overview Spectrometer

(HEXOS) is employed. It is composed of four VUX/XUV overview spectrometers, detecting from 2.5 to 160 nm, with an acquisition rate of 1 kHz [83]. In this work it was used to investigate the composition of the strong impurity influx, detected after strong sawtooth crashes.

2.1.6. Mirnov coils

Mirnov coils are used to detect $\dot{B}_{\mathrm{pol}}$ at the plasma edge. At W7-X [84] several poloidal arrays are installed at different toroidal positions, for a total of 125 Mirnov coils, with a sampling rate of 2 MHz. This yields information about the poloidal and toroidal mode numbers as well as the frequency, with great resolution. The system is able to detect mode numbers up to $m \sim 20$, $n \sim 10$. The array is located outside the plasma, therefore no information about the radial structure or the localisation of the mode can be inferred. The intensity of a magnetic perturbation decays as $B \approx r^{(m+1)}$, with m the poloidal mode number, making the amplitude of perturbations localised in the centre smaller than the amplitude of perturbations near the plasma edge.

The Mirnov coils were used to calculate the poloidal numbers of MHD modes. Due to an acquisition system issue, a delay between the ECE and Mirnov coil signal was found, as well as a delay between coils located at different toroidal position. For this reason, the toroidal mode number analysis was not possible.

2.1.7. Continuous Rogowski coils

The net toroidal current I_{tor} flowing in the plasma can be measured by means of a continuous Rogowski coil, which consists of a coil that poloidally encircles the plasma cross section. The toroidal current I_{tor} produces a magnetic flux, whose variation in time gives rise to an electromotive force V:

$$V = \dot{\Phi} = nA\mu_0 \dot{I}_{\mathrm{tor}}. \tag{2.5}$$

where n represents the number of turns in the coil of area A and dot denotes the time derivative. Finally, by integration of the signal, it is possible to measure changes of the total toroidal current. At Wendelstein 7-X, the net toroidal current is measured by a continuous Rogoswki coil, with a sampling rate of 50 kHz. The continuous Rogowski coil measures the net I_{tor} flowing in the plasma and does not allow to reconstruct the current density profile $j(r)$. However, it will be shown (section 4.4) that I_{tor} correlates with the size of a sawtooth crash and therefore it is used as a parameter to investigate the crash size.

2.1.8. Diamagnetic loops

The diamagnetic loops provide a measurement of the diamagnetic energy (W_{dia}) stored in the plasma. The measurement is based on the detection of toroidal flux changes, which are generated by currents flowing perpendicularly to the magnetic field. As summarised in [85], the toroidal flux is given by:

$$\Phi = \frac{\mu_0^2 I_{\mathrm{tor}}^2}{8\pi B_0} + \frac{\pi\mu_0 \iota\!\!\text{-}}{R}\int_0^a j_{\mathrm{tor}}(r) r^3 \,\mathrm{d}r - \frac{\mu_0 W_{\mathrm{dia}}}{3\pi R B_0}. \tag{2.6}$$

where I_{tor} is the toroidal current measured by the Rogowski coils, B_0 is the axis magnetic field at the position in which the loops are located, $\iota\!\!\text{-}$ is the rotational transform, $j_{\mathrm{tor}}(r)$ is the current density and a and R are respectively the minor and major radii. For W7-X plasma parameters, the first two terms in the RHS are negligible and therefore, $W_{\mathrm{dia}} = -3\pi R B_0 \Phi/\mu_0$.

A good agreement between the diamagnetic energy and the kinetic energy, obtained by Thomson scattering data, was found in [85].

Being the Thomson scattering sample rate too low for resolving a sawtooth crash, W_{dia} was used to have a fast and reliable measurement of the stored plasma energy.

2.2. TRAVIS-code

No direct measurement of the profile of the toroidal current is presently possible at W7-X. Therefore the toroidal current has to be calculated either using codes like NTSS (for the bootstrap current) [86] or by calculating the power deposition and current drive efficiency with the TRAVIS-Code [87]. TRAVIS is a ray-tracing code developed at IPP, which calculates the ECRH beam propagation into the magnetised plasma and the power deposition from the wave itself to the electrons. If the WKB approximation can be used (i.e. $|\nabla k|/k^2 << 1$, where k is the wavenumber of the propagating wave) the ray-trajectory can be described using the "cold" dispersion relation (section 1.4.1). This assumption is not valid in the proximity of the cyclotron resonance due to relativistic thermal effects, where a fully relativistic treatment is necessary. Generally, a Maxwellian distribution function is assumed for electrons and the power transfer from the electromagnetic wave to the plasma is calculated under the assumption that the interaction remains linear. A proper treatment regarding TRAVIS can be found in [87] and in the references therein. Here we just present the main concept regarding the calculation of the power deposition and current drive. The beam is divided into different rays and the power absorption along the ray path can be expressed as:

$$\frac{\mathrm{d}P_{\mathrm{abs}}}{\mathrm{d}s} = P_0 \alpha_\omega \mathrm{e}^{-\tau_\omega} \tag{2.7}$$

where P_0 is the power of each ray, α_ω is the cyclotron absorption coefficient and τ_ω the optical thickness.

The current drive flowing through an area δA between two neighbouring flux surfaces ψ and $\psi + \delta\psi$ can be defined as:

$$\delta I_{\mathrm{tor}} = \int_{\delta A} \left(\frac{j_\parallel}{B}\right) \mathbf{B} \cdot \mathrm{d}\mathbf{S} = \frac{< j_\parallel B >}{< B^2 >} \delta\Psi_{\mathrm{tor}} \tag{2.8}$$

where Ψ_{tor} is the toroidal magnetic flux and $\langle ... \rangle$ indicates a flux surface averaged quantity. Ray-tracing codes calculate the current drive efficiency, defined as $\eta = j_\parallel / P_{\mathrm{abs}}$. The current generated on the arc-length for a given ray is:

$$\frac{\mathrm{d}I_{\mathrm{tor}}}{\mathrm{d}s} = (< B > V')^{-1} \eta \frac{\mathrm{d}P_{\mathrm{abs}}}{\mathrm{d}s} \tag{2.9}$$

and finally the elementary toroidal current for the given ray is given as:

$$\frac{\delta I_{\mathrm{tor}}}{\delta \Psi_{\mathrm{tor}}} = V' |\frac{\delta V'}{\delta s}|^{-1} \frac{\mathrm{d}I_{\mathrm{tor}}}{\mathrm{d}s} \tag{2.10}$$

The total current is then obtained by the summation of all ray contributions and integration of equation 2.10. Alternatively, the term $< j_\parallel >$ can be obtained by equations 2.8 and 2.10. Figure 2.5 shows a 2-D poloidal cut, where a beam (grey) enters the plasma and propagates until the resonance

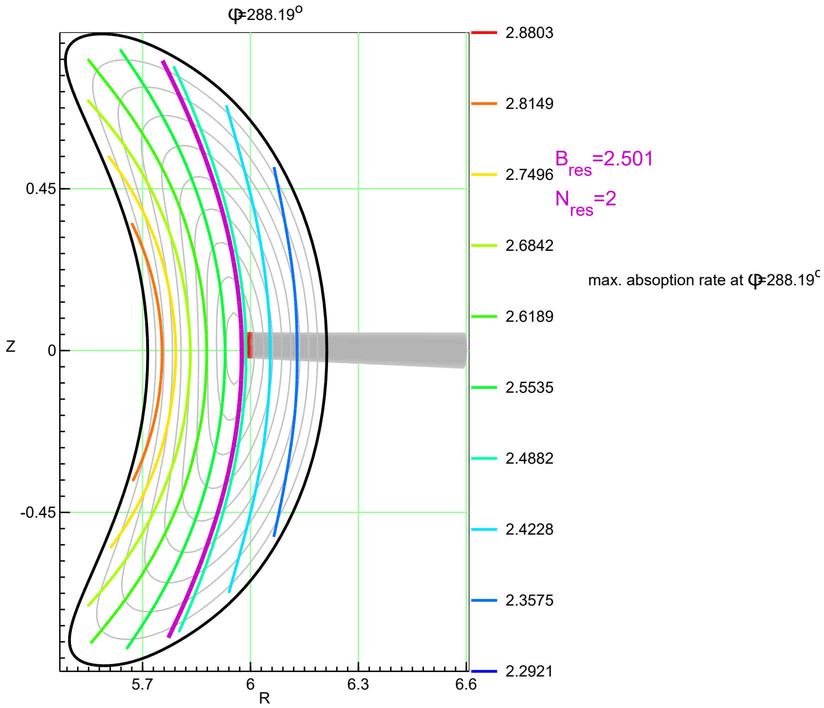

Figure 2.5.: Ray propagation and absorption calculated by the ray-tracing code TRAVIS. The injected beam is depicted in grey and the region where absorption takes place in red. The coloured lines indicate the magnetic field strength, whose values are reported on the right side of the picture. The purple curve represents the cold resonance magnetic field ($B = 2.5$T).

condition is met. Due to partially oblique injection (not visible from the 2-D cut) the position where the power absorption (red) occurs at a magnetic field slightly lower than $B = 2.5$T, represented by the purple curve.

2.3. MHD activity analysis tools

2.3.1. Instability characterisation with ECE

Temperature oscillations are related to deformations of the flux surfaces [88]. In case of sinusoidal crash precursors, it was possible to discriminate between even or odd poloidal numbers m. If the oscillations between the inboard and outboard region of the plasma are in phase, the instability has an even poloidal number, otherwise the poloidal number is odd.

Additionally, if a magnetic island, with no strong heating into it, is present and the mode rotates, the ECE channels will detect a constant temperature as long as it is measuring inside the island and the unperturbed T_e when measuring close to the X-point. The measured signal will show a T_e oscillation due to the transits of the X- and O-points. Additionally, the perturbations are out of phase at the two sides of the island [16].

The opposite oscillation phase of the neighbouring channels can also be seen in the change of sign of the displacement function $\xi(r) = (T_e(t) - \langle T_e \rangle)/\nabla \langle T_e \rangle$, where $T_e(t) - \langle T_e \rangle$ represents the temperature perturbation and $\langle T_e \rangle$ the unperturbed temperature profile [88]. ξ represents in fact the displacement of the flux surfaces from the equilibrium. If a magnetic island opens up, it pushes the inner flux surfaces inwards and the outer flux surfaces outwards and therefore ξ has different signs on the two island sides (figure 1.5).

The temperature profiles were smoothed and the signal of every channel rescaled to the smoothed value. In this way it was possible to analyse also the channels with a wrong calibration. The oscillations were analysed by means of Welch's method, based on the Fast Fourier Transform. A reference channel was chosen and the dominant values of the power spectrum $P_{xx}(f)$ extracted for every channel. The cross power spectral density ($P_{xy}(f)$) was calculated between the reference signal and the signal of each ECE channel and the phase ϕ between them is represented by $\phi = \arctan(\Im(P_{xy})/\Re(P_{xy}))$.

2.3.2. Crash detection

In a typical ECCD experiment, hundreds of sawtooth crashes can be present and therefore an automatised algorithm, which detects the crashes and calculates the main crash parameters (described below) was developed. At first a ridge detection algorithm has been applied to ECE data to automatically detect fast changes of the electron temperature T_e. The algorithm is based on continuous wavelet transform (CWT) $Wf(a,t)$ [89], which corresponds to the convolution of the signal $f(t)$ and a waveform $\psi(t)$, called mother

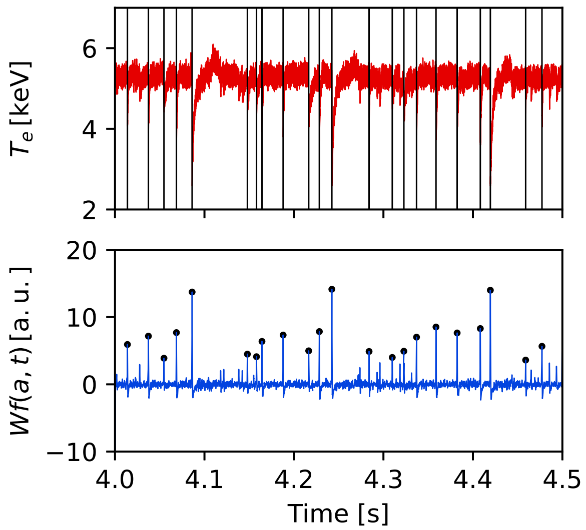

Figure 2.6.: Top: ECE central channel. The presence of temperature is visible. Bottom: wavelet transform of the ECE signal. Every peak represents a crash.

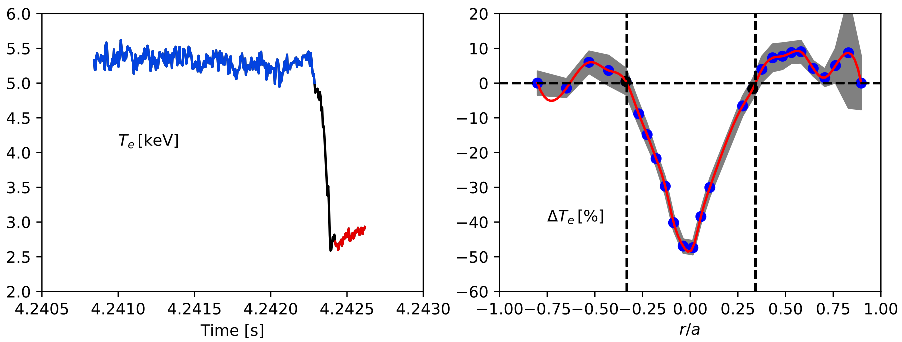

Figure 2.7.: Right: relative temperature change (percentage) during a sawtooth crash. The pre-crash profile is obtained by the average of the data in blue in the left plot, while the post-crash profile by averaging the red data. The grey area represents the uncertainty of the relative temperature change, while the dashed vertical lines indicate the position of the inversion radii.

wavelet, using different scales a and positions τ. It can be written as:

$$Wf(a,t) = \frac{1}{\sqrt{a}} \int_{-\infty}^{\infty} f(t)\psi^* \left(\frac{t-\tau}{a}\right) \mathrm{d}t \tag{2.11}$$

where * indicates the complex conjugate of the wavelet function. A good choice for a ridge detection algorithm is based on the first derivative of a Gaussian [1], which provides precise localization, reliable edge detection and it is well suited for noise filtering. This approach is equivalent to the Gaussian filtering generally used in a Canny edge detector algorithm [90]. The wavelet transform coefficients are represented by peaks in correspondence of fast and sharp discontinuities of the signal, whose time position can easily be detected (figure 2.6). It should be noted that, according to the chosen scale, the peak maxima can shift. Therefore, an interval around the peak maxima, of 300 µs, is defined, in which the temporal coordinate of the signal maximum and minimum is found. These two values are related to the temperature before and after the crash. For each ECE channel, the pre- and post- crash T_e is calculated. The left plot in figure 2.7 shows the temporal intervals over which the T_e is averaged. The blue region extends from $t_{\text{crash}} - 1500\,\mu\text{s}$ to $t_{\text{crash}} - 500\,\mu\text{s}$. The red region from $t_{\text{crash}} + 30\,\mu\text{s}$ to $t_{\text{crash}} + 230\,\mu\text{s}$, where t_{crash} is the time corresponding to the maximum of the wavelet transform (figure 2.6, bottom plot). Using the T_e profiles before and after the crash, we calculate the relative temperature change, defined as $\Delta T_e = (T_e^{after} - T_e^{before})/T_e^{before}$ (figure 2.7, plot on the right). Data are interpolated with a spline of 100 points. The $\Delta T_e^{\max}$ is defined as the strongest temperature change, while the position of the two r_{inv} is calculated as the position where $\Delta T_e = 0$. If more solutions are found, the points closer to the $\Delta T_e^{\max}$ are taken. The biggest source of uncertainty comes from the ECE mapping. Asymmetries in the T_e profiles (due to a possible ECRH beam shine-trough, O-mode contribution, suprathermal electron emission or partially wrong mapping from channel frequency to radius) were detected during experiments and affected mainly the LFS. This asymmetry has a direct impact also on the determination of the inversion radii, which are not always symmetric. The HFS is generally less affected by beam shine-through or O-mode contribution and therefore is generally taken as a reference.

The error of the relative temperature change is calculated from the standard deviation of T_e before and after the crash. The uncertainty of r_{inv} is calculated as $\sigma_r \approx \sigma_{\Delta T_e}/m$, where $\sigma_{\Delta T_e}$ and m are the ΔT_e uncertainty and the derivative of the spline at r_{inv}, respectively. The uncertainty regarding

[1] $\psi\left(\frac{t-\tau}{a}\right) = -\left(\frac{t-\tau}{a}\right) e^{-\frac{1}{2}\left(\frac{t-\tau}{a}\right)^2}$

the time detection is neglected. In fact, the error in the time domain is related to the width of the peaks of the wavelet transform, which is negligible with respect to the distance between two crashes as it can be seen in figure 2.6.

The algorithm developed for this work proved to be well suited for the detection of sawteeth with weak precursors. However for experiments characterised by a strong precursor activity, it was not able to distinguish between the precursors and the crashes.

Chapter 3.

1-D current diffusion model [1]

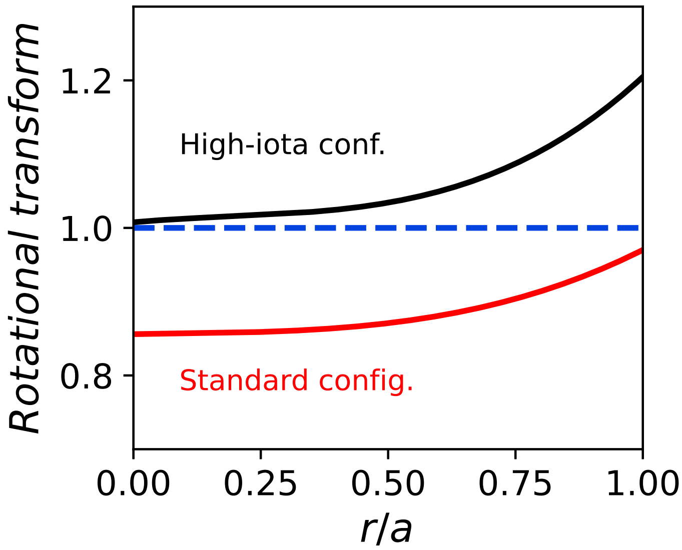

Figure 3.1.: Rotational transform profiles for two different magnetic configurations.

Magnetic confinement at W7-X is generated by the external coils. Most configurations are designed in such a way the rotational transform $\iota\!\!\!-$ does not cross any low order rational values in the confinement region. However, low order rational values are crossed at the edge, e.g. $\iota\!\!\!- = 4/5, 5/5, 6/5$, etc., where an island chain opens up and intersects the divertor plates. An

[1]Part of this chapter was published in [70]

example of typical ι profiles is depicted in figure 3.1. However, if a net toroidal current is present, ι can be written as a combination of two terms [4]:

$$\iota = \iota_{cf} + \iota_{\mathrm{curr}} \tag{3.1}$$

where ι_{cf} is the rotational transform created by the external magnetic coils and ι_{curr} is the contribution to the rotational transform given by net toroidal currents. $\iota(r)_{\mathrm{curr}}$ is proportional to $I(r)/r^2$, with $I(r)$ the toroidal current enclosed in the plasma volume of radius r. The $1/r^2$ dependence, together with W7-X being a low shear stellarator, makes the rotational transform very sensitive to local changes of toroidal current, such as the bootstrap current or ECCD. In particular, the ECCD profile is generally well localised and can strongly modify the rotational transform.

The ECRH system at W7-X is very flexible and allows for a wide range of power deposition positions. In figure 3.2 we show an example of the propagation and the absorption of two different ECRH beams for the so-called *on-axis* (left column) and *off-axis* (right column) depositions. Qualitatively, the ECCD is driven within $r_{\mathrm{eff}}/a < 0.2$ in the first case and between $0.2 < r_{\mathrm{eff}}/a < 0.5$ in the second case. Additionally, the current is in *co-direction* if the rotational transform is increased and in *counter-direction* if it is decreased. In order to estimate how a net toroidal current can modify the rotational transform, we develop a 1-D cylindrical model and solved a current diffusion equation, using realistic plasma parameters. The procedure is described as follows:

- The plasma parameters used in the following calculations are based on the typical ECCD experiments (chapter 4) at W7-X, which are characterised by $T_e(r = 0) \approx 5\,\mathrm{keV}$, low electron density ($n_e \approx 2 \cdot 10^{19}\,\mathrm{m}^{-3}$) and low ion temperature $T_i = 1\,\mathrm{keV}$. The parallel Spitzer resistivity is calculated as $\eta_{\mathrm{sp}} = 1.03 \cdot 10^{-4} Z_{\mathrm{eff}} \log\Lambda/(1.96 T_e^{3/2}) \approx 2.5Z\,10^{-9}\Omega\mathrm{m}$, where Z is the atomic number [91]. These experiments were conducted in a helium plasma. The ratio of kinetic pressure $p = n_e T_e + n_i T_i$ and magnetic pressure is defined as $\beta = p/(B^2/2\mu_0)$. The typical experiments have a volume averaged plasma beta of $<\beta>\approx 0.2\%$ Therefore, contribution of the pressure to the plasma equilibrium

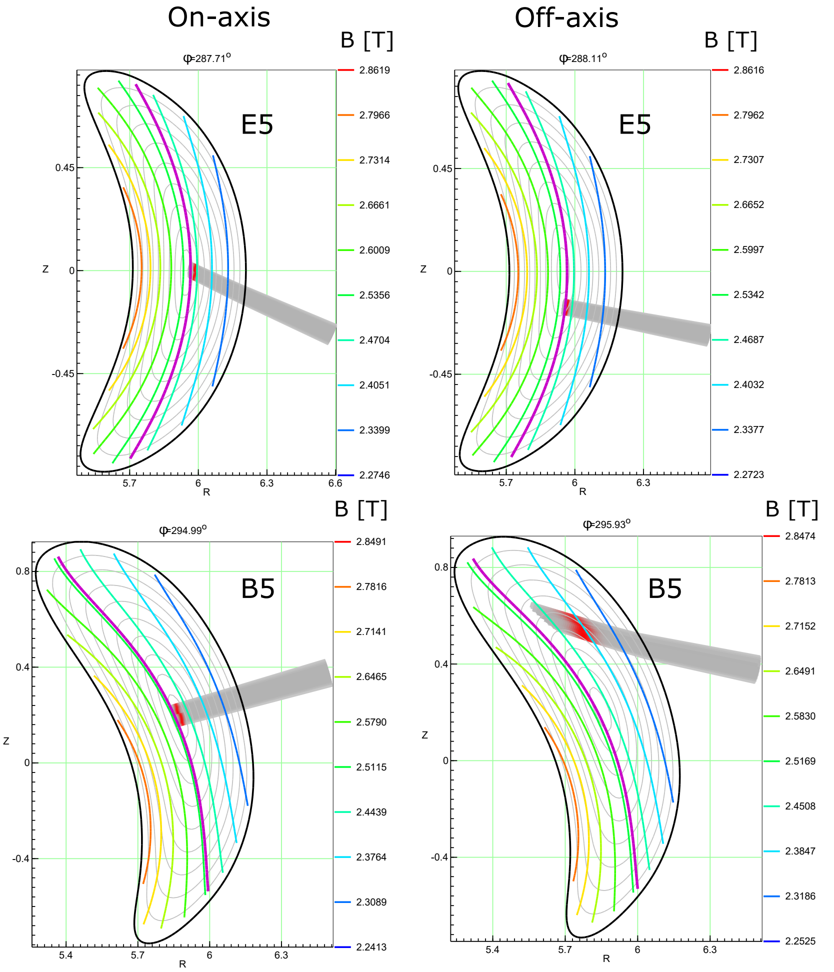

Figure 3.2.: Ray-tracing calculations performed with TRAVIS. In the left column the propagation of two beams for the on-axis heating scheme is shown. In the right column, the propagation of the same beams with an off-axis heating scheme is depicted. The purple curved lines indicate $B = 2.5\,\mathrm{T}$.

can be neglected and a low bootstrap current, which depends on the pressure gradient, is expected.

- The current density $j_{\mathrm{tot}}(r,t)$ is composed of three terms: $j_{\mathrm{BS}}(r)$, $j_{\mathrm{ECCD}}(r)$, and $j_{\mathrm{ind}}(r,t)$: $j_{\mathrm{BS}}(r)$ is the bootstrap current (calculated by the NTSS code [86]), $j_{\mathrm{ECCD}}(r)$ is the ECCD, calculated by the ray-tracing code TRAVIS 2.2 and $j_{\rm ind}(r,t)$ is the shielding current. The plasma, due to Lenz's law, generates the latter to oppose magnetic flux changes. Two characteristic times can be distinguished: the L/R time ($\tau = L/R$) and the resistive time. The first describes the timescale for the current to develop (equation (1.35)). The latter is the characteristic time for the resistive diffusion $\tau_\eta = \mu_0 l^2/\eta_0$, where η is the plasma resistivity and l a characteristic length. The macroscopic resistive time of the system can be estimated by setting $l = a$, where a is the plasma minor radius. Using the aforementioned plasma parameters, $\tau_R \approx 125 Z^{-1}\,$s.

- The rotational transform is divided into two terms $\iota = \iota_{cf} + \iota_{\rm curr}$. ι_{cf} is calculated by the code VMEC [2], using the aforementioned plasma parameters and without a net toroidal current, i.e. $I_{\rm tor} = 0$. The toroidal current contribution to the rotational transform is calculated by solving a diffusion equation. Additional recalculations of the magnetic equilibrium due to toroidal current changes have not been performed, neglecting the feedback of the current evolution on the equilibria. We emphasize that we use this model to estimate the time for ι to cross a low order rational value. As we will show, this occurs in about 100 ms. From an experimental point of view, the net toroidal current is small, due the presence of shielding current ($I_{\rm tor} \sim 0\,$kA, see equation 1.35,the experimental data in figure 4.1). In fact, additional VMEC equilibrium calculations would not significantly change the magnetic flux surface topology, due to the low β and the current densities well localised close to the axis.

- Finally, the calculations are performed using a 1-D cylindrical geometry. A 1-D cylindrical model is insufficient to describe the complexity of the stellarator geometry but can be used to provide a first quantitative guess of the current drive effects on the rotational transform profile. This approach is justified by the fact that, for the vast majority of the experiments, ECCD is driven in the proximity of the axis, inside $r_{\rm eff}/a < 0.25$. This fact, along with being W7-X a large aspect

[2]The VMEC code is used to solve the magnetohydrodynamic force balance $\mathbf{j} \times \mathbf{B} = \nabla p$ in a 3-D geometry. More information can be found in [92].

stellarator ($R/a \approx 10$) allows for using a 1-D cylindrical approximation as a first step to evaluate the current profile evolution.

We will now present the toroidal current density evolution for an on-axis ECCD deposition, using the experiment that will be presented in figure 4.1 as a reference, in order to estimate the typical time scale for ɨ to cross low order rational values. The ECCD profile is artificially shifted away from the position $r = 0$, in order to avoid computational issues and an overestimation of the modified rotational transform. The peak is around $r \approx 0.1\,a$ and the current profile is located within $r/a < 0.25$. $j_{\mathrm{BS}}(r,t)$ has a very broad profile. These two components are plotted in figure 3.3 (a) (dashed lines). If $j_{\mathrm{ECCD}}(r)$,$j_{\mathrm{BS}}(r)$ are constant in time, $j_{\mathrm{ind}}(r,t)$ evolves as:

$$\mu_0 \frac{\partial j_{\mathrm{ind}}(r,t)}{\partial t} = \frac{1}{r}\frac{\partial}{\partial r}\left(r\frac{\partial}{\partial r}(\eta_{\mathrm{sp}}(r) j_{\mathrm{ind}}(r,t))\right) \tag{3.2}$$

with μ_0 being the vacuum permeability, $\eta_{\mathrm{sp}}(r)$ the Spitzer plasma resistivity and $j_{\mathrm{ind}}(r,0) = -(j_{\mathrm{ECCD}}(r) + j_{\mathrm{BS}}(r))$. In figure 3.3 the numerical solution of equation 3.2 is plotted for three different timesteps (solid lines). The shielding current diffuses mainly towards the centre, allowing for a strong and localised current density increase. In the right plot of figure 3.3 the sum of currents is displayed for different timesteps. In 1-D cylindrical geometry, the rotational transform produced by the toroidal current can be written as:

$$\text{ɨ}_{\mathrm{curr}}(r) = \frac{\mu_0 R_0 I_{\mathrm{tor}}(r)}{2\pi B_{\mathrm{tor}} r^2}. \tag{3.3}$$

Therefore, because the toroidal current and the rotational transform are connected, it is possible to express equation 3.2 as:

$$\frac{\partial \text{ɨ}_{\mathrm{ind}}}{\partial t} = \frac{1}{\mu_0 r}\frac{\partial}{\partial r}\left[\frac{\eta_{\mathrm{sp}}}{r}\frac{\partial}{\partial r}\left(r^2 \text{ɨ}_{\mathrm{ind}}\right)\right]. \tag{3.4}$$

Equation 3.4 describes the resistive evolution of the rotational transform. Renormalising equation 3.2 with respect to the resistive time of the system $\tau_\eta = \mu_0 a^2/\eta_0$, where η_0 is the Spitzer resistivity in the core and a is the minor plasma radius:

$$\frac{\partial \text{ɨ}_{\mathrm{ind}}}{\partial \tau} = \frac{1}{\hat{r}}\frac{\partial}{\partial \hat{r}}\left[\frac{\hat{\eta}}{\hat{r}}\frac{\partial}{\partial \hat{r}}\left(\hat{r}^2 \text{ɨ}_{\mathrm{ind}}\right)\right] \tag{3.5}$$

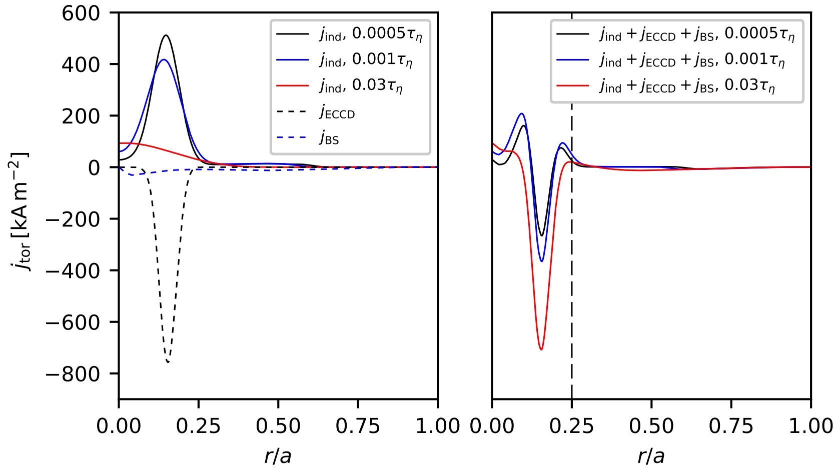

Figure 3.3.: Modelled current density profiles for different timesteps. On the left image, $j_{\mathrm{ECCD}}(r)$, $j_{\mathrm{BS}}(r)$ (dotted lines) and $j_{\mathrm{ind}}(r,t)$ are plotted. $j_{\mathrm{ind}}(r,t)$ represents the numerical solution of equation 3.2, without taking into account any current redistribution after a crash. The shielding current $j_{\mathrm{ind}}(r,t)$ diffuses towards the centre and a net current is created. On the right image the sum of the two components is displayed. The dashed vertical line represents the position of r_{inv} at the beginning of the experiment.

with $\tau = t/\tau_\eta$, $\hat{r} = r/l$ and $\hat{\eta} = \eta_{sp}/\eta_0$. The rotational transform of the system is finally given by equation 3.1, with $\bar{\iota}_{\mathrm{curr}}(r,t) = \bar{\iota}_{\mathrm{ind}}(r) + \bar{\iota}_{\mathrm{ECCD}}(r) + \bar{\iota}_{\mathrm{BS}}(r)$, the latters being respectively the rotational transform modifications due to stationary ECCD and stationary bootstrap current, i.e. the modifications of $\bar{\iota}$ after several L/R times. At $t = 0$, the initial condition is $\bar{\iota}_{\mathrm{ind}}(r, t = 0) = -(\bar{\iota}_{\mathrm{ECCD}}(r) + \bar{\iota}_{\mathrm{BS}}(r))$. The ECCD modifies the rotational transform and a low order rational value is reached on the order of $0.0012\tau_\eta \approx 74\,\mathrm{ms}$, which is consistent with the measured time for the first sawtooth to appear. The red curve represents the case when almost the whole shielding current is dissipated. A double crossing of $\bar{\iota} = 1$ is possible, although the values close to the magnetic axis $(r = 0)$ should carefully be interpreted, due to the $1/r^2$ dependence. The dominant contribution is given by ECCD, which is deposited close to the axis with a strongly peaked profile. For the calculated current profiles, the contribution of the bootstrap current inside r_{inv} i.e. for $r/a < 0.4$ is less than $10\,\%$, which indicates

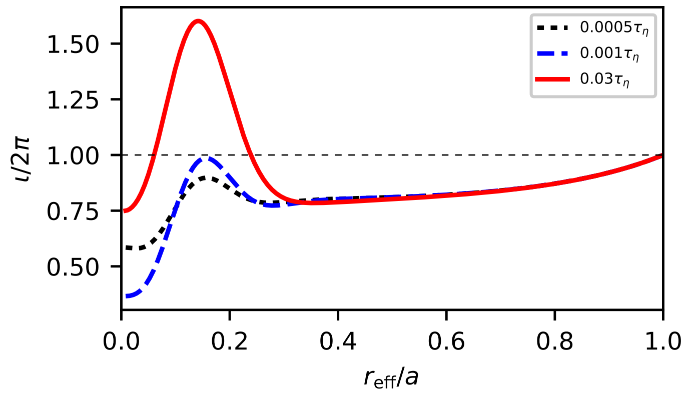

Figure 3.4.: Modelled rotational transform profile modified by ECCD for different times. Plotted curves represent the solution of 3.4.

that the dominant contribution to the rotational transform is given by the ECCD.

Since the sawtooth crash can introduce significant changes on the current profile, we presently use this model to estimate the ι profile at the beginning of the experiment until the first sawtooth crash appears. It is interesting to notice that the induced current diffuses toward the plasma centre, thus creating a region in which a current of the opposite sign is present. This is visible also in figure 3.4, where in the proximity of the centre, the ι is decreased,the rational values of $\iota = 1/2$ or $\iota = 5/6$ are crossed. Let us consider two different cases, one with a more off-axis ECCD and one with on-axis counter-ECCD. We will neglect the bootstrap current contribution, since it does not significantly contribute as it was previously shown.

For the off-axis co-ECCD case (see figure 3.5), no qualitative differences are found with respect to the case analysed in figure 3.3. $\iota = 1$ is reached five times slower than in the on-ECCD case (figure 3.4). This is a consequence of $I(r)/r^2$ in equation (3.3) and means that at equal plasma current, the rotational transform changes are stronger for smaller r. Additionally, it is found that the accumulation of shielding current in the centre is weaker.

The counter-ECCD case (figure 3.6) has a current profile similar to the one analysed in figure 3.3, but with the current in the opposite direction. The diffusion of the shielding current towards the centre leads to the crossing

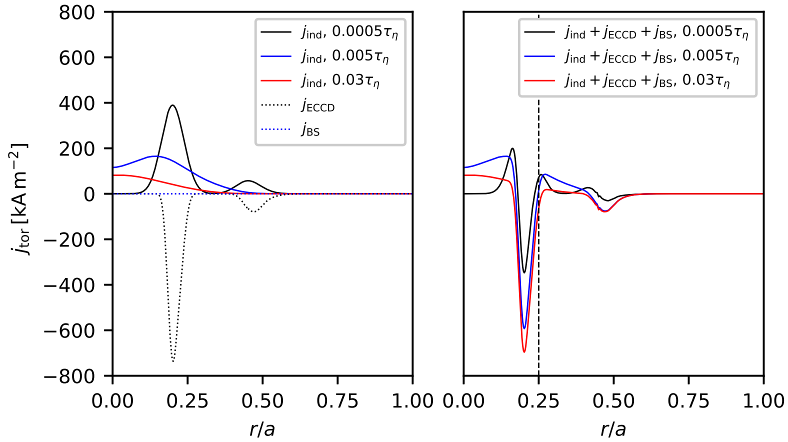

(a)

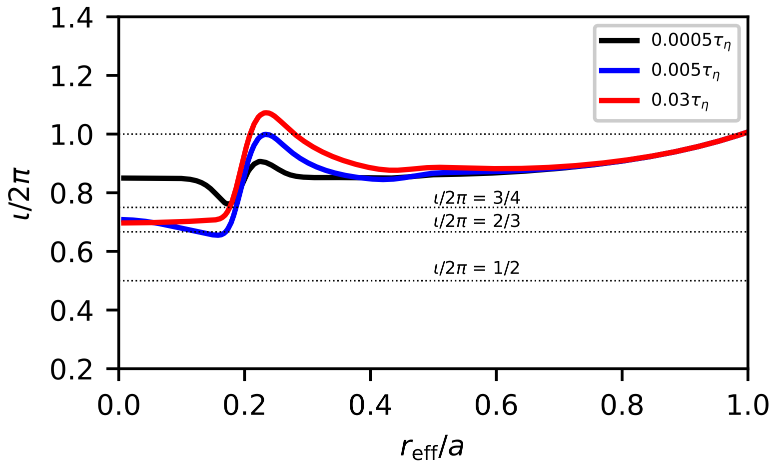

(b)

Figure 3.5.: $j(r)$ and ι profiles for different timestep for off-axis current drive. The current drive is deposited in the region $0.2 < r_{\text{eff}}/a < 0.5$.

.

of $\iota = 1$. Most importantly, it has to be noted that counter-ECCD leads to a strong decrease of ι and several resonances (dashed lines in figure 3.6b, $\iota = 1/2$, $2/3$, $3/4$ ...) are crossed.

As it will be show in the next chapter, this simple 1-D model is able to

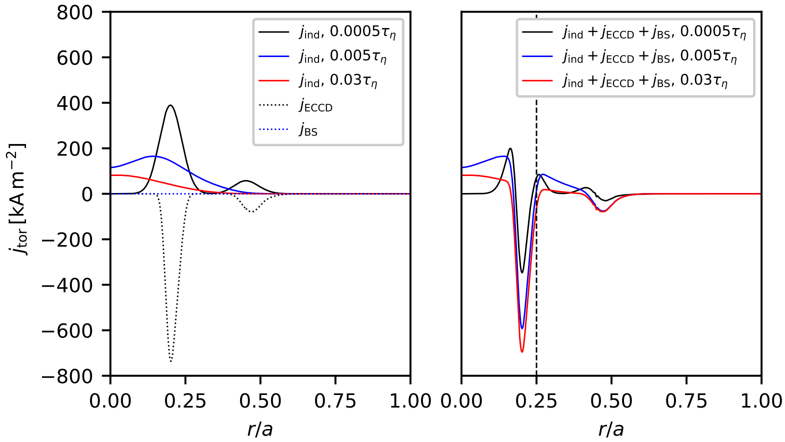

(a)

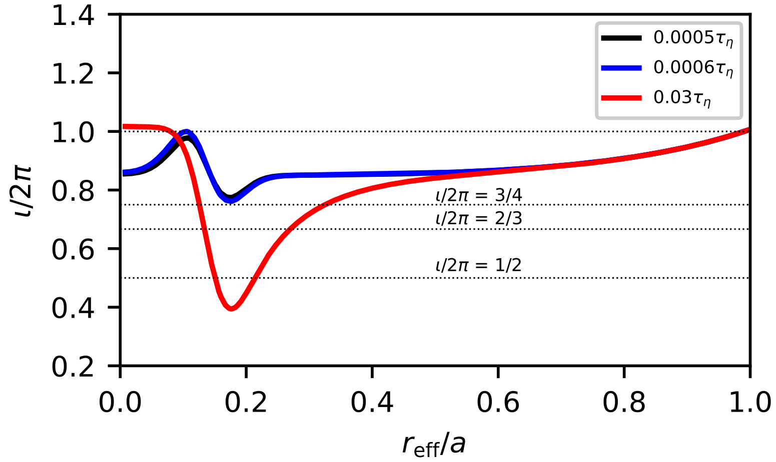

(b)

Figure 3.6.: $j(r)$ and ι profiles for different timestep for counter-current drive.

.

estimate the times for the instability to be detected. More accurate models, in which the post-crash current redistribution is taken into account are under development and will provide more insights regarding the modified rotational transform, but are beyond the scope of this thesis.

Chapter 4.

Sawtooth crashes at W7-X [1]

Sawtooth crashes are periodic relaxations of the central electron temperature and density. Ideal-MHD calculations, performed before the start of W7-X operations, suggested W7-X to be stable to the $(m, n) = (1, 1)$ internal kink instability [93], generally related to the sawtooth crashes. However, these instabilities were detected in most of the experiments with ECCD [70]. As shown in chapter 3, localised ECCD can drastically change the rotational transform profile,low order resonant surfaces can be crossed, thus making the plasma susceptible to instabilities.

In this chapter the main features of the sawtooth crashes will be analysed. We begin the analysis with long experiments ($> 10\,\mathrm{s}$) where central heating and current drive was provided. It will be shown that in this case the crashes are stronger and therefore it is easier to identify and analyse them. It is found that the slow development of I_{tor} plays a crucial role in making the sawtooth crashes bigger and stronger in time by shifting the position were $\iota = 1$ is reached. Additionally, up to two types of sawteeth, characterised by a different amplitude, were detected. For the stronger events, a mode consistent with $(m, n) = (1, 1)$ is found, while for the second type of crash the mode analysis was not conclusive.

The high flexibility of W7-X allowed for studying the sawtooth crashes with different heating schemes and magnetic configuration. In section 4.5, the main results from the on-axis co-ECCD (rotational transform is increased) experiments are compared with off-axis heating and counter-ECCD (rotational transform is decreased). In 4.6, we briefly show that for different magnetic configurations, no relevant differences are found. Examples of current deposition profiles for the experiments we mention in this chapter

[1]Part of this chapter was published in [70]

are reported in the appendix.

4.1. Sawtooth crash overview for on-axis experiments

We will start the analysis with the experiments *20171206.025* (figure 4.1). This experiment allows for a characterisation of the main crash features which are commonly observed in other ECCD experiments. The core electron temperature is about $5-6\,\mathrm{keV}$ and the line integrated density $< n_e >$ about $2-2.5\cdot 10^{19}\,\mathrm{m}^{-3}$. At these T_e and n_e values, the coupling between ions and electrons is weak, therefore the ion temperature T_i is about $1\,\mathrm{keV}$. The toroidal current I_{tor} is given by the sum of several components, as explained in the previous chapter, and develops on the timescale of $\tau = L/R \approx 9\,\mathrm{s}$. The ECCD is generated by the oblique injection of two ECRH beams, depositing power around $r_{\mathrm{eff}} \approx 0.15\,a$. The ECCD is not generated in the centre, but slighty outside due to the Doppler shifted absorption. The stationary I_{ECCD} value is simulated by TRAVIS and is expected to be $-14\,\mathrm{kA}$ [2]. The stationary bootstrap current is calculated with NTSS and is about $-4\,\mathrm{kA}$. The ECCD profile and its time evolution is displayed in chapter 3, figure 3.3. In figure 4.1, the plasma parameters from different plasma diagnostics for the whole experiment are presented, while in figures 4.2a,4.2b two selected zooms (from 3.4 s to 3.65 s and from 15.5 s to 15.75 s) are shown. Central temperature crashes start to appear a hundred milliseconds after the plasma start-up. Strong and repetitive temperature crashes are visible in the panel (b), where two ECE channels are plotted. The channel in red shows the core T_e, while the channel in blue measures T_e at about $r_{\mathrm{eff}} = 0.4\,a$, where $a = 0.5$ is the plasma minor radius. The core timetrace shows the presence of two types of crashes, with different amplitude and period. Both crash types are characterised by a drop of T_e in the core. The central T_e drop is generally between $30-60\,\%$ for the strongest crashes and recovers in about $5-20\,\mathrm{ms}$. The strongest crashes are visible also in the external timetrace (in blue). In figure 4.2a a temporary T_e increase is

[2] The experiments in this section were conducted with a configuration in which the magnetic has an opposite direction with respect to standard configuration. For this reason, the co-current has a negative sign and the counter-current a positive sign.

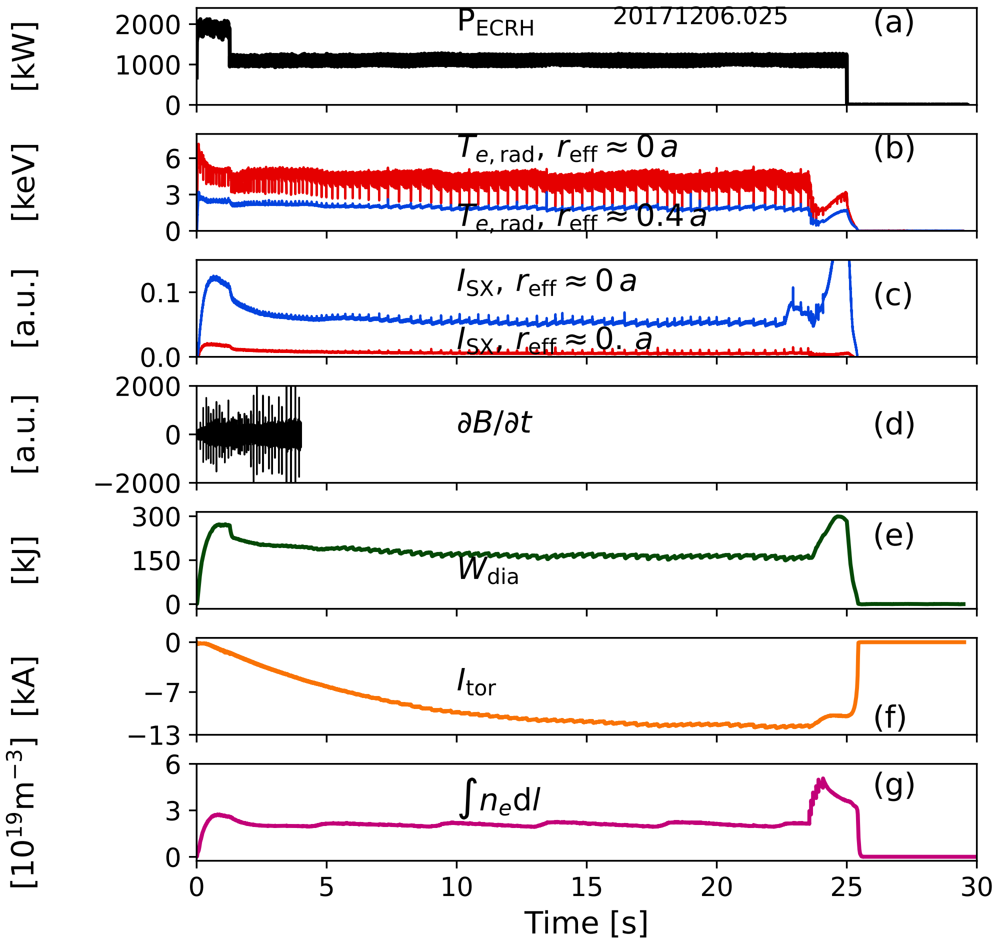

Figure 4.1.: Overview of the experiments *20171206.025*. In (a) the ECRH power is plotted. In (b) the T_e detected by a core ECE channel (red) and a mid-plasma ECE channel (blue) is plotted. The temperature crashes can be seen. In (c) the timetraces of a central (blue) and a mid-plasma (red) x-ray LOS are plotted. In (d) the timetrace from a Mirnov coil are plotted. The data acquisition stopped after 5 s. In (e), (f) and (g) the stored plasma energy W_{dia}, the toroidal current I_{tor} and the line integrated electron density $\int n_e dl$ are plotted.

visible in correspondence with the central T_e drop, thus indicating the hot plasma core has been expelled and redistributed. On the other hand, the blue timetrace in figure 4.2b shows a small temperature decrease for the

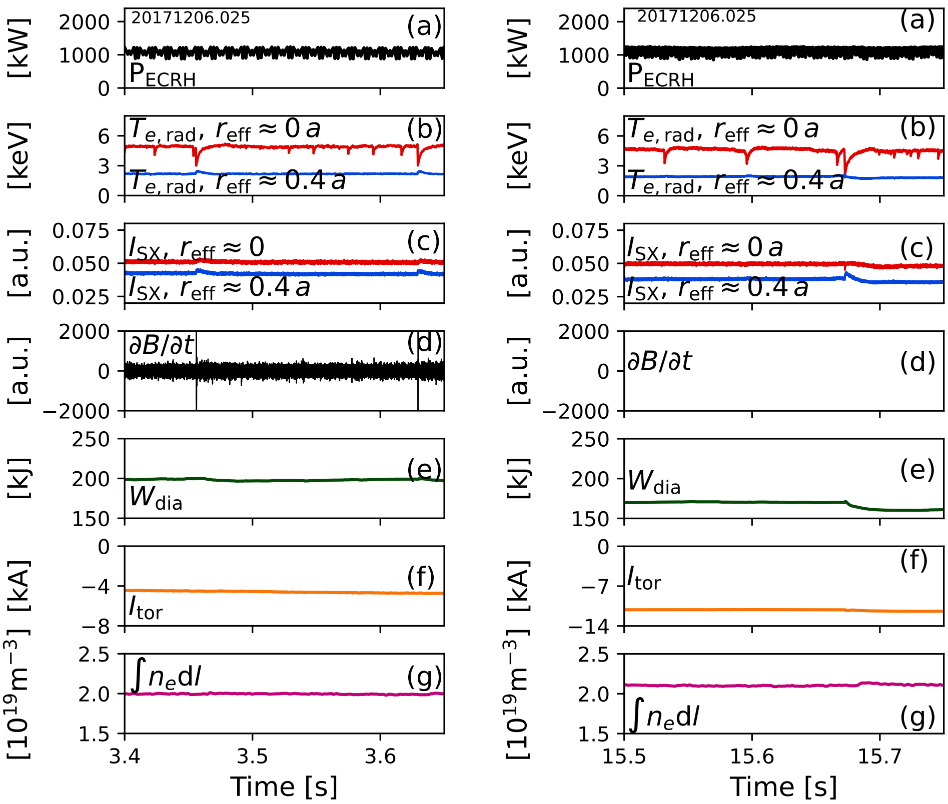

(a) **(b)**

Figure 4.2.: Selected time windows for experiment *20171206.025* (figure 4.1).
.

crash at 15.67 s, which means that the volume affected by the temperature crash is bigger than the crash at about 3.45 s in figure 4.2a. The weaker crashes that occur between two stronger crashes are hardly visible in the external timetraces because of the narrower region they affect.

The soft x-rays intensity emission I_{SX}, measured by a core and a mid-plasma ($r_{eff} \approx 0.4\,a$) line of sight (LOS), is plotted in panel (c). The interpretation of the crash dynamic is more difficult, since both timetraces show an increase in the intensity emission. Moreover, smaller events are not detected. There can be several explanations for the discrepancy between the x-ray signals and T_e measured by ECE. First of all, the x-ray measurement is a line-integrated measurement and therefore less effective in detecting local changes. Moreover, I_{SX} is proportional to $\sqrt{T}_e n_e^2 Z_{\mathrm{eff}}$. Therefore, the stronger dependence on n_e than T_e can significantly influence the emitted signal and does not allow to decouple the temperature dynamics from the density dynamics.

In panel (d), the temporal variation of the magnetic field (in arbitrary units) is plotted. $\dot{\mathbf{B}}$ is directly related to the perturbations, to which the plasma is subjected and that are created by the sawtooth crash.

The diamagnetic plasma energy is plotted in panel (e), where drops of the stored plasma energy (about 10 kJ, corresponding to 5 % of the whole energy and consistent with the calculated drop in kinetic energy) are detected by the diamagnetic loops. The time for the energy to recover is on the order of 200 ms, one order of magnitude slower than the central temperature recovering time mentioned above. It should be noted that smaller events have little to no effect on the stored energy. The toroidal current I_{tor} is visible in panel (f). I_{tor} increases fast at the beginning of the experiment and tends to converge to its stationary value at the end.

The main observations can be summarised as follows: 1) localised ECCD is responsible for sawtooth-like crashes. 2) Up to two different crash types with different amplitudes are observed for on-axis ECCD. 3) The crash amplitude increases as a function of time. In the next chapter we provide a possible explanation for the aforementioned phenomena.

4.2. Crash classification

The presence of different crash types is important and interesting for the following reasons: it allows to validate numerical results and codes in complicated geometries, can potentially be used to obtain informations about how the rotational transform is modified and how the different instabilities may be triggered.

Crashes are detected by applying to ECE data a ridge detection algorithm, based on continuous wavelet transform (CWT) (see chapter 2.3). We study the evolution of the three main parameters: the inversion radius, the maximum amplitude during a crash and the crash period. An example of how the first two of these parameters are defined can be seen in figure 4.3b. The inversion radius is calculated for both HFS and LFS of the plasma

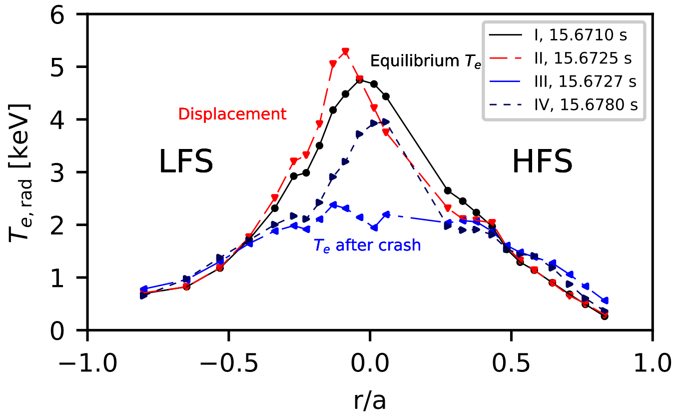

(a)

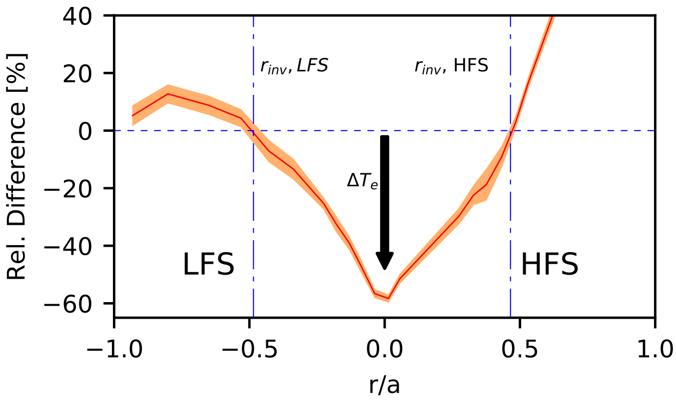

(b)

Figure 4.3.: (a): ECE temperature profiles during a temperature crash. I) represents the T_e profile before the crash, II) the core displacement, III) the profile after the crash and IV) the profile during the re-heating phase. The relative T_e change between I) and III) is used to estimate the inversion profile, which in plotted in (b). From the inversion profile ΔT_e and r_{inv} are calculated.

.

and it is defined as the radial position where the temperature remains constant before and after the crash. The maximum amplitude, ΔT_e, is defined as the maximum relative change between the T_e profile before and after the crash. The crash period represents the temporal interval between two crashes of the same type and it will be introduced later on, after we will have shown that the division into more crash types suits our dataset.

A division into groups can be achieved by setting a threshold for certain crash parameters, such as r_{inv} or ΔT_e, so as to assign the crashes, whose parameters are below or above the selected threshold, to one or to the other group, respectively. However, for our dataset this approach was not always possible, since the crash parameters evolve over time and, therefore, a division based on a threshold parameter value might be misleading and can assign a certain crash to a wrong group.

Instead, data are divided into clusters using the DBSCAN clustering algorithm [94] and by taking into account $r_{\text{inv lfs}}$, $r_{\text{inv hfs}}$ and ΔT_e and I_{tor}. I_{tor} is not a crash parameter but it is used as a proxy for the temporal evolution, since it is expected to be a function of time and it influences the other crash parameters. The DBSCAN algorithm divides data into clusters, which are defined as regions of high point density separated by low point density regions in the parameter space. More information regarding the application to our dataset is discussed in the appendix A.2. In order to improve the statistics, we analyse the crash data for six experiments with comparable T_e, n_e, ECCD profiles and magnetic configurations.

Results are represented in figure 4.4, in which two clusters are shown. Every cluster is characterised by a different colour: red for smaller crashes and blue for the stronger crashes. The points which do not belong to any of the found clusters are represented in black.

From now on we will introduce the following formalism: Type-A crashes are the crashes belonging to the cluster with the higher ΔT_e and Type-B crashes those belonging to the cluster with lower ΔT_e.

The division into different clusters allows to evidence even more the dependence of bigger crashes on the toroidal current (fig 4.4b). The scatter matrix of the crash and plasma parameters is depicted in figure 4.5. In a scatter matrix the variables are plotted against each others, in order to show the relation between them. The division into clusters is confirmed by the good correlation (table 4.1a) between the current and the crash parameters of the type-A crashes. Correlations are weaker for type-B crash parameters (table 4.1b), but this can partially be explained by considering that these crash parameters are not only influenced by I_{tor} but also by the type-A crashes preceding them. No correlation is found between the crash

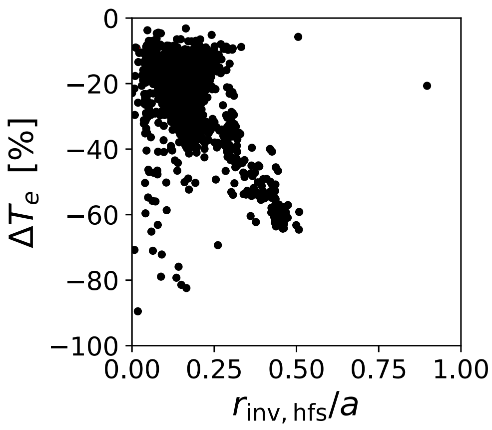

(a)

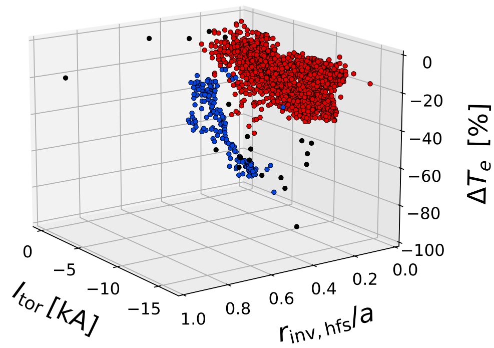

(b)

Figure 4.4.: Clustering performed on the data from six different ECCD experiments, with similar plasma parameters. Two different clusters are recognised.
.

parameters and the electron temperature T_e and the electron density n_e

	$r_{\text{inv,hfs}}$	$r_{\text{inv,lfs}}$	ΔT_e	τ_{crash}
I_{tor}	0.88	−0.61	−0.78	0.73

(a)

	$r_{\text{inv,hfs}}$	$r_{\text{inv,lfs}}$	ΔT_e	τ_{crash}
I_{tor}	0.39	−0.02	−0.13	0.02

(b)

Table 4.1.: Correlation (Pearson) between $|I_{\text{tor}}|$ and the crash parameters of type-A crashes in (a) and for type-B crashes in (b). The sign depends on how the parameter are defined. For instance ΔT_e is negative and therefore the correlation is negative.

The aforementioned analysis is based on the distribution of the crash parameters in the parameter space. A crucial question to be answered is whether the two crash types are also characterised by a different physical process or whether they are triggered by the same phenomenon and occurring at a different region of the plasma. In the following subsections we will describe the dynamics of the two processes and highlight similarities or differences.

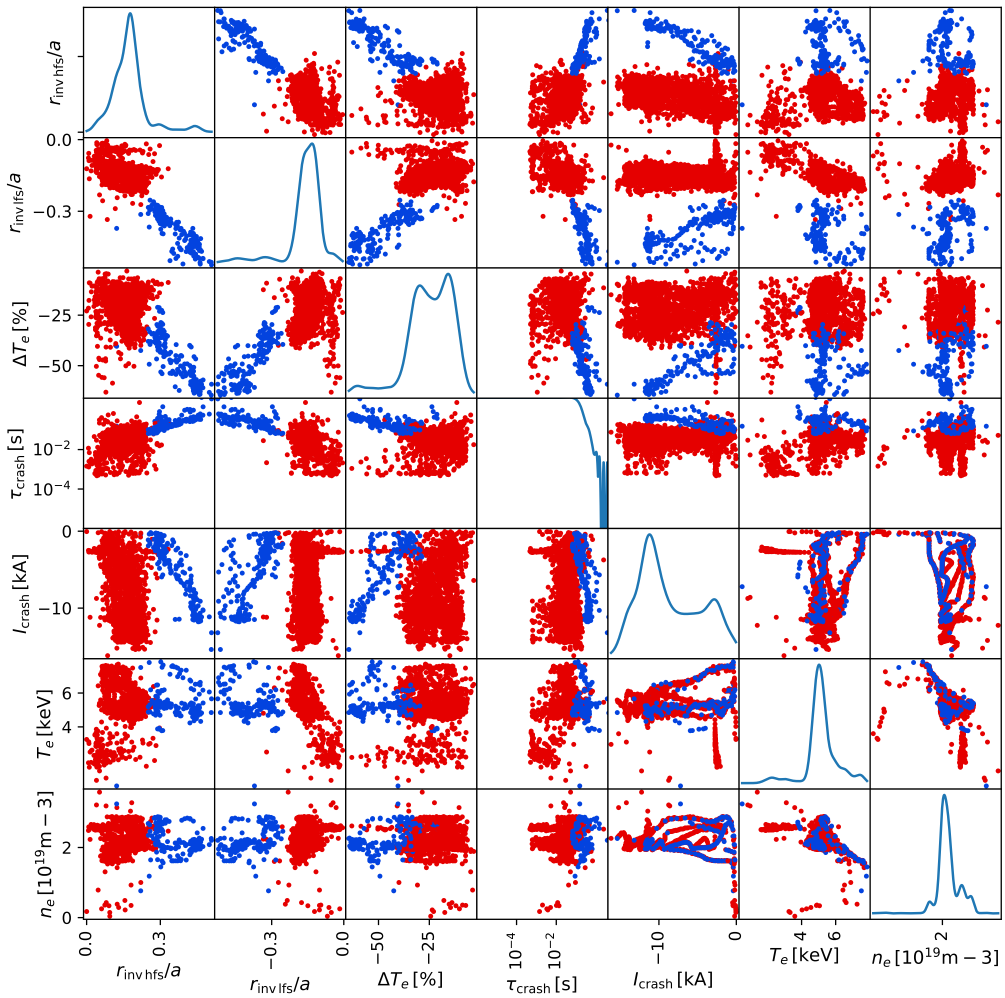

Figure 4.5.: Scatter matrix of the crash parameters and plasma parameters. Each color indicates one crash cluster. Type-A crashes (higher ΔT_e) in blue, type-B crashes in red.

4.2.1. Type-A crashes

The electron temperature profile, $T_e(r)$ is plotted in figure 4.3a for a typical type-A crash at different timesteps. At I), in black, the T_e at the equilibrium before the crash is shown. A fast core displacement (II, in red) then occurs within $100-200\,\mu$s, preceding the temperature drop. The crash happens in about $100\,\mu$s, during which the T_e profile within r_{inv} (defined in figure 4.3b) drops and flattens and the core energy is redistributed outside the inversion radius, causing a weak T_e increase. The re-heating phase (time step IV) depends on the amplitude of the crash and the involved region: for the crashes in this experiments the typical time is about $5-20\,$ms, faster than the time interval between two events. I_{tor} strongly influences the crash parameters, as it is shown in figure 4.4b. ΔT_e varies from about $30-35\,\%$ to $60-65\,\%$ for currents from 10 to 15 kA and r_{inv}/a changes from about 0.25 to 0.5. The same trend and the same values (with small differences due to slightly different plasma parameters) is detected in other experiments. In figure 4.6, τ_{crash} and r_{inv} of experiments *20171206.025*, *20171206.028* and *20171207.008* are plotted against I_{tor}. These experiments were performed with the same magnetic field configuration (axis magnetic field $B_0 = -2.52\,$T) and similar heating schemes. The r_{inv} of the three experiments overlaps very well, especially at late times of the experiments and indicates once again that the toroidal current plays a major role in setting the crash size. The r_{inv} discrepancies at the beginning of the experiments can be explained by the fact that I_{tor} represents the total toroidal current and not the current within a volume of radius r_{inv} and, therefore, differences of the current profile can be present. τ_{crash} values overlap at the beginning of every experiment (low I_{tor} values) and can show rather different values at higher I_{tor}. For instance, at the end of the experiment, the average τ_{crash} for *20171206.025* is $2-3$ times lower than in *20171206.028*.

Several models [29, 30, 95] predict that the current redistributes as a result of the crash and then develops until the plasma instability condition is reached again. We are not interested in *how* the current is redistributed, but in *how fast* it recovers for the next crash to be triggered. We are, in other words, interested in estimating how much time it takes for the current to make the plasma unstable again and if this is compatible with the crash period τ_{crash}. The resistive time τ_η describes the time scale for the current to diffuse. It is defined as $\tau_\eta = \mu_0 l^2/\eta_{\mathrm{sp}}$, where l is the typical scale of the

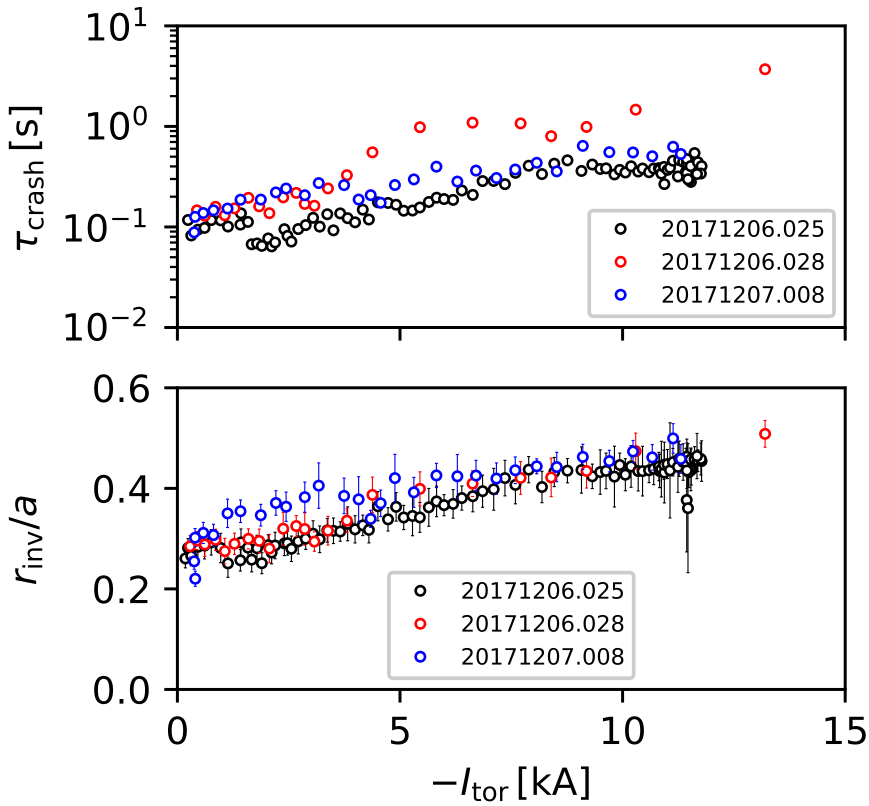

Figure 4.6.: Type-A τ_{crash} (top panel) and r_{inv}/a (bottom panel) as a function of I_{tor} for three different experiments.

system and η_{sp} the Spitzer resistivity. It is reasonable to expect τ_{crash} to scale with τ_η, thus to be similar for experiments whose τ_η are comparable. We do not directly estimate the relation between τ_{crash} and τ_η. Instead, we compare the ratios of τ_{crash} of different experiments, i and j, with the ratios of τ_η for the same experiments. The ratio can be written as follows:

$$\frac{\tau_{\eta\, i}}{\tau_{\eta\, j}} = \left(\frac{\mu_0 l^2}{\eta_{\text{sp}}}\right)_i \left(\frac{\eta_{\text{sp}}}{\mu_0 l^2}\right)_j \approx \frac{Z_{\text{eff}\, j}}{Z_{\text{eff}\, i}} \left(\frac{T_{e\, i}}{T_{e\, j}}\right)^{3/2} . \tag{4.1}$$

Since generally r_{inv} for different crashes agree very well, especially at higher currents, it is reasonable to assume that l be the same for the three experiments. For i = *20171206.025* and j =*20171207.008*, the ratio of the resistive times is $\tau_{\eta\,i}/\tau_{\eta\,j} = 0.87 \pm 0.22$ and the ratio between the crash periods (for $I_{\mathrm{tor}} < -8000\,\mathrm{kA}$) is $\tau_{\mathrm{crash}\,i}/\tau_{\mathrm{crash}\,j} = 0.77 \pm 0.26$. The two ratios are similar, thus indicating that the current evolution process and crash trigger happen on the same timescales for both the experiments. However, if we consider i = *20171206.028* and j =*20171207.008*, we obtain $\tau_{\mathrm{R}\,i}/\tau_{\mathrm{R}\,j} = 1.03 \pm 0.26$ and $\tau_{\mathrm{crash}\,i}/\tau_{\mathrm{crash}\,j} = 3.27 \pm 2.28$. The ratios strongly differ, which means that in *20171206.028* the crash trigger timescale is slower than the current diffusion.

An additional example is the last crash in this experiments, which occurs after 4 s from the previous crash. A similar observation is found for *20171206.030*. For the first 2 s, type-A crashes are detected. The type-A crash activity is replaced by type-B crashes. After about 14 s, a type-A crash is detected. The suppression of the type-A crashes is not understood and might have different reasons for which we propose two hypotheses. Either the presence of the type-B crashes influences the current evolution, making it slower, or the crossing of $\iota\!\!\!-= 1$ (or other resonant values) is not a sufficient condition for the crash to be triggered.

Theoretical works [96, 97, 93] regarding the W7-X plasma stability during ECCD experiments have just started. A better comparison between theoretical results and the experimental data requires measurements of the rotational transform profile, which are currently not possible.

4.2.2. Type-B crashes

Type-B crashes have similar characteristics as type-A crashes, i.e. a fast drop of the central T_e is detected along with a small increase in the temperature outside r_{inv}. However, the plasma volume affected by the crash is smaller than in a type-A crash. The crash time is of the same order of magnitude of the type-A crash (about 100 µs), but no precursors were detected. Crash parameters are not only influenced by the toroidal current but also by the presence of stronger crashes. It is possible to observe that ΔT_e , r_{inv} and τ_{crash} are reduced immediately after a big crash. In the following crashes, these three parameters increase again until values consistent with the ones before the crash is reached. This can be seen as an indication of a strong change and redistribution of the toroidal current following a type-A crash. However, the overall trend seems to be influenced as well by I_{tor}, since the average ΔT_e and r_{inv} for higher current values are larger

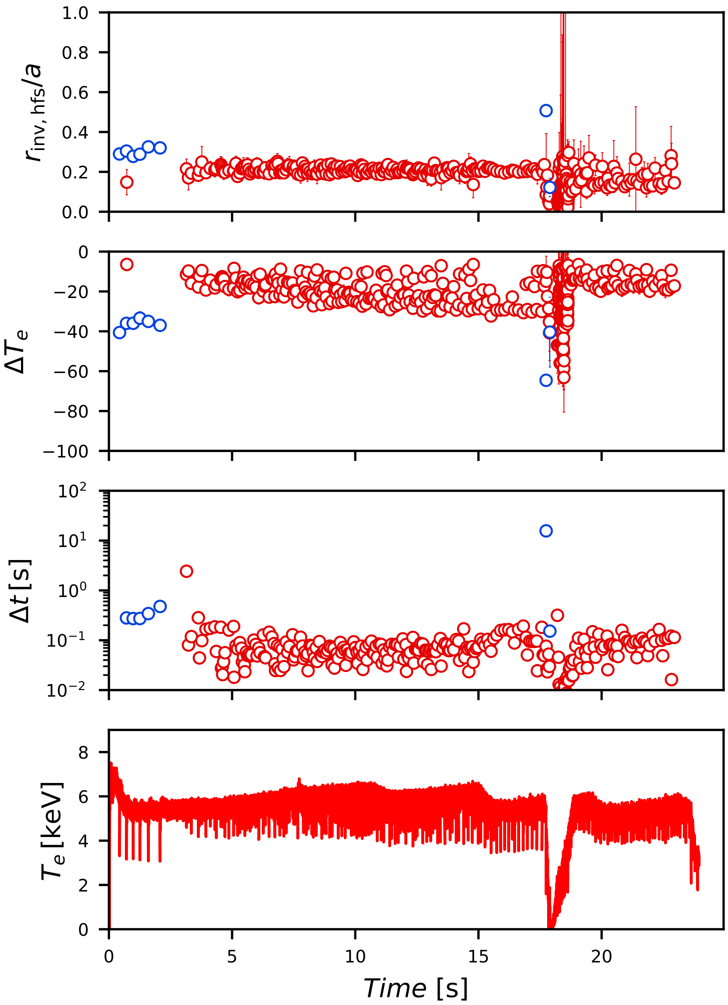

Figure 4.7.: Crash parameters of *20171206.030*. The blue and red dots represent the type-A and -B crashes, respectively. It is possible to see the absence of type-A crashes from $t = 2\,\mathrm{s}$ to $t = 17.5\,\mathrm{s}$.

than the average value at the beginning of the plasma discharge. The same comparison between crash parameters belonging to different experiments can be done for this type of crash as well, as plotted in figure 4.8. Also for the type-B crashes the values of r_{inv} overlap very well between different experiments. In figure 4.9, it is possible to notice that in both cases τ_{crash} is

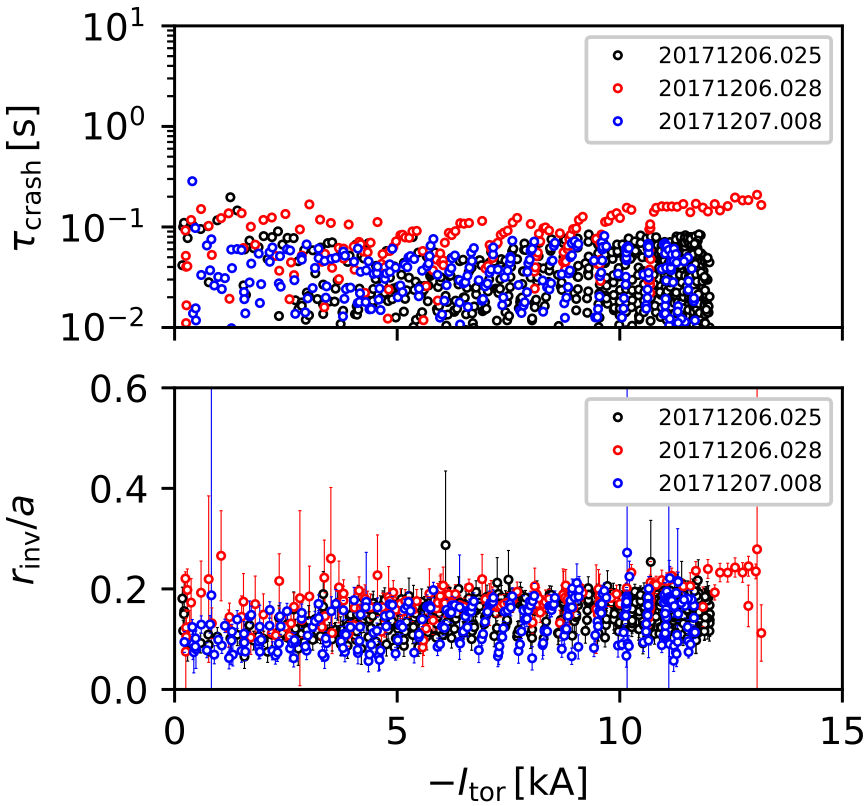

Figure 4.8.: Type-B τ_{crash} (top panel) and r_{inv}/a (bottom panel) as a function of I_{tor} for three different experiments.

non-monotonic, due to the influence of the type-A crash. However, the τ_{crash} in *20171206.028* (blue dots) shows a very fast recovery, followed by time window in which τ_{crash} is constant. The same is not visible in *20171207.008* (blue dots), where the reaching of a saturated value for τ_{crash} is probably interrupted by a type-A crash.

4.3. Mode Number estimation

The existence of crash precursors is extremely useful in studying and characterising an instability. In this work two main types of precursor phenomena

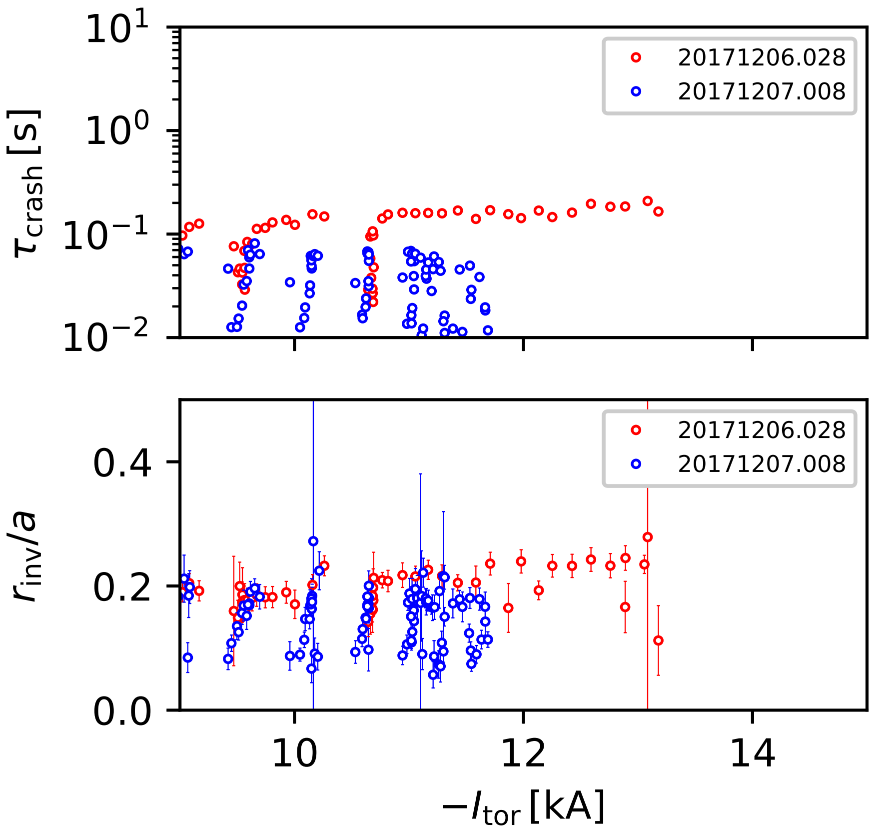

Figure 4.9.: Type-B τ_{crash} (top panel) and r_{inv}/a (bottom panel) as a function of $I_{\text{tor}} < -9\,\text{kA}$ for two different experiments.

were encountered. Oscillating precursors, which can in principle be easily studied by means of time-frequency analysis, and strong and fast displacement of the plasma core. In our case, oscillating precursors have a short lifetime and are generally not detected by the x-ray cameras and therefore are mainly studied by ECE. Magnetic diagnostics, which have a greater mode resolution, detect a strong oscillating signal after the crash. The signal is composed by several periodic oscillations, which are damped in about 100 µs. Frequencies depend on several factors, such as plasma parameters, but are one order of magnitude higher than postcursors that can be observed in the ECE signal after the crash itself. The typical frequencies that

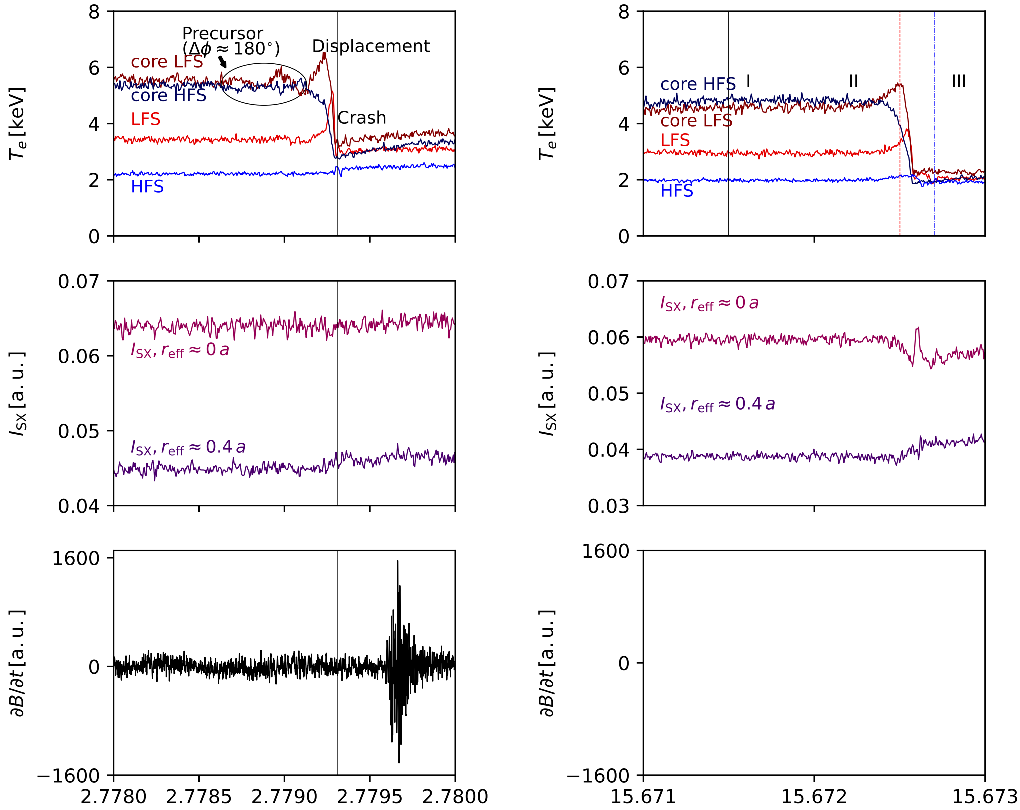

(a) **(b)**

Figure 4.10.: Precursor activity in *20171206.025*. In a) short-lived precursors and core displacement are observed before the crash. The crash is hardly detected by the x-rays and a strong oscillations is detected by the Mirnov coils after the crash. b) Crash without oscillating precursors. The core displacement is detected as well (time step II). The crash is visible also in the x-rays.
.

compose the detected signal seem to be related to a post-crash Alfvénic activity [84] and are detected only for the stronger crashes. It may be the case that the smaller crashes are too weak or too close to the magnetic axis for the perturbation they produce to be detected by the coils. During experiments using the *standard configuration* and co-ECCD, the magnetic coils did not detect any significant crash precursors and therefore they could not be used for mode analysis.

4.3.1. Oscillating precursors

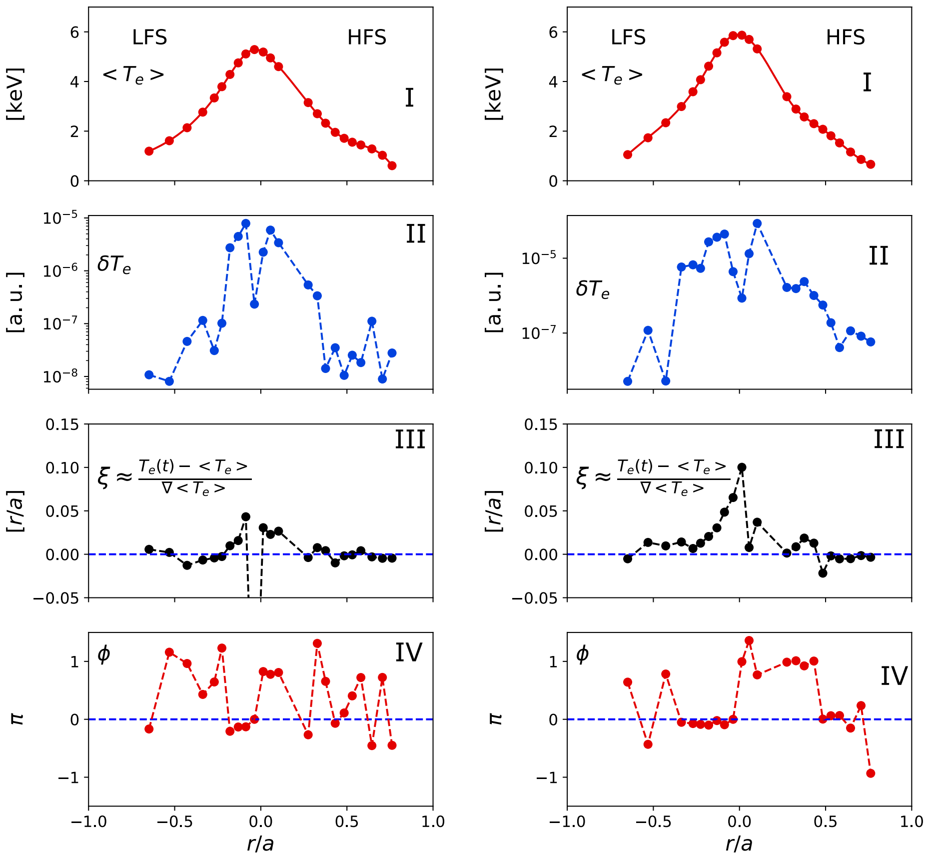

(a) (b)

Figure 4.11.: FFT analysis for precursors at $1.992 - 1.99254$ s (*20171206.025*) (a) and $13.523 - 13.5245$ s *20171206.028* (b). The smoothed pre-crash $\langle T_e \rangle$ profile, the power density of the dominant frequency, the radial displacement ξ and the relative phase between the precursor oscillations are plotted, respectively.

.

Crashes are occasionally preceded by short-lived precursor oscillations ($2-6$ kHz) and in most cases by a displacement of the plasma core. Precursors are not identified in x-ray data. The ECE timetraces of two HFS channels and two LFS channels are plotted in figure 4.10a. From $t = 2.7785\,\mathrm{s}$ to $t = 2.7791\,\mathrm{s}$, the two core channels show T_e oscillations 180° out of phase, consistent with an odd poloidal number.

Generally, the oscillating precursors for on-axis current drive are relatively weak and the cycle is too short for being properly analysed by means of a FFT. However, an example is provided in figure 4.11. Figure 4.11a shows the precursor analysis for the time window $t = 1.0615 - 1.0622\,\mathrm{s}$ (*20171206.025*), in which the smoothed pre-crash T_e profile (I), the power spectral density of the main Fourier component (II), the radial displacement $\xi(r)$ (III) and the relative phase between channels (IV) are plotted. Due to the small time windows and relatively weak oscillations, the phase relation between the core channels is not easy to interpret. However, a phase of π exists between the channels with the stronger oscillations, therefore the precursors are related to a perturbation with odd poloidal number. The oscillations for $|r/a| > 0.25$ are too weak for assessing the phase relations with respect to the core oscillations. Figure 4.11b shows a case (*20171206.028*, $t = 13.523 - 13.5245\,\mathrm{s}$) in which the precursor activity was stronger and detected by a wider number of ECE channels. Several LFS channels detect oscillations with a phase of π with respect to the HFS, thus confirming the mode has an odd poloidal number. An additional phase jump is present, around $r/a \approx 0.45$. A phase jump on the same side with respect to the axis is an indication for a magnetic island, thus indicating the mode has a non-ideal nature (chapter 3 in [16]). This is also confirmed by the displacement ξ, which changes sign in correspondence to the phase jump, thus confirming the existence of a magnetic island before the crash.

4.3.2. Core Displacement

A fast displacement of the plasma core is often detected, regardless of the presence of oscillating precursors (figure 4.10). The core displacement can be identified in the timetraces as the spike that precedes the crash. The T_e profile during the displacement can be seen in figure 4.3a where it is compared to the unperturbed T_e.

The contour plot in figure 4.12a can be used to visualise the dynamics of the core displacement. The two dotted lines represent the timewindow in which the crash phase occurs. Before that, it is possible to see a movement

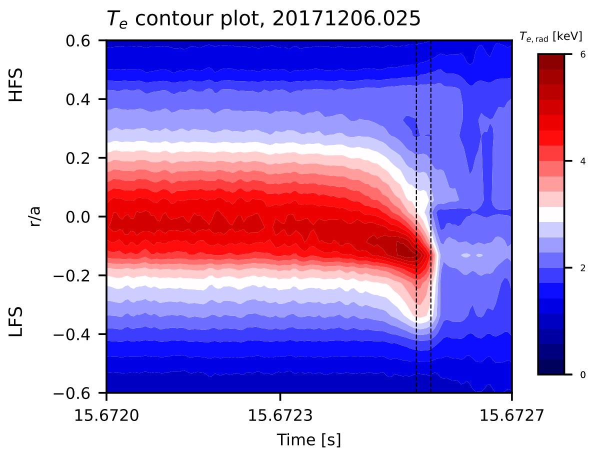

(a)

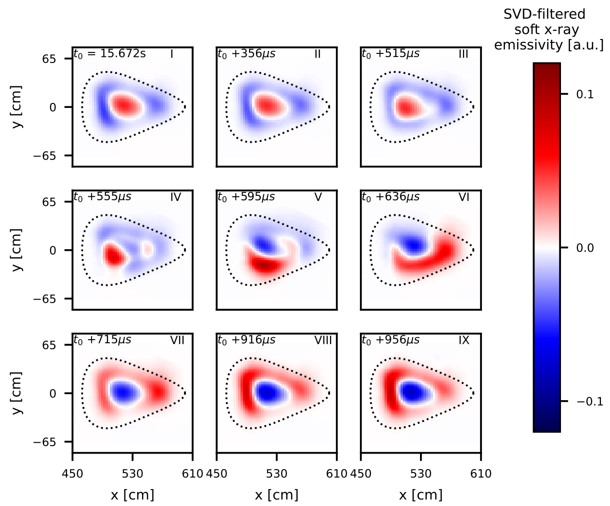

(b)

Figure 4.12.: ECE contour plot (a) and SVD-filtered x-ray tomography (b) of a crash preceded by the core displacement. The ECE detects an outwards core movement. The SVD-filtered x-ray tomography shows an inwards core movement (recognisable in the third and fourth tomograms).

.

from the centre to the LFS, which is caused by the core displacement. The T_e profile during the displacement is not poloidally symmetric and has the typical structure of an $m = 1$ mode. At the same time a region with flat T_e develops at the HFS, at $r/a \approx 0.4$. The temperature flattening is generally a good indication for the existence of a magnetic island. The island expands, spanning from $r/a \approx 0.22$ to $r/a \approx 0.45$ before the crash.

The core displacement is relatively strong and the x-ray tomographic reconstruction (4 µs of temporal resolution) was possible. The tomograms plotted in figure 4.12b are filtered by applying singular value decomposition (SVD) [98] to remove the dominant component of the emissivity which, for this case, consists of a constant value. The first tomogram represents the SVD-filtered data before the core displacement happens, which starts to be visible in the third tomograms and is completed in the fourth, showing a typical $m = 1$ structure. The tomography is also able to reconstruct the post-crash dynamics, showing a poloidal propagation of the expelled core (from the fifth tomogram). The redistribution is not isotropic and occurs in the direction of the electron diamagnetic drift. The ECE radiometer and the x-ray camera array are placed almost 180° apart in toroidal direction (figure 2.1). In figure 4.12, the ECE contour plot and the SVD-filtered x-ray tomography are compared. We observe that a horizontal outwards (inwards) movement in the ECE signal corresponds, in the x-ray tomography, to an inwards (outwards) movement. Comparing the movement directions of the x-ray signals with respect to ECE signals (figures 4.12a and 4.12b), we conclude that the toroidal mode number n has to be odd. The analysis of different crashes shows that the core could be displaced in every direction. ECE has only a 1-D horizontal line of sight and therefore only horizontal movements of the core can be detected. The existence of vertical displacements is confirmed by the soft x-ray tomography.

The existence of a preferred displacement position can be assessed by comparing the displacement detection in a LFS and an HFS channel. If the core displacements were purely horizontal or vertical, one would expect to detect by means of ECE (25 %) core displacements to the HFS, (25 %) to the LFS and to not detect any core movement in (50 %) of the cases. Considering again the experiment *20171206.025*, 62 type-A crashes are detected in the time window between $t = 3$ s and $t = 23$ s. 18 core displacement (29 %) are detected by an HFS channel, 15 (24 %) by a LFS channel and the remaining 29 (46 %) do not show any core displacement before the crash. This simplified analysis may suggest that the core displacement is isotropic, i.e. it does not clearly occur in a preferred direction.

4.4. Comparison with 1-D calculations

We have shown that the stronger crashes are characterised by mode numbers that do not contradict $(m, n) = (1, 1)$. An instability with these mode numbers will probably be destabilised in the proximity of the resonant surface with the same helicity, i.e. with $\iota\!\!\!- = 1$. Here, we present an estimation of $r_{\iota\!\!\!-=1}$ for type-A crashes based on two major observations. The first assumption is that the driven toroidal current is mainly generated in the proximity of the magnetic axis, therefore it is deposited inside the measured r_{inv}. The second observation concerns the bootstrap current, which has been calculated to be about 3 kA in the stationary phase, with a broad profile. Combining these assumptions, we can assume the toroidal current density to be mainly distributed inside r_{inv} and therefore that the measured toroidal current yields a good estimation of the toroidal current inside the inversion radius, i.e., $I_{\mathrm{tor}}(r = a) \approx I_{\mathrm{tor}}(r_{\iota\!\!\!-=1})$, where:

$$I_{\mathrm{tor}}(r_{\iota\!\!\!-=1}) = 2\pi \int_0^{r_{\iota\!\!\!-=1}} j_{\mathrm{tor}}(r)\, r\, \mathrm{d}r \approx I_{\mathrm{tor}} \tag{4.2}$$

with $r_{\iota\!\!\!-=1}$ being the radius where $\iota\!\!\!- = 1$ is crossed. The assumption that most of the current is distributed close to the magnetic axis allows us to estimate $\iota\!\!\!- = 1$ despite the lack of information about the real $j(r)$ profile. As plotted in figure 4.13a, the crossing position depends only on the integrated value of $j(r)$, which corresponds, under this assumption, to the experimentally measured toroidal current. Since we do not have any information about $j(r)$, the easiest assumption is to assume $j(r) = j_0\delta(r = 0)$, which indicates that the whole current lies on the plasma axis. This is physically not correct, but it has to be stressed that, as long as the toroidal current is within r_{inv}, any $j(r)$ will yield the same result on the estimation of $r_{\iota\!\!\!-=1}$. Under this assumption, equation 3.3 becomes:

$$\iota\!\!\!-_{\mathrm{curr}} = \frac{\mu_0 R_0}{2\pi} \frac{I_{\mathrm{tor}}(r = a)}{r^2} \tag{4.3}$$

We used equations (3.1) and (3.3) to estimate how the rotational transform is modified by the toroidal current. For every detected crash, we calculate $r_{\iota\!\!\!-=1}$, which is the radial position that solves equation (3.1) and compare it to the inversion radius (r_{inv}) of every crash as displayed in figure 4.13b. The temporal evolution of the calculated $r_{\iota\!\!\!-=1}$ position follows

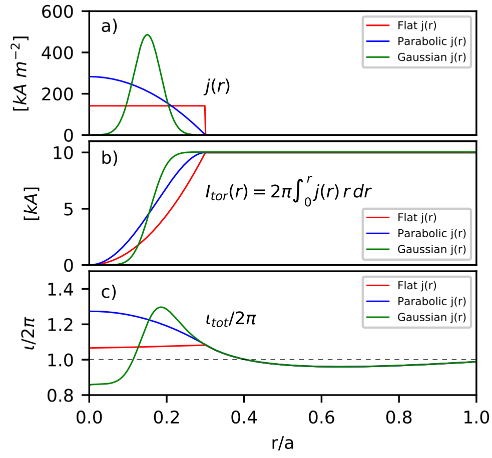

(a)

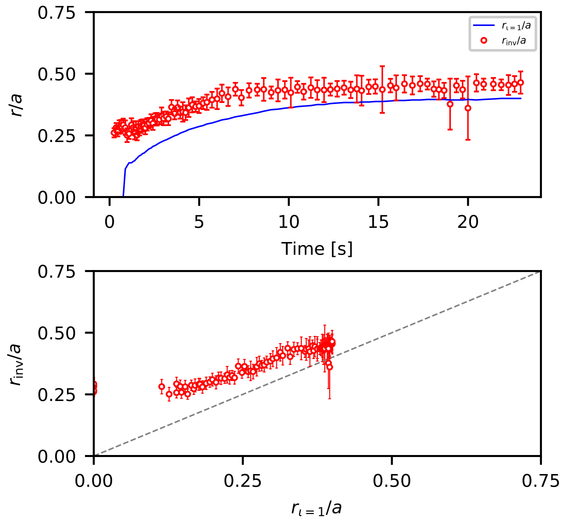

(b)

Figure 4.13.: a) sketch showing that different $j(r)$ profiles yielding the same I_{tor}, do not influence the position where $\iota = 1$ is crossed. In b), top panel, the $\iota = 1$ position (solid line) is estimated by assuming the whole I_{tor} is on the axis and it is compared with r_{inv} (red dots). In the bottom panel the two position are plotted against each other.

.

the trend of r_{inv} increase. While at the beginning of the discharge the two positions deviate approximately by 25 %, the deviation reduces with time, until the two datasets differ by less than 10 %. This deviation indicates that r_{inv} and $r_{\iota=1}$ might not coincide. The initial bigger difference can be explained by the fact that, at the beginning of the plasma discharge, due to the shielding current $j_{\text{ind}}(r,t)$, the toroidal current inside the inversion radius does not represent the whole toroidal current measured by the Rogowski coils. Although r_{inv} and $r_{\iota} = 1$ do not coincide, it is interesting to notice that they follow a similar trend (bottom plot of figure 4.13b) and their difference becomes constant at the end of the discharge, thus providing a reasonable explanation for the increase in r_{inv} at higher currents.

4.5. Comparison with other heating schemes

In the previous sections we have mainly studied long experiments with strong on-axis heating, whose sharp crashes are easily detected by different diagnostics. In the following sections we will briefly show the main features of different heating schemes and ECCD experiments conducted in different magnetic configurations. The limited amount of comparable experiments, the short duration and the malfunctioning of some core ECE channels strongly hampered the amount of information, which could be extracted. Therefore, the main similarities or discrepancies with respect to the long on-axis ECCD experiments are highlighted.

4.5.1. On- and off-axis comparison

In this section we compare two experiments, plotted in figure 4.14: one with on-axis current (in black) and one with off-axis (in red) current drive. The experiments were conducted in *standard configuration*, with an axis magnetic field of $B_0 = 2.52$.

The regions where the power (and the current drive) is deposited can be seen in figure 3.2. The heating power and the current drive are deposited within $r_{\text{eff}}/a < 0.2$ for the on-axis deposition and between $0.2 < r_{\text{eff}}/a < 0.5$ for the off-axis deposition. The plasma energy in the two experiments is comparable as well as the density. A big difference is represented by the central T_e, which is lower in the off-axis experiment due to the off-axis

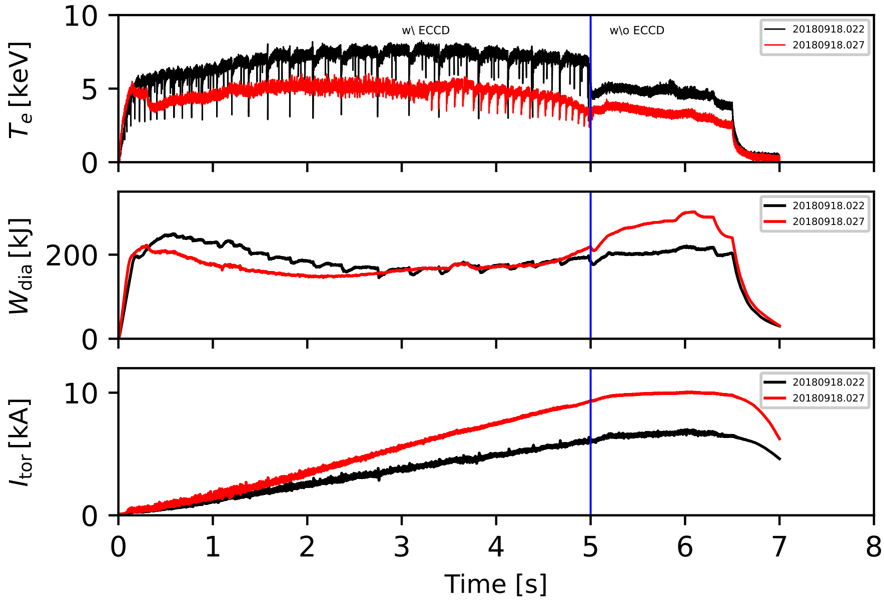

Figure 4.14.: Comparison between *20180918.022* (black, on-axis ECCD),*20180918.027* (red, off-axis ECCD). The T_e timetraces from a core ECE channel, the stored plasma energy and the toroidal current are plotted, respectively. The blue line indicates the moment in which no more net ECCD is driven.

heating itself. At the beginning of each experiment, the ERCH beams were obliquely injected, in order to the generate ECCD. At $t = 5\,\mathrm{s}$, the gyrotrons providing the current drive were turned off. The plasma heating was then taken over by a couple of ERCH beams which reciprocally compensated the generated ECCD and therefore no net current was driven. It is important to note that, as soon as no net current is generated by the ECRH itself, no more crashes are detected. This is an additional confirmation that a localised current is necessary as crash trigger.

The effects of the different heating schemes are visible, even if a proper study of the crash pattern evolution was not possible. The on-axis ECCD experiment has a crash pattern, which is very similar to the one analysed at the beginning of the chapter. In fact, type-A crashes and type-B crashes were detected. The crash pattern is more complicated in the off-axis ECCD

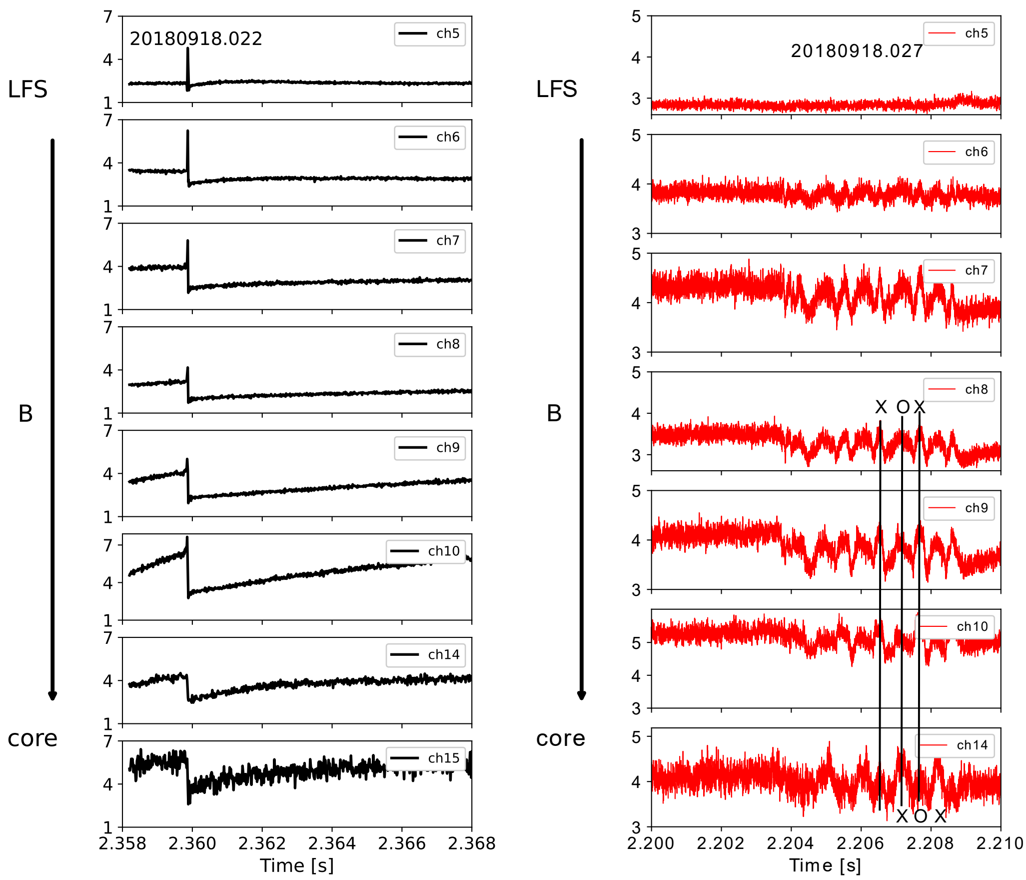

(a) (b)

Figure 4.15.: Comparison of different ECE channels for a type-A crash (black timetraces, *20180918.022*) and a crash with strong oscillations (red timetraces, *20180918.027*). In the latter, the O-point and the X-point of a hot magnetic island can be recognised. Top plots refer to LFS channels, while the bottom refers to a core-HFS channel.

experiment. Since no on-axis heating is present, the T_e profile is different and broader than in the on-axis experiment. A less peaked T_e profile results in turn in a weaker ΔT_e. For the first three seconds, the crashes appear relatively different with respect to those analysed before. An example is shown in figure 4.15b, where the time traces of one HFS channel (ch 14) and other LFS channels are plotted. The crash itself is composed of strong

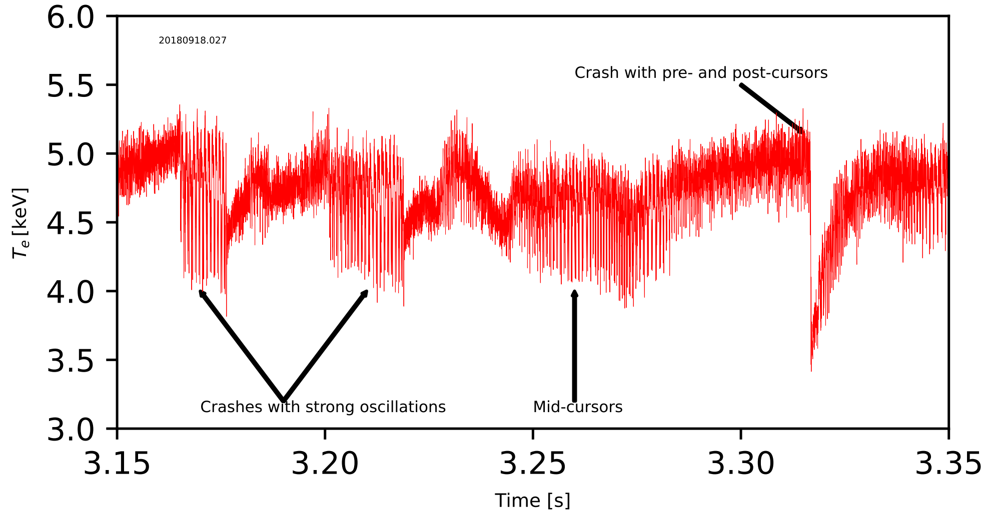

Figure 4.16.: Crash activity in *20180918.022*. Crashes with different precursor types are shown.

T_e oscillations (from $t = 2.204\,\mathrm{s}$ to $t = 2.208\,\mathrm{s}$). The oscillations have the same amplitude of the crash itself, that can be seen at about $t = 2.209\,\mathrm{s}$. The shape of the oscillations have the typical features of a *hot magnetic island* in which T_e within the island is not flat, but presents a maximum due to the localised heating within the island itself. Let us consider channel 8 and 14 of the ECE (figure 4.15b). The two temperature peaks are usually associated with the X-point of the magnetic island, while the hump in between describes a region of the island close to the O-point where the ECRH depositon occurs. The comparison with the HFS channel 14 shows that the X-point detected in one channel corresponds to the O-point in other channel, thus indicating the island has odd poloidal number. No x-ray tomography reconstruction was available. In figure 4.16 several types of T_e oscillations are visible. The crashes at about $t = 3.17\,\mathrm{s}$ and $t = 3.22\,\mathrm{s}$ are similar to the one presented in 4.15b, where oscillations of the order of magnitude of the crash are observed. The oscillations at $t = 3.27\,\mathrm{s}$ are not followed by a temperature drop. These oscillations were observed in other devices [99, 100] and are known as *midcursors* or *compound crashes*. Finally, at $t = 3.2\,\mathrm{s}$ the T_e drop becomes sharper and more similar to the one plotted in figure 4.15a. However, it is preceded by long lasting precursors and postcursors are often observed, which are related to incomplete magnetic reconnection. The presence of mid- and post-cursors suggests a $\iota = 1$ flux surface remains after the temperature crash. A possible explanation for the different pattern of the mode activity preceding the crashes in figure 4.15b could be caused by the position of the ECRH absorption. As we have shown, the position of the resonance shifts outwards as I_{tor} develops. Therefore, the shift of the resonance position with respect to the deposition position could be responsible for the different crash and precursor patterns.

4.5.2. Counter-ECCD

Experiment *20171206.036* was conducted with the same ECCD profile and magnetic configuration as *20171206.025*, but with counter-current, i.e. the current was driven in such a way that the rotational transform is decreased. As a result, τ_{crash} becomes very large and only two crashes in a 25 s long experiment are detected. However, strong T_e oscillations are present for the whole plasma discharge (black time traces in figure 4.17a). The dominant harmonic component has a frequency of 5.8 kHz and the central HFS channels show a strong activity of several harmonics. In figure 4.17b the two dominants Fourier components and the relative phases are plotted respectively in the second and in the fourth panel. The red points indicate the dominant harmonic data (5.8 kHz), while the black points are related to the second harmonic. The reference channel is channel 8 (in blue) at the LFS. The HFS channels with the strongest first harmonic δT_e component are in phase with respect to the reference channel and therefore the perturbation seems to be dominated by an even poloidal number. Two phase jumps, along with strong changes of ξ (third panel) can be seen at about $r/a \approx \pm 0.35$, indicating the non-ideal nature of this mode. Regarding the second harmonic (red) up to three local maxima are identified in proximity of the centre and the phase relation is not clear, since most of the external channels have a negligible component. The rotational transform profile during a counter-ECCD experiment crosses several low rationals $(1/2, 2/3, 3/4, ...)$ (see figure 3.6) in a narrow region and the interaction between them might explain the presence of different modes in the proximity of the axis.

An interesting observation is that oscillations in Mirnov coils (blue timetrace in 4.17a) are found to have the dominant frequency (5.8 kHz) as those

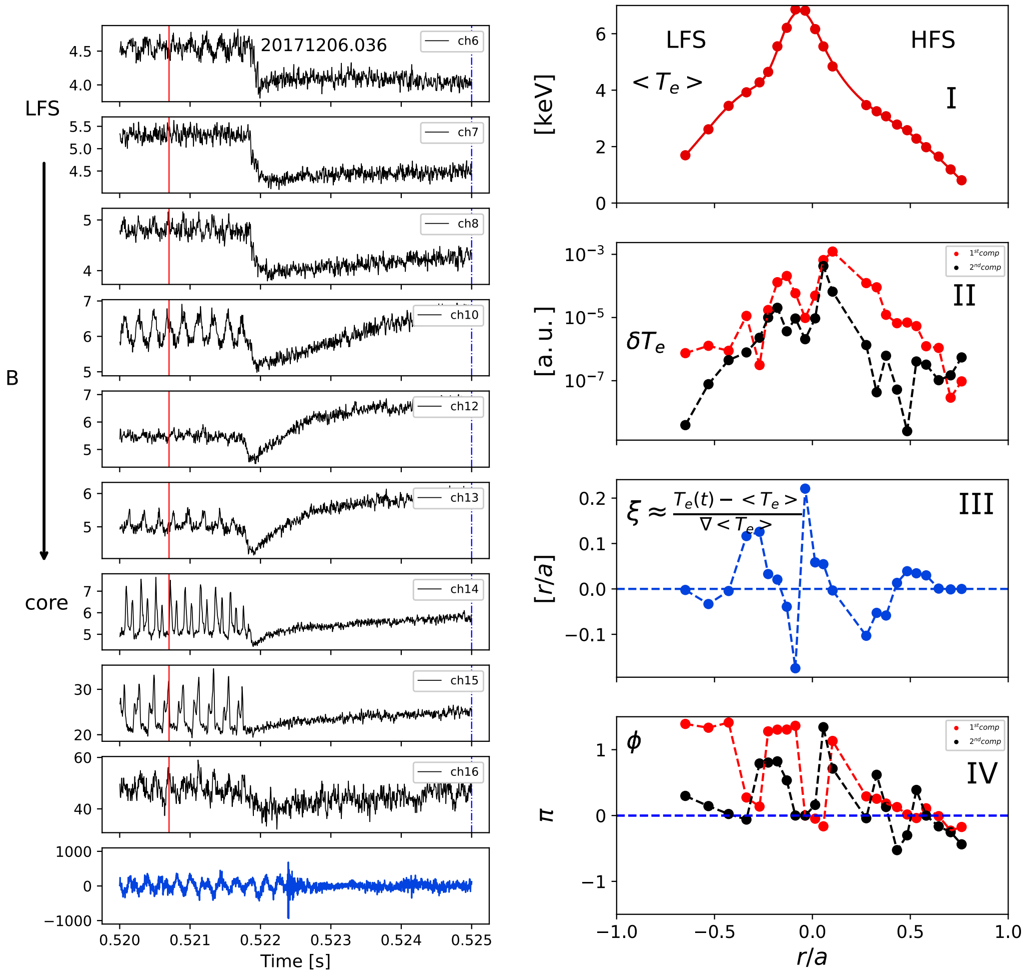

(a) **(b)**

Figure 4.17.: a) different ECE timetraces for *20171206.036* are plotted in black and a Mirnov coil timetrace is plotted in blue. b) The smoothed pre-crash $\langle T_e \rangle$ profile ($t = 0.525\,\mathrm{s}$, blue vertical line), the first and the second Fourier components, the displacement ξ and the preursor phases are plotted.

.

found in the ECE data. The poloidal mode analysis is performed using the Stochastic System Identification (SSI) algorithm [101, 84] and the results are plotted in figure 4.18. A dominant $|m| = 2$ component is found and it consistent with the crossing of a $\iota\!\!\!-\, = n/m = 1/2$ rational surface. No toroidal mode number analysis was possible.

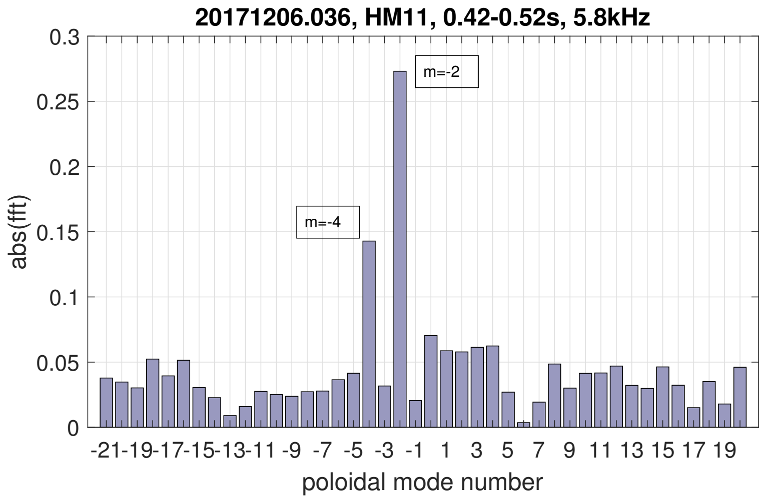

Figure 4.18.: Poloidal mode number analysis of the MHD activity detected in *20171206.036* by means of the Mirnov coils. A dominant $|m| = 2$ poloidal mode number is found.

The absence of periodic crashes can be used to estimate whether the crash activity hampers the development of I_{tor}. We compared three experiments with the same heating power: *20171206.017* (no ECCD), *20171206.028* (co-ECCD) and *20171206.0236* (counter-ECCD). The current deposition profile of the last two mentioned experiments is the same, the only exception being the sign of the current. Experiment *20171206.028* terminated prematurely (see chapter 5) and therefore we can only compare the current developed within the first 12 s. A graphical comparison is provided in figure 4.19. Remembering that $I_{\mathrm{tor}} = I_{\mathrm{ECCD}} + I_{\mathrm{BS}}$ and assuming I_{BS} be the same in the three experiments, we can estimate the ECCD contribution. The subtraction yields $I_{\mathrm{co-ECCD}} \approx -10\,\mathrm{kA}$ and $I_{\mathrm{counter-ECCD}} \approx +9\,\mathrm{kA}$. Therefore, the comparison of this experiments does not show a decrease in I_{tor} for the co-ECCD case, in which strong temperature crash are observed. A better comparison should be performed using experiments in which the current has reached a stationary value.

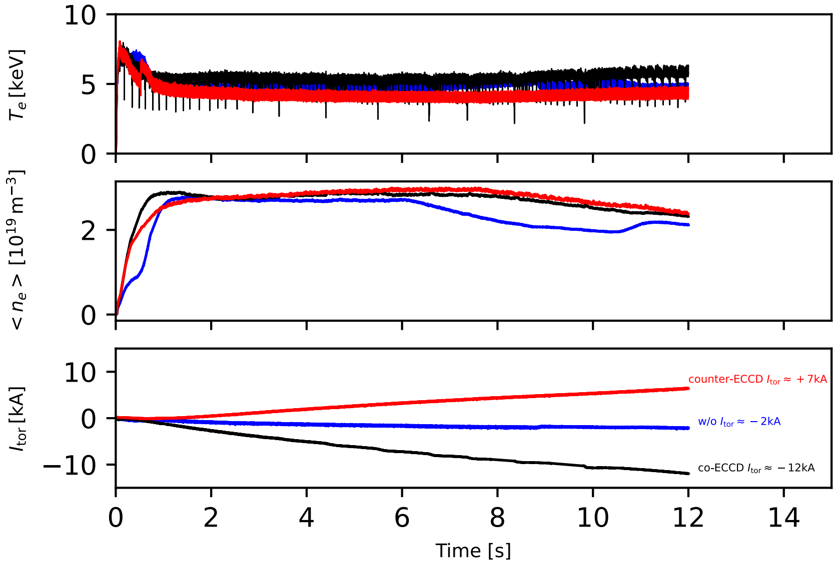

Figure 4.19.: Comparison between the toroidal current development with co-ECCD (black), counter-ECCD (red) and without ECCD (blue). The plasma parameters (first and second panels) are comparable, therefore the blue plot yields a good estimation of the bootstrap current.

4.6. High-iota magnetic configuration

ECCD experiments in the so-called *high-iota configuration* were performed. The rotational transform at the magnetic axis is about $\bar{\iota}_0 \approx 1.04$, therefore counter-ECCD was used to cross $\bar{\iota} = 1$. Experiments confirmed that sawtooth-like crashes are observed in such *high-iota* plasmas. Examples of time traces during on-axis ECCD are plotted in figure 4.20a. The crashes have the same characteristics of a type-A crash. In fact, precursor oscillations with an odd poloidal number are often observed, as well as fast core displacements. The analysis of the relative phase between precursors is plotted in 4.20b. Several channels on both sides are removed due to a malfunctioning. Due to the low number of channels showing precursors, it is not possible to assess the presence of magnetic islands and therefore the nature of the instability. The magnetic shear is considered an important element in the stability analysis [30]. Approaching a resonance from *above* means the

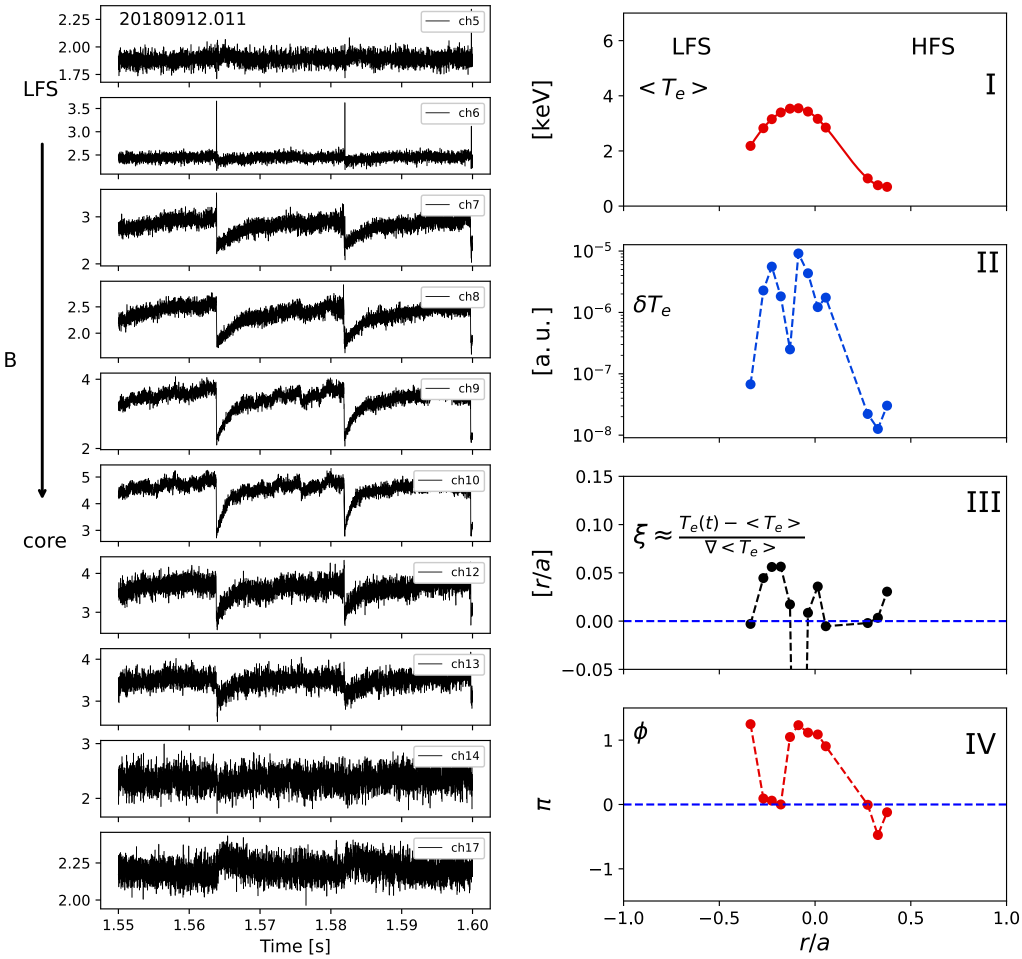

(a) **(b)**

Figure 4.20.: a) in black: different ECE timetraces for *20180912.011*. b) The smoothed T_e profile at the equilibrium ($t = 0.525\,\mathrm{s}$) (I), the dominant Fourier components (II), the displacement ξ and the precursor phases. Several channels were excluded from the Fourier analysis.

.

shear has a sign opposite to the sign which is assumed when approaching it from below. Although the main features of type-A crashes are present, the *high-iota* experiments were generally too short to study the evolution of the crash parameters as a function of the toroidal current. Additionally, the influence of the magnetic shear on the stability of the sawtooth crashes would require a measurement of the rotational transform during the ECCD experiments. Such a measurement is currently not available at W7-X.

4.7. Conclusion

In this chapter we presented the analysis and the characterisation of sawtooth crashes with different magnetic configurations and heating schemes which were observed during ECCD experiments at the W7-X stellarator. The strongest focus is on experiments with on-axis co-ECCD and the *standard configuration*. Several experiments are characterised by a large duration of the plasma discharge (up to 25 s), which allowed us to study the sawtooth crashes at different values of I_{tor}. The experiments are characterised by two different crash types. The crashes can be classified by means of a clusterisation algorithm, such as DBSCAN and which was able to recognise two crash clusters. Type-A crashes are characterised by a large amplitude (up to $60 - 65\,\%$). Short-lived sinusoidal ($f \sim 2 - 6\,\mathrm{kHz}$) precursors are often observed. Even more important is the presence of a strong core displacement which precedes the crash itself. During this process, the plasma core is displaced in about $100 - 200\,\mu\mathrm{s}$ and the core expulsion occurs in $20 - 100\,\mu\mathrm{s}$. The core displacement shows a typical $n = 1$ structure. The relative direction of the core displacement in the ECE and XMCTS planes does not contradict a $m = 1$ structure.

The nature of the mode was investigated by studying the $\xi(r)$ profile and the relative phase ϕ between signals. In most cases, the precursor oscillations were too weak to show the presence of magnetic islands. However, such an analysis was possible in cases of relatively strong precursors, where the change of sign of $\xi(r)$ was accompanied by a phase jump of 180°, thus indicating the presence of a magnetic island.

The crash position and amplitude strongly depends on the toroidal current enclosed in the volume of radius r_{inv}. The toroidal current develops on the timescale of the L/R time, which is on the order of tens of seconds at W7-X. As the current within r_{inv} develops, the $r_{\iota=1}$ shifts outwards, the affected volume becomes larger and the crash stronger. The estimated $r_{\iota=1}$ and the measured r_{inv} do not exactly match. However, they both evolve as a function of r_{inv} with a similar trend.

Type-B crashes were more difficult to analyse. The smaller amplitude and the narrower region of the plasma they affect made them hardly detectable by the x-ray cameras and a proper tomographic inversion was not possible. No precursors were detected by the ECE. Therefore it is not possible to assess any information about their mode number. A possible explanation for the existence of two types of crashes consists in assuming the rotational transform crosses unity twice. Another possibility is that the type-B crashes are triggered by a perturbation with different mode numbers.

A comparison between on-axis and off-axis heating was possible for selected experiments. The main properties of the crashes, such as the crash time and the mode numbers, are consistent with on-axis-induced crashes. A big difference consists in the presence of large precursors and the lack of smaller crashes, such as type-B crashes. The presence of mid-cursors and post-cursors was detected. They are related to the presence of an $\iota\!\!\!- = 1$ surface existing between and after the crashes and the latter are also an indication for incomplete magnetic reconnection.

The island dynamics seems to be strongly influenced by the heating schemes. *Hot island* signatures are in fact identified during off-axis ECCD experiments, in which long oscillations ($> 1\,\mathrm{ms}$) are detected before the T_e crash. The precursor pattern changes during the plasma discharge as it was shown in figure 4.16. The reason is not completely clear and would also require experiments to be conducted at higher densities, in order to have clearer x-ray signals, which could be crucial in better identifying these modes.

No qualitative differences were found between on-axis co-ECCD experiments in *standard configuration* and counter-ECCD in *high-iota configuration*. In both cases an odd poloidal number was found, consistent with the $\iota\!\!\!- = 1$ crossing.

Temperature crashes, although rare, were found in counter-ECCD experiments in the *standard configuration*. The mode seems to be dominated by a perturbation with an even poloidal number, consistent with a crossing of $\iota\!\!\!- = 1/2$ or $3/4$. This hypothesis is supported by poloidal mode number analysis by means of a poloidal Mirnov coil array. A dominant $|m| = 2$ mode number was detected.

A comprehensive theory of sawtooth crashes for W7-X is not completed and several works have recently been published. One work was conducted by using the linear resistive code CASTOR3D [96]. The main findings of this work show that, if $\iota = 1$ is crossed twice $(m, n) = (4, 4)$ double tearing modes (DTM) are formed coupling to $(m, n) = (1, 1)$ non-ideal kink. Another work studied non-linearly the problem in a 1-D cylindrical geometry [97]. An important result is that, if the two $\iota = 1$ are well separated, the $(m, n) = (4, 4)$, DTM couples with a $(m, n) = (1, 1)$ resistive internal kink mode, which becomes dominant in the non-linear phase. The phenomenon obtained in this simulation describes very well the main experimental findings of the type-A crash. However, no experimental indications for DTMs are present. A second crash type was found for a small $\iota = 1$ surface separation, which, however, does not reproduce the main features of a type-B crash we described in this work.

An additional work ([93]) suggests that the ECCD, by changing the rotational transform profile, moves W7-X closer to the ideal marginal stability,therefore becomes susceptible to non-ideal instabilities. In particular, for kinetic effects the instability threshold can be below the ideal one.

Chapter 5.

Effects on plasma performances [1]

In chapter 4 we discussed and presented the main results about ECCD-induced temperature crashes. In this chapter we focus and expand the analysis of experiments in which plasma performance is affected by the temperature crashes. It is empirically observed that large crashes at relatively high I_{tor} can trigger an n_e increase, which in most cases leads to the abrupt deterioration of the plasma stored energy and even to the premature end of the experiment.

A similar event chain was detected in all the experiments, in which a fast and premature termination of the plasma discharge has occurred (presented in section 5.1). A remarkable experiment in which the stored energy did not deteriorate but increased after a series of crashes is presented in section 5.2. We discuss the role of the toroidal current on the density increase in section 5.3. Finally we discuss the main differences with respect to tokamak disruptions in the concluding section (5.4).

5.1. Chain of events

The number of experiments, in which a strong degradation or even a premature plasma termination is observed is very limited, therefore we lack of a proper statistics. However, these experiments are characterised by a similar event chain and a remarkable example (experiment *20171206.028*) is displayed in figure 5.1. We can divide the plasma termination event into five phases. The first phase is represented by a strong crash, with an inversion radius $r_{\text{inv}} \approx 0.5\,a$ at $t = 13.525\,\text{s}$. This crash has the typical

[1] Part of this chapter was published in M. Zanini *et al* 2021, *Nuclear Fusion*, **60** 116053

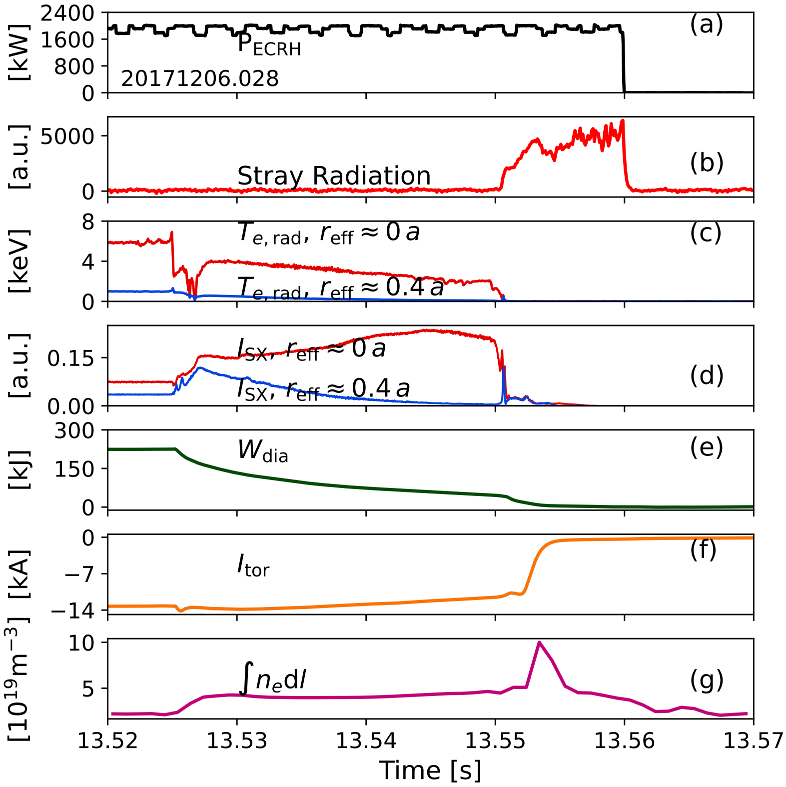

Figure 5.1.: Plasma parameters for *20171206.028*, between $t = 13.52\,\mathrm{s}$ and $t = 13.57\,\mathrm{s}$. A strong temperature crash is detected at $t \approx 13.525\,\mathrm{s}$ (panel (c)) and is followed by an increase in n_e (panel (g)).

features of a type-A crash, such as fast displacement of the plasma core and crash time of about 50 µs. A strong temperature increase, caused by the expulsion of the hot core, is detected by ECE HFS channels in the instants after the crash (see also the T_e profile in red in figure 5.2b). The second phase is characterised by an increase in the electron density, as shown in figure 5.1 (g). An additional indirect measurement of the density increase is given by the x-ray cameras. In figure 5.1 (panel (d)) the timetraces of a core ($r \approx 0a$) and a mid-plasma ($r \approx 0.4a$) x-ray line of sights (LOS) are plotted for the whole process and a zoom is depicted in figure 5.2a (b). The x-ray camera detects an increase in signal for both LOS and a strong peak

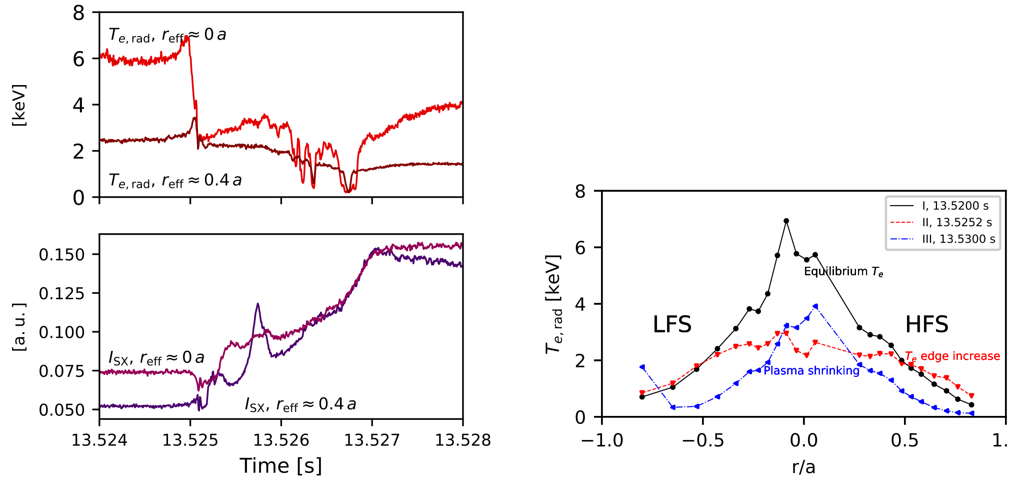

(a) **(b)**

Figure 5.2.: Top plot a): Timetraces of two core ECE channels. The T_e crash happens at $t = 13.5252\,\mathrm{s}$. The decay at $t = 13.526\,\mathrm{s}$ might be artefact. Bottom plot b): Core (light purple) and mid-plasma (dark purple) x-ray diodes. (b): T_e profiles measured by ECE at different timesteps. In black before the crash, in red right after the crash and in blue during the energy dissipation phase.

can be seen by the mid-plasma LOS at $t = 13.526\,\mathrm{s}$. The x-ray radiation intensity I_{SX} is proportional to $T_e^{1/2} n_e^2 Z_{\mathrm{eff}}$ and therefore the I_{SX} increase has to be caused by an increase in n_e and/or Z_{eff}. The additional drop in ECE signals (figure 5.2a (a)) at $t = 13.526\,\mathrm{s}$ does not seem to be a real temperature drop; instead it seems to be caused by a temporary cut-off of the X-2 emission detected by the ECE radiometer. The T_e profiles detected by the ECE for three selected instants are shown in figure 5.2b. The black solid line represents the T_e before the crash. The red dashed line depicts T_e after the crash, with a strong core temperature decrease ($\Delta T_e \approx 65\,\%$). A temporary T_e increase can be seen at the plasma edge. The blue dotted line represents T_e after the density increase. The T_e profile has peaked again, however the temperature from the edge region to the mid-plasma region ($0.5 < |r/a| < 1$) shows a strong decrease with respect to the other two profiles and is generally below $1\,\mathrm{keV}$, which suggests the plasma cooling down starts from the edge.

From the tomographic reconstruction of the soft x-ray emission, regions of stronger signal increase in the poloidal plane of the viewing diagnostic can be identified. Tomograms are plotted in figure 5.3a. The first tomogram represents the emissivity E_{SX} before the temperature crash, while the others display E_{SX} at different instants afterwards. Strong deviations from the pre-crash emissivity E_{SX} are visible, especially in (VI - IX) tomograms. In these tomograms a signal as strong as the one of the core is detected in the outboard side of the plasma. To highlight the interaction region, the relative change of the emissivity was taken into account and plotted in figure 5.3b. From the emissivity $E_{\mathrm{SX}}(t)$ of each point a reference distribution is subtracted, representing the time averaged emissivity in a stationary phase $\langle E_{\mathrm{SX}} \rangle$ before the sawtooth crash. The relative emissivity ΔE_{SX} is calculated as:

$$\Delta E_{\mathrm{SX}}(t) = \frac{E_{\mathrm{SX}}(t) - \langle E_{\mathrm{SX}} \rangle}{\langle E_{\mathrm{SX}} \rangle}. \tag{5.1}$$

In this picture, the strong increase in signal, propagating from the edge, is confirmed. The emissivity peak is initially located in the outboard portion of the plasma and then spreads to the whole plasma edge and eventually increases in the centre. The third phase is characterised by the plasma cooling down. During this phase, the energy decays up to 10 times faster than in a regular experiment termination. Both ECE and x-ray tomography confirm that during the plasma cooling down phase the plasma centre does not move. The plasma cooling starts from the edge and moves towards the core, as the plasma volume shrinks. The strong radiation is the main source of the plasma energy loss, yielding an (almost) isotropic energy release. Thermographic measurements of the divertor do not detect any additional local heating, with the exception of a temperature spike corresponding to the sawtooth crash (which is consistent with other experiments in which no energy degradation is detected) and no direct interaction between the plasma core and the device itself is detected. The third phase is characterised by the dissipation of I_{tor}. The shrinking of the plasma volume and the temperature drop cause an increase in the plasma resistance resistance R. The $\tau = L/R$ term, which is present in equation (1.35) is strongly decreased, thus accelerating the current I_{tor} dissipation. A possible concern for the device integrity is the threat that counter current induced in the plasma facing components and the plasma vessel by the fast decay of I_{tor} can generate strong electromagnetic forces and damage the components. However, no device damages was detected so far.

Finally, the last phase is characterised by an increase in the stray radiation (figure 5.1), representing the unabsorbed ECR power, caused by a poor coupling of the ECRH to the electrons. Triggered by the increase in stray radiation, the interlock system stops the ECRH ($t = 13.56\,\text{s}$). Another remarkable experiment is *20171206.030*, in which the same chain of events is detected. Since the ECRH is not stopped by the interlock system, the plasma is able to recover. In fact, is possible to notice that from $t = 18\,\text{s}$, all plasma parameters start to recover. The recovery is slower than a normal plasma discharge start up (tens of milliseconds), however after about 2 s the stored energy and T_e display similar values to those before the crash.

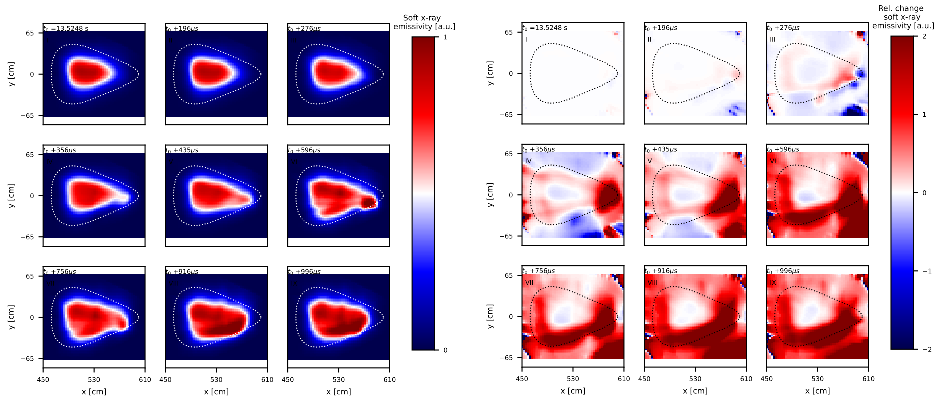

(a) **(b)**

Figure 5.3.: (a): Time series of tomograms for *20171206.028*, between $t = 13.5248\,\text{s}$ and $t = 13.5258\,\text{s}$, showing a poloidal cross-section of the W7-X plasma. The dashed line indicates the last close flux surface. (b): relative change of the emissivity with respect to the first tomogram (equation 5.1). The core expulsion happens in the second and third tomograms. The other tomograms show an increase in x-ray emissivity.

.

The T_e decay in *20171206.030* is slow enough ($5 - 10$ times slower than in figure 5.4) so that the dynamics of the impurity emission lines could be studied by means of the High Efficiency XUV Overview Spectrometer (HEXOS). Clear conclusions regarding the impurity dynamics and effects are not possible since several parameters such as n_e, T_e, r_{eff} are changing at

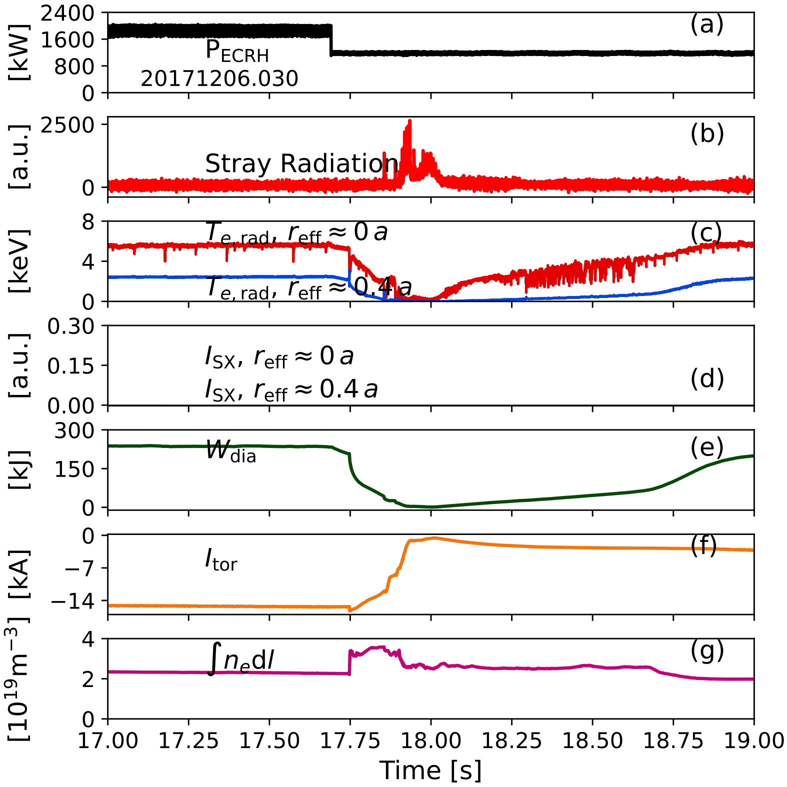

Figure 5.4.: Plasma parameters for *20171206.030*, between $t = 17\,\mathrm{s}$ and $t = 19\,\mathrm{s}$. A strong temperature crash occurs at $t \approx 17.75\,\mathrm{s}$, followed by an increase in density (panel (g)) and a drop of the stored energy (panel (e)). The plasma starts to slowly recover at $t \approx 18\,\mathrm{s}$.

the same time. We therefore qualitatively compare the results with another experiment (*20171207.026*), in which a sudden drop of temperature but no density increase are detected. The temperature drop in *20171207.026* is not related to ECCD experiments. The comparison can be seen in figure 5.5. The x-axis represents $t - t_{\mathrm{ref}}$, where t_{ref} is a reference timestep shortly before the T_e decrease. The y-axis represents the signal renormalised to their average value within the first 50 ms. The direct comparison between the signal increases for the two experiments shows that the H- and He-like carbon emissions are similar in the two experiments. The other emission lines show differences, since the relative emission increase detected in

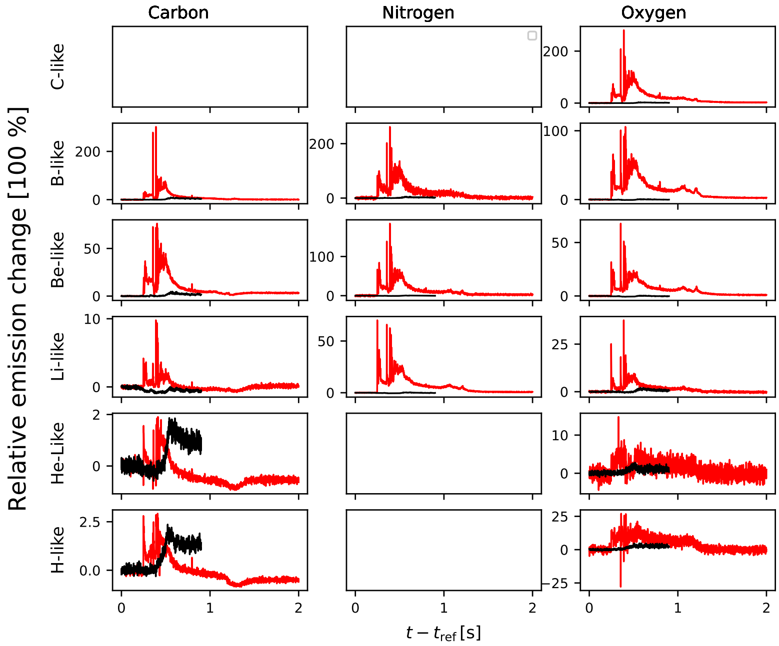

Figure 5.5.: Impurity emission detected by HEXOS. *20171206.030* in red and a reference experiment *20171207.026* in black. The x-axis represents the time from which the temperature drop is detected (t_{ref}).

20171206.030 is orders of magnitude stronger than the emission increase in *20171207.026*. Considering *20171206.030*, a massive radiation increase is detected at $t - t_{\mathrm{ref}} = 0.3\,\mathrm{s}$. The increase is up to 30 times for selected, non saturating oxygen lines (third column). A massive increase in nitrogen (70 times) and carbon (8 times for selected lines) is detected as well. Moreover, chlorine and fluorine emission lines, which were not present before the crash, are detected. Although it is not possible to reconstruct the dynamics of the process, the following is suggested. First of all, the temperature decrease alone, as detected in *20171207.026*, cannot explain the *20171206.030* data. The strong signal increase for the three elements is probably caused by an influx of impurities. Moreover, comparing the inner lines (He- and H-like) of carbon and oxygen and we can observe an increase of up to $2-4$ times for the first element and $5-15$ times for the second. This is an additional indication for a strong oxygen influx in the plasma.

The presence of impurities following the crash is consistent with the x-ray signal increase detected in 5.1 and explains the fast energy decay, which is found to be 10 times faster than a regular experiment termination.

5.2. Sawtooth crash-induced fuelling

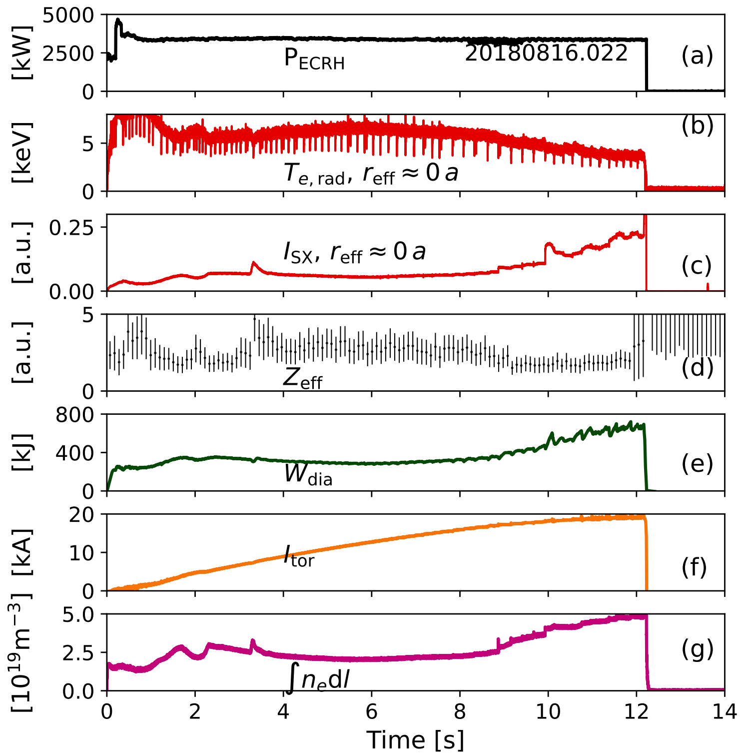

Figure 5.6.: Overview of the main plasma parameters of *20180816.022*. From $t \approx 8\,\mathrm{s}$ a stepwise increase in density is detected.

.

The previous examples show that the plasma can be lost by a fast increase in n_e and/or impurities, following a sawtooth crash. However, in this section we report on one case where the sawtooth activity induced a density increase in the plasma, without leading to a premature termination of the experiment (figure 5.6). The experiment is characterised, with respect to the other

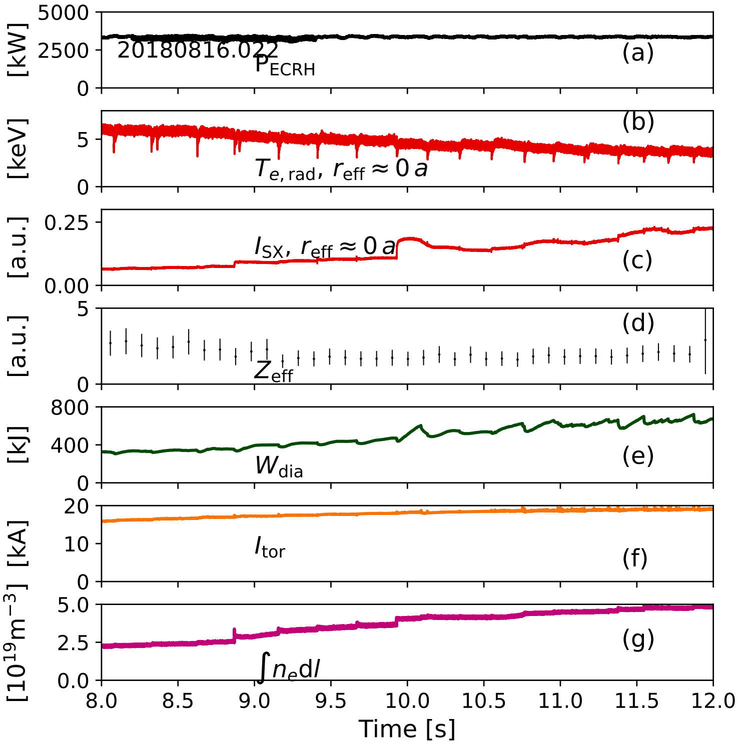

Figure 5.7.: a): Zoom of the main plasma parameters of *20180816.022* between 8 s and 12 s. Almost every sawtooth is associated with a density increase.

.

experiments presented before, by more heating power and a broader current drive profile. At the beginning of the experiment strong differences with respect to the experiments analysed in Chapter 4 are not observed. Both type-A and B crashes are present and the crash sizes increase. In the second part of the experiment, depicted in figures 5.6 and 5.7, stepwise density increases can be seen with every sawtooth crash on the interferometer and the x-ray camera. The crash parameters ($\Delta T_e \approx 65\,\%$ and $r_{\mathrm{inv}} \approx 0.5\,a$) are comparable with those of the sawtooth crashes which are detected before a fast terminating event.

We can only speculate about the factors which lead to the differences between *20180816.022* and the experiments analysed at the beginning of this chapter (*20171206.028* and *20171206.030*). The first difference is the higher heating power used in *20180816.022*, which determines the maximum achievable density [102]. Boronisation can also affect the maximum achievable density by reducing the plasma impurity content. This last aspect was investigated in more details. The first indication is given by the Z_{eff} trend. At about (from about $t = 3\,\mathrm{s}$) a strong increase in Z_{eff}, caused by a probe entering the plasma, is visible. The Z_{eff} value remains constant until about $t = 8.8\,\mathrm{s}$, when the density starts to increase. During this phase of the experiments Z_{eff} drops from about 2.5 to 1.6. This observation indicates that the new particles, which are now fuelling the plasma, are mainly hydrogen. If this were not the case, the Z_{eff} decrease, along with a n_e increase, could not be explained. A more detailed analysis regarding impurity line radiation was attempted with the HEXOS diagnostic. However, it was not possible to disentangle the T_e and n_e contributions to the line emissions, but, nevertheless, no strong increase in the impurity emission was detected.

5.3. Role of I_{tor}

It was empirically noticed that these few events with a plasma termination occurred at relatively high toroidal current ($> 10\,\mathrm{kA}$). The increase in radiation starting from the edge is a good indication for the interaction of the expelled hot core and the neutrals or impurities located between the very edge of the confinement region and the plasma facing components. It is shown in chapter 4 that I_{tor} can be directly related to the size of the crashes. We consider four different experiments with comparable plasma parameters and heating schemes and verify whether a significant increase in density can be detected after the crashes. The results are displayed in figure 5.8, where $r_{\mathrm{inv,\,hfs}}$ of each crash is plotted against ΔT_e. If no density increase is detected, the points are shown in black and, in red, if a density increase is detected. Only four crashes are related to a density increase. One of them ($\Delta T_e \approx -40\,\%$, $r_{\mathrm{inv}} \approx 0.15$) is related to a crash detected in *20171206.030* ($t = 17.9\,\mathrm{s}$) (figure 5.4) and occurred in a plasma which has already shrunk due to the energy dissipation caused in turn by another sawtooth crash, discussed in figures 5.4 and 5.5. The other three crashes depicted in red are related to large ΔT_e and especially to average $r_{\mathrm{inv}} \approx 0.5a$. This is a very large r_{inv}, as it can be seen that the average inversion radius of

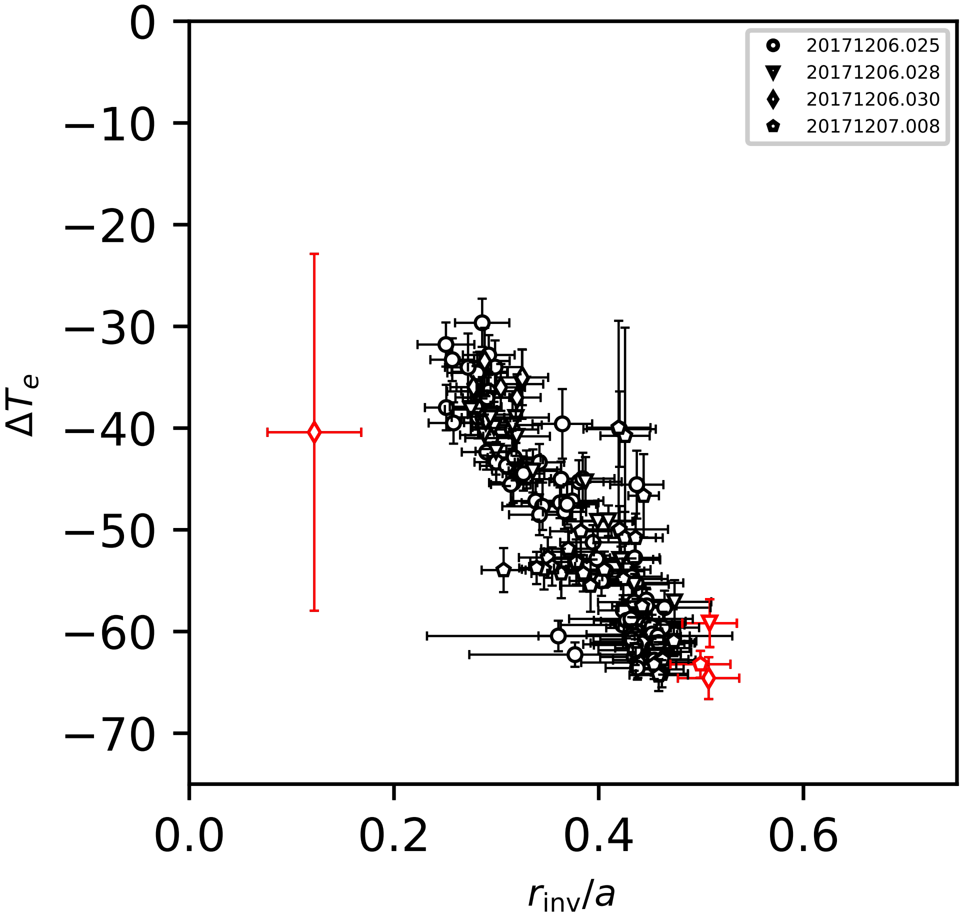

Figure 5.8.: In black: crash parameters of crashes not related to a density increase. In red: crash parameters of crashes were a density increase was detected by the interferometer.

the other crashes is about $r_{\mathrm{inv}^{avg}} \approx 0.38a$. A large crash volume is not only related to a large expelled energy but it also makes easier for the expelled plasma to reach the edge.

5.4. Conclusions

In this chapter we presented a series of experiments where strong density increases were detected after the sawtooth crashes. In one case, after a large sawtooth has taken place, a strong x-ray radiation is detected in the region in which the hot core is expelled. It is assumed the signal be caused by the ionisation of neutrals which, are present at the plasma edge. Analysis of the impurity emission confirms a strong increase in the N and O emission lines. The increased radiation losses cause a cooling down of the plasma that starts from the edge and propagates towards the core as the plasma volume shrinks. The total plasma current remains nearly constant until the plasma temperature is well below 1 keV and is eventually dissipated on a timescale some orders of magnitude faster than a normal experiment ending. The plasma energy is lost mainly through radiation and the plasma core maintains its position throughout the process. We also detected one case, in which the ERCH heating is not turned off and the plasma recovers after a few seconds. This event demonstrates the robustness of W7-X plasmas against terminating events.

In one case it is found that the sawtooth crashes themselves were responsible for stepwise density increases. The process is similar to the case in which the plasma loss occurs, but in this case no impurity increase is detected.

The main difference between the experiments in which the plasma is lost and the one in which the plasma is fuelled by sawteeth consists in a different heating power and in the wall boronisation. The boronisation of the wall reduces the concentration of impurities in the plasma and therefore reduces radiation losses. An higher heating power allows to sustain a plasma at higher densities, by keeping a positive balance between the energy transferred to the plasma and the energy losses.

In summary, we propose the following mechanism. Large crashes are found to trigger a density increase. If the energy balance is negative, i.e. the ECRH power is not sufficient to sustain the radiation losses, the cooling down of the plasma, starting from the edge, occurs and the plasma shrinks. This indicates that the plasma-wall interaction is strongly reduced and the energy release is almost isotropic. Additionally, an higher heating power or an adequate wall conditioning can contribute to avoid such events.

Chapter 6.

Summary and conclusions

In this work we analysed and characterised the main features of the sawtooth crashes observed in W7-X plasmas, during ECCD experiments. The main magnetic field configurations are designed to avoid low order rational values of the rotational transform within the confinement region of the plasma. Localised ECCD can strongly modify the rotational transform producing such low order rationals, which can significantly alter the plasma stability conditions.

In chapter 3 we calculated the ECCD profiles, for typical experiments, using the ray-tracing code TRAVIS and solved the current diffusion equation in simplified geometry. We showed that the rotational transform can be modified by ECCD on time scales which are consistent with the measured times for the temperature crashes to occur.

In chapter 4 we presented the experimental data, focusing our analysis on on-axis ECCD experiments ($t > 10$s, with a crash period of about $\tau_{\text{crash}} \approx 50 - 200$ms) and identified up to two types of crashes. The first type (called type-A) is characterised by large temperature drop (ΔT_e between 30 an 60 %) and large affected volumes, with an inversion radius of $r_{\text{inv}} \approx 0.3\,a - 0.5\,a$. This crashes are occasionally preceded by low frequency precursors. More often, a core displacement is detected before the crash. The displacement has a typical $m = 1$ structure and forms in about 100 µs. The joint analysis of electron cyclotron emission (ECE) and x-ray tomography showed that the mode is consistent with an $(m, n) = (1, 1)$ structure.

The second type of crashes (called type-B) are localised close to the magnetic axis, covering a smaller volume and have smaller amplitudes (ΔT_e between 10,30 %). The analysis of these crashes was performed only with ECE, since their amplitude was generally too small for the soft x-ray diagnostic to detect them. A mode analysis was not possible.

Since a measurement of the current profile was not available, it was not possible to directly measure the positions where low order rationals are crossed. However, since most of the toroidal current is driven within the inversion radius r_{inv}, an estimation of the resonance positions for the type-A crashes was attempted by assuming that the whole plasma current is driven at the magnetic axis. Since the current evolves over time, also the estimated resonance position changes.

The time evolution from the model compares favourably with the measured r_{inv} being almost linear in the final part of the experiment. This indicates that the crash size is directly related to the position where the resonance is triggered, which moves outwards as the toroidal current evolves.

Temperature crashes are detected also for ECCD deposition positions away from the magnetic axis, with two major differences with respect to the (almost) on-axis case: strong precursor activities are detected before the crashes and no type-B crashes were detected. Although it is not possible to properly give an explanation for these differences, it can be speculated that the absence of type-B crashes might be caused by the crossing of different rational values in the proximity of the axis.

During counter-ECCD experiments, temperature crashes were rarely observed. The MHD activity analysis suggests the mode is characterised by an even poloidal number ($m = 2$) and therefore is consistent with a crossing of $\iota = 1/2$.

Finally, experiments with counter-ECCD in the so-called *high iota* magnetic configuration have been analysed. Temperature crashes were detected as well even if the resonance crossing occurs from *above* and therefore with a reversed shear with respect to the *standard configuration* case.

The temperature crashes we observed at W7-X seem to reproduce the main features of the sawtooth crashes which are regularly observed in tokamaks and this offers the possibility to use the extensive work which was carried out in the past to improve the knowledge over the temperature crashes at W7-X. However, differences exist. The main difference is represented by the toroidal current, which is necessary in tokamaks for the plasma confinement. The toroidal current has a broad profile and sawteeth are very common, although externally driven current can be generated to modifiy the rotational transform too, so as to mitigate or suppress them. With respect to this, the sawtooth control is crucial for large devices since the expelled energy and the coupling with other unstable modes can limit the maximum achievable plasma parameters and can also damage the device itself.

Regarding W7-X, the temperature crashes were only detected during ECCD experiments. A conclusive theoretical work regarding the W7-X plasma stability is not yet complete, although the studies performed so far indicate that the strong modifications of the rotational transform caused by a localised current can significantly change the stability condition of the magnetic configuration. This shows that a low shear stellarator is very sensitive to a toroidal current. A crucial question to be answered in the future experiments is whether the bootstrap current in high β plasmas can contribute to destabilise a sawtooth. The understanding of the temperature crash physics would also offer the possibility to control them, such as to remove high-Z impurities from the plasma core.

The effects the temperature crashes have on the removal of high-Z impurities from the plasma core were not yet assessed. This feature is widely used to prevent an high concentration of impurities in tokamaks and could be investigated in W7-X. For this reason, a deeper understanding of the temperature crash physics is crucial in order to control them.

In chapter 5 the impact of strong temperature crashes on the plasma performances was investigated. However, only few experiments were available. The comparison of these experiments suggests that when a strong crash occurs ($r_{\mathrm{inv}} > 0.5/a$), a strong density increase is detected in the plasma. In most cases, this density increase came along with a strong impurity emission increase. Such an increase in the impurity content can be deleterious for the plasma. In one experiment, which was conducted after wall boronisation, a constant plasma fuelling was observed after every crash, without any increase in impurity. This may suggest that, if a proper wall conditioning is conducted, the temperature crash can also have positive effects to the plasma fuelling and terminating events can in principle be avoided by carefully planning the experiments in such a way not to overcome a certain I_{tor} threshold, as I_{tor} itself plays a fundamental role in the crash size.

A crucial question to be answered is whether these events can be related to disruptions in tokamaks. The termination events presented in chapter 5 present some qualitative similarities with respect to tokamak disruptions, i.e. a temperature quench and a current quench phases are detected before the plasma loss. However, the situation for the two configurations is rather different. First of all, in stellarators the toroidal current is not necessary for the plasma confinement. This makes the toroidal currents in tokamaks orders of magnitude higher than the maximum achieved toroidal current at W7-X. Therefore, the $\mathbf{j} \times \mathbf{B}$ forces, induced into a tokamak vessel due to a fast current dissipation, can be orders of magnitude higher than in a stellarator. Additionally, the rotational transform in a stellarator is provided by the external coils. The existence of the flux surfaces does not depend on the toroidal current and we reported on a case in which the plasma recovered after a loss of more than 90 % of the stored energy.

The limited dataset does not allow to have a full comparison with tokamak disruptions. On the other hand, this is also a demonstration that these events do not happen routinely, showing once again the robustness of W7-X against plasma loss events.

Appendix A. Appendix

A.1. Singular value decomposition

The singular value decomposition (SVD) [98] algorithm allows to decompose the experimental signals into spatial and time elements. Data are represented by an $(n \times m)$ matrix $\mathbf{X}$ $(m \leq n)$ and the matrix consists of m_{ij} elements, with $i, ..., n$ time points and $j, ..., m$ spatial points. The SVD algorithm decomposes the matrix $\mathbf{X}$

$$\mathbf{X} = \mathbf{U}^T \mathbf{S} \mathbf{V}, \tag{A.1}$$

where $\mathbf{U}$ and $\mathbf{V}$ are respectively a $(m \times m)$ and $(n \times n)$ unitary matrices and $\mathbf{S}$ is a $(m \times n)$ diagonal matrix, whose eigenvalues s_i are called *singular values*. They are sorted with decreasing relevance for the data, such that $s_1 \geq s_2 \geq ... \geq s_m \geq 0$. The singular values represent the *magnitude* of each component, whose spatial and time components are represented by the columns of the matrices $\mathbf{U}$ and $\mathbf{V}$. The spatial structures of the dataset is represented by the vectors u_k (*topos*) and their corresponding temporal evolution v_k (*chronos*). The filtered signal can be reconstructed by properly selecting the components, such that:

$$\hat{\mathbf{X}} = \sum_{k=l}^{p} u_{ki} s_k v_{kj} \tag{A.2}$$

where the indeces l,p refer to the first and the last element used in the reconstruction. SVD has been successfully used in different fields. For this work it has been used to extract the unperturbed and perturbed components from the total signal. The first singular value is generally referred to the unperturbed component of the signal, while the others represents, in descending order, the strongest perturbations. In this thesis, the SVD analysis was applied to soft x-ray tomography data before the crashes in order to verify whether a dominant component could be found.

A.2. Cluster algorithm

Cluster analysis consists in grouping a set of data with similar characteristics. As a first approach, we analysed experiments with similar plasma parameters (such as P_{ECRH}, W_{dia}, n_e, T_e, etc.) in order to automatise the separation of type-A and -B crashes. The parameters used for the cluster analysis are I_{tor}, $r_{\mathrm{inv,\,hfs}}$, $r_{\mathrm{inv,\,lfs}}$,ΔT_e.

Data were pre-processed using the `scikit-learn` [103] build-in function `RobustScaler`, which rescales the dataset by removing the median and by scaling the data according to the chosen quantile range, which in the cases here presented spans between the first and the third quantile.

Additionally, the principal component analysis (PCA) was performed on the scaled data in order to reduce the dimensionality. Data in figures A.1 and A.2 represent the experimental data plotted in figure 4.4, processed using the PCA. PCA is an orthogonal linear transformation that decomposes a multivariate dataset in a set of orthogonal components. The new components are sorted by their variance. The *first component* is the component with the highest variance, the *second component* has the second-highest variance and so on. For the dataset here analysed the first and the second components provide 99 % of the variance of the data. This made possible to carry out the cluster analysis using two dimensions instead of the original four.

The internal validation of the algorithm was assessed using the *Silhouette score* [104], which is based on two quantities: a and b. a measures the intra-cluster distance, i.e. the average distance of a point with respect to all the other points of the same cluster. b measures the distance between one point of a cluster and all the other points in the clusters it is not part of. Finally, the Silhouette score of each point i is defined as: $s(i) = (b(i) - a(i))/max\{a(i), b(i)\})$. The best value is 1, representing that the clusters are dense and well separated, while the worst value is -1, indicating that different clusters do not differ from each others.

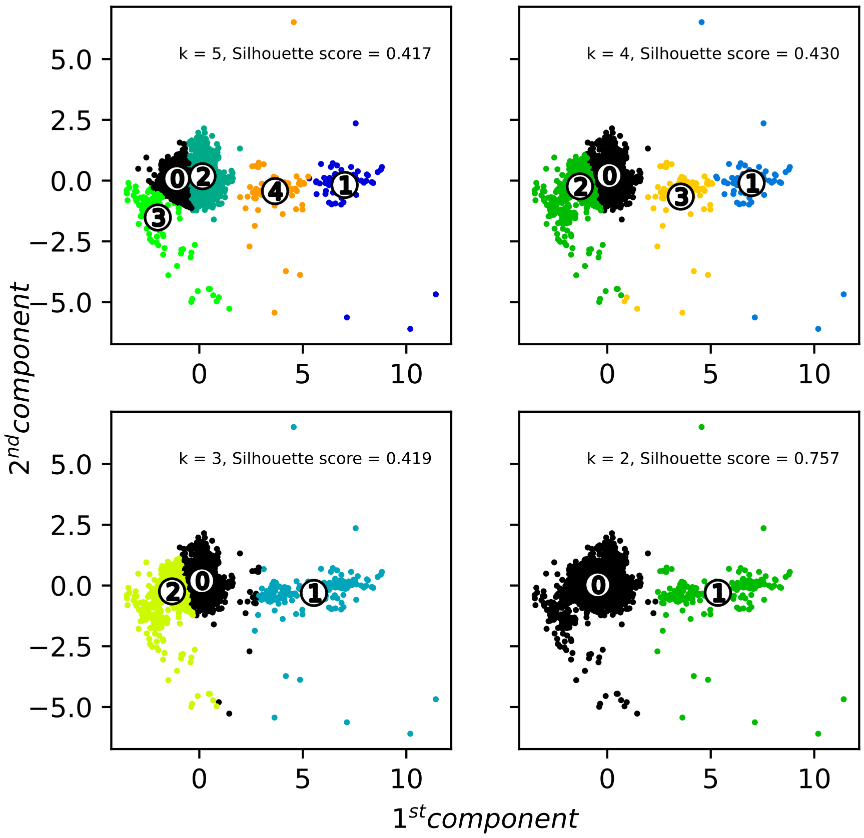

Figure A.1.: k-Means clustering, for different k. The x- and the y-axes represent the first and the second component found by means of the PCA, used to reduce the dimensionality of the dataset.

We tested first the possibility of dividing the dataset into clusters by using the *k-Means* algorithm, which splits the dataset into k different clusters, each described by the mean μ_j (known as *centroid*) of the samples in the cluster. The algorithm starts with the creation of k centroids and iterates the following two steps. The first step consists in assigning each point to the closest centroid, while the second step consists in re-calculating new centroids by taking the mean values of all the sample assigned to previously existing centroids. The process is iterated until the position of the new centroids does not significantly vary with respect to the position of the previous centroids.

We run the algorithm for different k values and compared the Silhouette score (figure A.1). The number of clusters k that maximizes the average Silhouette score is for $k = 2$.

Once we showed the dataset could be divided into clusters, we tested another algorithm, DBSCAN [94]. DBSCAN clusters are defined as regions of high point density separated by low point density regions. In such a way, clusters can assume any shape, in contrast to k-Means which requires the cluster have a convex shape. Additionally, DBSCAN is well suited for handling possible outliers (*noise*).

Each cluster is composed of *core samples* and *non-core samples*. A point is a core sample if it is located within a distance (`eps`) from at least a certain amount of point (`min samples`). Non-core samples are points which are within a distance `eps` from a number of points lower than (`min samples`). If a points is neither a core sample or a non-core samples it is classified as noise. The cluster number is a free parameter and the main parameters to be chosen are the distance `eps` and the minimum amount of points a cluster can be composed of. For the clustering of our dataset we chose `min samples` = 10 and selected the distance `eps` that maximises the Silhouette score.

An example is depicted in figure A.2, where the algorithm is applied to the data using different `eps` values. Every different cluster is plotted with different colours, while outliers are plotted in black. For a small distance (`eps` = 0.27), the algorithm recognises 4 clusters and several points located in between are classified as outliers. The number of clusters decreases as `eps` increases, as well as the number of outliers. Finally, in the bottom right plot, we displayed the results corresponding to the maximum Silhouette (0.729), which corresponds to (`eps` = 0.66). Also for DBSCAN, the Silhouette is maximised if the dataset is divided into two clusters. These two clusters are shown in the original parameter space in figure 4.4.

The clustered data presented in chapter 4 corresponds to bottom right plot of A.2, since DBSCAN revealed to be as effective as k-Means and has the intrinsic advantages of not requiring a predetermined number of clusters, not requiring a convex shape and being capable of removing the outliers.

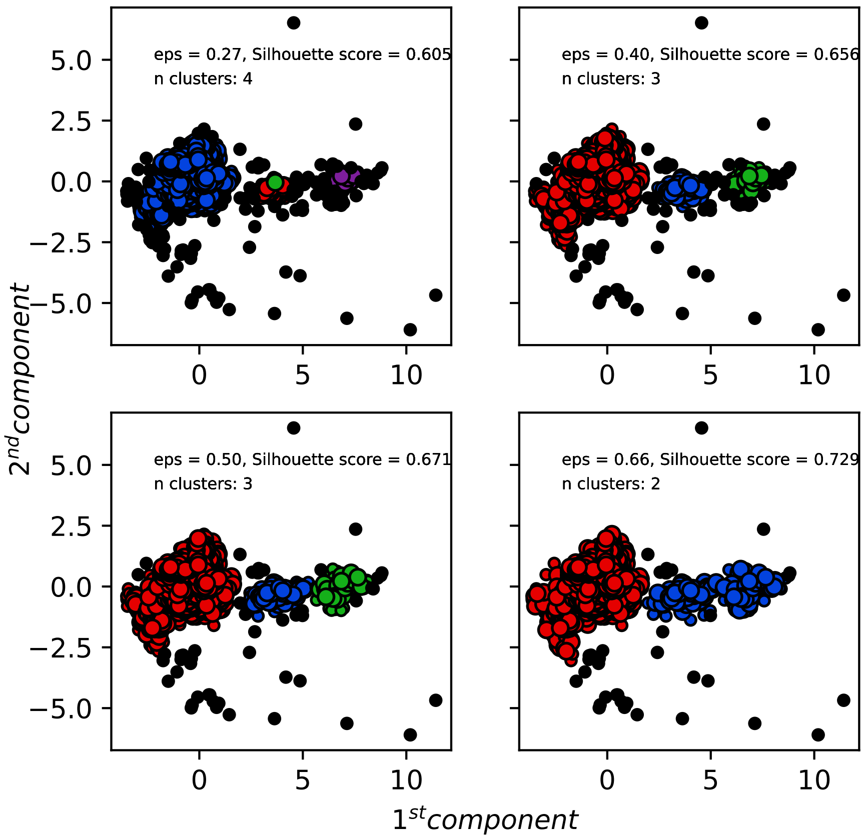

Figure A.2.: DBSCAN clustering, for different `eps`. The bottom left plot refers to the `eps` value that maximise the average Silhouette score. The x- and the y-axes represent the first and the second component found by means of the PCA, used to reduce the dimensionality of the dataset.

Bibliography

[1] K. Kikuchi, M.; Lackner and T. Minh Quang, *Fusion Physics.* International Atomic Energy Agency, 2012.

[2] S. Atzeni and J. Meyer-ter Vehn, *The Physics of Inertial Fusion.* Oxford University Press, 2009.

[3] J. D. Lawson, "Some criteria for a power producing thermonuclear reactor," *Proceedings of the Physical Society. Section B*, vol. 70, pp. 6–10, Jan. 1957.

[4] P. I. Strand and W. A. Houlberg, "Magnetic flux evolution in highly shaped plasmas," *Physics of Plasmas*, vol. 8, pp. 2782–2792, June 2001.

[5] N. J. Fisch, "Theory of current drive in plasmas," *Reviews of Modern Physics*, vol. 59, pp. 175–234, Jan. 1987.

[6] F. L. Hinton and R. D. Hazeltine, "Theory of plasma transport in toroidal confinement systems," *Reviews of Modern Physics*, vol. 48, pp. 239–308, Apr. 1976.

[7] P. Helander and D. Sigmar, *Collisional Transport in Magnetized Plasmas.* Springer Berlin Heidelberg, 2002.

[8] A. Gibson and J. B. Taylor, "Single particle motion in toroidal stellarator fields," *Physics of Fluids*, vol. 10, no. 12, p. 2653, 1967.

[9] H. E. Mynick, "Transport optimization in stellarators," *Physics of Plasmas*, vol. 13, p. 058102, May 2006.

[10] A. H. Boozer, "Physics of magnetically confined plasmas," *Reviews of Modern Physics*, vol. 76, pp. 1071–1141, Jan. 2005.

[11] P. Helander, "Theory of plasma confinement in non-axisymmetric magnetic fields," *Reports on Progress in Physics*, vol. 77, p. 087001, July 2014.

[12] J. P. Freidberg, *Ideal MHD.* Cambridge University Press, 2014.

[13] H. Grad, "Toroidal containment of a plasma," *Physics of Fluids*, vol. 10, no. 1, p. 137, 1967.

[14] H. Zohm, ed., *Magnetohydrodynamic Stability of Tokamaks.* Wiley-VCH Verlag GmbH & Co. KGaA, Dec. 2014.

[15] T. Hender *et al.*, "Chapter 3: MHD stability, operational limits and disruptions," *Nuclear Fusion*, vol. 47, pp. S128–S202, June 2007.

[16] V. Igochine, ed., *Active Control of Magneto-hydrodynamic Instabilities in Hot Plasmas.* Springer Berlin Heidelberg, 2015.

[17] I. B. Bernstein *et al.*, "An energy principle for hydromagnetic stability problems," *Proceedings of the Royal Society of London. Series A. Mathematical and Physical Sciences*, vol. 244, pp. 17–40, Feb. 1958.

[18] J. Wesson, "Hydromagnetic stability of tokamaks," *Nuclear Fusion*, vol. 18, pp. 87–132, Jan. 1978.

[19] Marshall. N. Rosenbluth, R. Y. Dagazian P. H. Rutherford, "Nonlinear properties of the internal m = 1 kink instability in the cylindrical tokamak," *Physics of Fluids*, vol. 16, no. 11, p. 1894, 1973.

[20] P. H. Rutherford, "Nonlinear growth of the tearing mode," *Physics of Fluids*, vol. 16, no. 11, p. 1903, 1973.

[21] Z. Chang *et al.*, "Observation of nonlinear neoclassical pressure-gradient–driven tearing modes in TFTR," *Physical Review Letters*, vol. 74, pp. 4663–4666, June 1995.

[22] S. von Goeler, W. Stodiek, and N. Sauthoff, "Studies of internal disruptions and $m = 1$ oscillations in tokamak discharges with soft x-ray tecniques," *Physical Review Letters*, vol. 33, pp. 1201–1203, Nov. 1974.

[23] J. Wesson and D. J. Campbell, *Tokamaks.* OUP Oxford, 2011.

[24] B. B. Kadomtsev *Fizika Plasmy*, vol. 1, no. 20, pp. 710–715, 1975.

[25] G. Ara *et al.*, "Magnetic reconnection and m = 1 oscillations in current carrying plasmas," *Annals of Physics*, vol. 112, pp. 443–476, June 1978.

[26] M. D. Kruskal and C. R. Oberman, "On the stability of plasma in static equilibrium," *Physics of Fluids*, vol. 1, no. 4, p. 275, 1958.

[27] A. Lichtenberg *et al.*, "The role of stochasticity in sawtooth oscillations," *Nuclear Fusion*, vol. 32, pp. 495–512, Mar. 1992.

[28] V. Igochine *et al.*, "Stochastic sawtooth reconnection in ASDEX Upgrade" *Nuclear Fusion*, vol. 47, pp. 23–32, Dec. 2006.

[29] C. G. Gimblett and R. J. Hastie, "Calculation of the post-crash state and 1 1/2 d simulation of sawtooth cycles," *Plasma Physics and Controlled Fusion*, vol. 36, pp. 1439–1455, Sept. 1994.

[30] F. Porcelli, D. Boucher, and M. N. Rosenbluth, "Model for the sawtooth period and amplitude," *Plasma Physics and Controlled Fusion*, vol. 38, pp. 2163–2186, Dec. 1996.

[31] R. J. Hastie *Astrophysics and Space Science*, vol. 256, no. 1/2, pp. 177–204, 1997.

[32] I. T. Chapman, "Controlling sawtooth oscillations in tokamak plasmas," *Plasma Physics and Controlled Fusion*, vol. 53, p. 013001, Nov. 2010.

[33] T. Nicolas *et al.*, "Impurity behavior during sawtooth activity in tokamak plasmas," *Physics of Plasmas*, vol. 21, p. 012507, Jan. 2014.

[34] A. Gude *et al.*, "Seed island of neoclassical tearing modes at ASDEX Upgrade," *Nuclear Fusion*, vol. 39, pp. 127–131, Jan. 1999.

[35] V. Igochine *et al.*, "Seeding of neoclassical tearing modes by internal crash events in the ASDEX Upgrade and DIII-D tokamaks," *Nuclear Fusion*, vol. 59, p. 066038, May 2019.

[36] Y. Nagayama *et al.*, “Sawtooth oscillation in current-carrying plasma in the large helical device,” *Physical Review Letters*, vol. 90, May 2003.

[37] T. Estrada *et al.*, “Transient behaviour in the plasma core of TJ-II stellarator and its relation with rational surfaces,” *Plasma Physics and Controlled Fusion*, vol. 44, pp. 1615–1624, July 2002.

[38] A. Weller *et al.*, “Survey of magnetohydrodynamic instabilities in the advanced stellarator Wendelstein 7-AS,” *Physics of Plasmas*, vol. 8, pp. 931–956, Mar. 2001.

[39] A. H. Boozer, “Theory of tokamak disruptions,” *Physics of Plasmas*, vol. 19, p. 058101, May 2012.

[40] N. Ohyabu, “Density limit in tokamaks,” *Nuclear Fusion*, vol. 19, pp. 1491–1497, Nov. 1979.

[41] L. Lao and T. Jensen, “Magnetohydrodynamic equilibria of attached plasmas after loss of vertical stability in elongated tokamaks,” *Nuclear Fusion*, vol. 31, pp. 1909–1922, Oct. 1991.

[42] P. Helander *et al.*, “Stellarator and tokamak plasmas: a comparison,” *Plasma Physics and Controlled Fusion*, vol. 54, p. 124009, Nov. 2012.

[43] E. Sallander *et al.*, “Effects of non-vanishing toroidal current densities on stability in the Wendelstein 7-AS stellarator,” *Nuclear Fusion*, vol. 40, pp. 1499–1509, Aug. 2000.

[44] B. Coppi, M. Nassi, and L. E. Sugiyama, “Physics basis for compact ignition experiments,” *Physica Scripta*, vol. 45, pp. 112–132, Feb. 1992.

[45] J. P. Freidberg, “Heating and current drive,” in *Plasma Physics and Fusion Energy*, pp. 534–632, Cambridge University Press.

[46] M. Thumm *et al.*, “High-power gyrotrons for electron cyclotron heating and current drive,” *Nuclear Fusion*, vol. 59, p. 073001, June 2019.

[47] T. H. Stix, *Waves in Plasmas.* AIP-Press, 2009.

[48] V. Erckmann and U. Gasparino, "Electron cyclotron resonance heating and current drive in toroidal fusion plasmas," *Plasma Physics and Controlled Fusion*, vol. 36, pp. 1869–1962, Dec. 1994.

[49] N. J. Fisch and A. H. Boozer, "Creating an asymmetric plasma resistivity with waves," *Physical Review Letters*, vol. 45, pp. 720–722, Sept. 1980.

[50] T. Ohkawa, "Steady-state operation of tokamaks by RF heating general," 1976.

[51] R. Prater, "Heating and current drive by electron cyclotron waves," *Physics of Plasmas*, vol. 11, pp. 2349–2376, May 2004.

[52] J. Stober *et al.*, "Feedback-controlled NTM stabilization on ASDEX upgrade," *EPJ Web of Conferences*, vol. 87, p. 02017, 2015.

[53] M. Romé *et al.*, "Electron cyclotron resonance heating and current drive in the W7-X stellarator," *Plasma Physics and Controlled Fusion*, vol. 40, pp. 511–530, Apr. 1998.

[54] G. Grieger and I. Milch, "Das fusionsexperiment Wendelstein 7-X," *Physik Journal*, vol. 49, pp. 1001–1005, Nov. 1993.

[55] R. Wolf *et al.*, "Major results from the first plasma campaign of the Wendelstein 7-X stellarator," *Nuclear Fusion*, vol. 57, p. 102020, July 2017.

[56] R. Wolf *et al.*, "Performance of Wendelstein 7-X stellarator plasmas during the first divertor operation phase," *Physics of Plasmas*, vol. 26, p. 082504, Aug. 2019.

[57] T. Rummel *et al.*, "The Wendelstein 7-X trim coil system," *IEEE Transactions on Applied Superconductivity*, vol. 24, no. 3, pp. 1–4, 2014.

[58] J. Nührenberg and R. Zille, "Stable stellarators with medium and aspect ratio," *Physics Letters A*, vol. 114, no. 3, pp. 129–132, 1986.

[59] G. Grieger *et al.*, "Physics optimization of stellarators," *Physics of Fluids B: Plasma Physics*, vol. 4, pp. 2081–2091, Mar. 1992.

[60] H. Wobig, “The theoretical basis of a drift-optimized stellarator reactor,” *Plasma Physics and Controlled Fusion*, vol. 35, pp. 903–917, Aug. 1993.

[61] J. Nührenberg *et al.*, “Overview on Wendelstein 7-X theory,” *Fusion Technology*, vol. 27, pp. 71–78, Apr. 1995.

[62] A. Dinklage *et al.*, “Magnetic configuration effects on the Wendelstein 7-X stellarator,” *Nature Physics*, vol. 14, pp. 855–860, May 2018.

[63] C. D. Beidler *et al.*, “Successful reduction of neoclassical energy transport in the Wendelstein 7-X stellarator,” *Submitted to Nature Physics*.

[64] T. Stange *et al.*, “Advanced electron cyclotron heating and current drive experiments on the stellarator Wendelstein 7-X,” *EPJ Web of Conferences*, vol. 157, p. 02008, 2017.

[65] R. C. Wolf *et al.*, “Electron-cyclotron-resonance heating in Wendelstein 7-X: A versatile heating and current-drive method and a tool for in-depth physics studies,” *Plasma Physics and Controlled Fusion*, vol. 61, p. 014037, Nov. 2018.

[66] I. P. E. G. on Divertor, I. P. E. G. on Divert Database, and I. P. B. Editors, “Chapter 4: Power and particle control,” *Nuclear Fusion*, vol. 39, pp. 2391–2469, Dec. 1999.

[67] H. Renner *et al.*, “Physical aspects and design of the Wendelstein 7-X divertor,” *Fusion Science and Technology*, vol. 46, pp. 318–326, Sept. 2004.

[68] Y. Gao *et al.*, “Effects of toroidal plasma current on divertor power depositions on Wendelstein 7-X,” *Nuclear Fusion*, vol. 59, p. 106015, Aug. 2019.

[69] J. Fellinger *et al.*, “Integration of uncooled scraper elements and its diagnostics into Wendelstein 7-X,” *Fusion Engineering and Design*, vol. 124, pp. 226–230, Nov. 2017.

[70] M. Zanini *et al.*, “ECCD-induced sawtooth crashes at W7-X,” *Nuclear Fusion*, vol. 60, p. 106021, Sept. 2020.

[71] M. Krychowiak *et al.*, "Overview of diagnostic performance and results for the first operation phase in Wendelstein 7-X (invited)," *Review of Scientific Instruments*, vol. 87, p. 11D304, Oct. 2016.

[72] I. H. Hutchinson, *Principles of Plasma Diagnostics.* Cambridge University Press, July 2002.

[73] M. Bornatici *et al.*, "Electron cyclotron emission and absorption in fusion plasmas," *Nuclear Fusion*, vol. 23, pp. 1153–1257, Sept. 1983.

[74] M. Hirsch *et al.*, "ECE diagnostic for the initial operation of Wendelstein 7-X," *EPJ Web of Conferences*, vol. 203, p. 03007, 2019.

[75] U. Höfel *et al.*, "Bayesian modeling of microwave radiometer calibration on the example of the Wendelstein 7-X electron cyclotron emission diagnostic," *Review of Scientific Instruments*, vol. 90, p. 043502, Apr. 2019.

[76] U. Höfel, "Bayesian analysis of electron cyclotron emission measurements at Wendelstein 7-X," 2020.

[77] C. D. Michelis and M. Mattioli, "Soft-x-ray spectroscopic diagnostics of laboratory plasmas," *Nuclear Fusion*, vol. 21, pp. 677–754, June 1981.

[78] C. Brandt *et al.*, "Soft x-ray tomography measurements in the Wendelstein 7-X stellarator," *Plasma Physics and Controlled Fusion*, vol. 62, p. 035010, Jan. 2020.

[79] M. Anton *et al.*, "X-ray tomography on the TCV tokamak," *Plasma Physics and Controlled Fusion*, vol. 38, pp. 1849–1878, Nov. 1996.

[80] K. Brunner *et al.*, "Real-time dispersion interferometry for density feedback in fusion devices," *Journal of Instrumentation*, vol. 13, pp. P09002–P09002, Sept. 2018.

[81] E. Pasch *et al.*, "The Thomson scattering system at Wendelstein 7-X," *Review of Scientific Instruments*, vol. 87, p. 11E729, Sept. 2016.

[82] S. Bozhenkov *et al.*, “The Thomson scattering diagnostic at Wendelstein 7-X and its performance in the first operation phase,” *Journal of Instrumentation*, vol. 12, pp. P10004–P10004, Oct. 2017.

[83] W. Biel *et al.*, “Design of a high–efficiency extreme ultraviolet overview spectrometer system for plasma impurity studies on the stellarator experiment Wendelstein 7-X,” *Review of Scientific Instruments*, vol. 75, pp. 3268–3275, Sept. 2004.

[84] K. Rahbarnia *et al.*, “Alfvénic fluctuations measured by in-vessel Mirnov coils at the Wendelstein 7-X stellarator,” *Plasma Physics and Controlled Fusion*, Oct. 2020.

[85] K. Rahbarnia *et al.*, “Diamagnetic energy measurement during the first operational phase at the Wendelstein 7-X stellarator,” *Nuclear Fusion*, vol. 58, p. 096010, July 2018.

[86] Y. Turkin *et al.*, “Neoclassical transport simulations for stellarators,” *Physics of Plasmas*, vol. 18, p. 022505, Feb. 2011.

[87] N. Marushchenko, Y. Turkin, and H. Maassberg, “Ray-tracing code TRAVIS for ECR heating, EC current drive and ECE diagnostic,” *Computer Physics Communications*, vol. 185, pp. 165–176, Jan. 2014.

[88] R. Fitzpatrick, “Helical temperature perturbations associated with tearing modes in tokamak plasmas,” *Physics of Plasmas*, vol. 2, pp. 825–838, Mar. 1995.

[89] S. Mallat, *A Wavelet Tour of Signal Processing.* Elsevier, 2009.

[90] J. Canny, “A computational approach to edge detection,” *IEEE Transactions on Pattern Analysis and Machine Intelligence*, vol. PAMI-8, no. 6, pp. 679–698, 1986.

[91] *NRL Plasma Formulary.* U.S. Naval Research Laboratory, 2015.

[92] S. P. Hirshman and J. Whitson, “Steepest-descent moment method for three-dimensional magnetohydrodynamic equilibria,” *Physics of Fluids*, vol. 26, no. 12, p. 3553, 1983.

[93] A. Zocco *et al.*, "W7-X and the sawtooth instability. Part I: Towards realistic simulations of current-driven magnetic reconnection," *Submitted to Nuclear Fusion*, 2021.

[94] M. Ester *et al.*, "A density-based algorithm for discovering clusters in large spatial databases with noise," pp. 226–231, AAAI Press, 1996.

[95] R. Fischer *et al.*, "Sawtooth induced q-profile evolution at ASDEX Upgrade," *Nuclear Fusion*, vol. 59, p. 056010, Mar. 2019.

[96] E. Strumberger *et al.*, "Linear, resistive stability studies for wendelstein 7-x-type equilibria with external current drive," *Nuclear Fusion*, vol. 60, no. 10, p. 106013, 2020.

[97] Q. Yu *et al.*, "Numerical modeling of the electron temperature crashes observed in Wendelstein 7-X stellarator experiments," *Nuclear Fusion*, vol. 60, p. 076024, June 2020.

[98] T. D. de Wit *et al.*, "The biorthogonal decomposition as a tool for investigating fluctuations in plasmas," *Physics of Plasmas*, vol. 1, pp. 3288–3300, Oct. 1994.

[99] Y. Nagayama *et al.*, "Tomography of full sawtooth crashes on the Tokamak Fusion Test Reactor," *Physics of Plasmas*, vol. 3, pp. 1647–1655, May 1996.

[100] V. S. Udintsev *et al.*, "Experimental observation of m/n= 1/1 mode behaviour during sawtooth activity and its manifestations in tokamak plasmas," *Plasma Physics and Controlled Fusion*, vol. 47, pp. 1111–1136, July 2005.

[101] R. Kleiber *et al.*, "Modern methods of signal processing applied to gyrokinetic simulations," *Plasma Physics and Controlled Fusion*, vol. 63, p. 035017, Jan. 2021.

[102] G. Fuchert *et al.*, "Global energy confinement in the initial limiter configuration of Wendelstein 7-X," *Nuclear Fusion*, vol. 58, p. 106029, Aug. 2018.

[103] F. o. Pedregosa, “Scikit-learn: Machine learning in Python,” *Journal of Machine Learning Research*, vol. 12, pp. 2825–2830, 2011.

[104] P. J. Rousseeuw, “Silhouettes: A graphical aid to the interpretation and validation of cluster analysis,” *Journal of Computational and Applied Mathematics*, vol. 20, pp. 53–65, Nov. 1987.

Publications

Peer-reviewed publications as first author

1. M. Zanini, H.P. Laqua, H. Thomsen, T. Stange, C. Brandt, H. Braune, K.J. Brunner, G. Fuchert, M. Hirsch, J. Knauer, U. Höfel, S. Marsen, E. Pasch, K. Rahbarnia, J. Schilling, Y. Turkin, R.C. Wolf, A. Zocco and the W7-X Team, "ECCD-induced sawtooth crashes at W7-X", *Nuclear Fusion*, vol. 60, p. 106021, (2020).

   DOI: 10.1088/1741-4326/aba72b

   The publication provides a first study of the sawtooth crashes detected at the W7-X stellarator, during electron cyclotron current drive (ECCD) experiments. The sawtooth crashes are characterised by a fast drop of the core electron temperature. The joint analysis of the electron cyclotron emission and the x-ray tomography shows the crashes are often preceded by a fast displacement of the plasma core, consistent with a $(m, n) = (1, 1)$ structure, but sometimes weak precursors can also be observed. The crash evolution is unchanged during the discharge, but the amplitude and the time interval between two events is found to be not constant in time. Comparing the amplitude and the location of the crashes, we identified two types of crashes: one affecting the central part of the plasma and another, stronger, extending the crashed volume to about 50 % of the effective radius. No direct measurements of the toroidal current profile are available at W7-X. It is speculated that localised ECCD can significantly change the rotational transform, thus altering the plasma stability conditions. We developed a 1-D cylindrical code to estimate the time scales for rotational transform to cross low order rational values, which is found to be consistent with the experimental data.

   This work contributed to most of chapter 3 and part of chapter 4.

M. Zanini took part in the planning of the experiments, analysed the data and wrote the publication. A. Zocco contributed by writing part of section 5, regarding the 1-D cylindrical model. H.P. Laqua, T. Stange, R. Wolf, H. Thomsen, C. Brandt, K. Rahbarnia and A. Zocco contributed with fruitful discussions on the ECRH physics, mode analysis and sawtooth physics. Additional contributions are the following. Y. Turkin provided the bootstrap current calculations. H.P. Laqua, T. Stange and S. Marsen contributed as responsible of the ECRH heating system, M. Hirsch and U. Höfel contributed as main responsible of the electron cyclotron emission diagnostic. H. Thomsen, C. Brandt, J. Schilling contributed as main responsible of the x-ray tomography system. K. Rahbarnia contributed as main responsible of the magnetic diagnostics. E. Pasch and G. Fuchert contributed as responsible of the Thomson scattering diagnostic. J. Knauer and K.J. Brunner contributed as responsible of the dispersion interferometer. The final editing involved all the co-authors.

2. M. Zanini, B. Buttenschön, H. P. Laqua, H. Thomsen, T. Stange, C. Brandt, H. Braune, K. J. Brunner, A. Dinklage, Y. Gao, M. Hirsch, U. Höfel, J. Knauer, S. Marsen, N. Marushchenko, A. Pavone, K. Rahbarnia, J. Schilling, Y. Turkin, R. C. Wolf, A. Zocco and the W7-X team Team", "Confinement degradation and plasma loss induced by strong sawtooth crashes at W7-X", *Nuclear Fusion*, vol. 61, p. 116053, (2021).

   DOI: 10.1088/1741-4326/ac2870

   This work describes the effects that strong temperature crashes, detected during electron cyclotron current drive experiments, can have on the performance of W7-X plasmas. The work describes remarkable experiments in which temperature crashes lead to a strong degradation of the stored plasma energy and eventually to the premature termination of the experiment. It is speculated that the energy released during strong temperature crashes can ionise the neutrals/impurities at the plasma edge and this hypothesis is not contraddicted by the strong increase in signal, detected by the dispersion interferometer, soft x-ray cameras and the XUV spectrometers. A large and localised increase in x-ray emissivity is initially found at the plasma edge. The

XUV spectrometers suggest a strong influx of impurities. Due to the increased radiation losses, the plasma cools down and the stored energy drops on a time scale faster than the confinement energy time. Eventually, the increase in plasma resistance causes a fast dissipation of the toroidal current and, due to the poor coupling between the ECRH and the electrons, the experiment is terminated. We compare different ECCD experiments in which the dispersion interferometer detected an increase in density after a temperature crash and find that only the largest crashes are related to such density increase.

Most of this work is discussed in chapter 5 of this thesis.

M. Zanini took part in the planning of the experiments, analysed the data and wrote the publication. B. Buttenschön provided and analysed the XUV spectrometer data and helped write the corresponding section. H.P. Laqua, T. Stange, R. Wolf, H. Thomsen, C. Brandt, B. Buttenschön, N. Marushchenko, K. Rahbarnia ,Y. Turkin and A. Zocco contributed with fruitful discussions on the sawtooth physics, the impurity effects on the energy confinement and the role of relatively high toroidal current at W7-X. .P. Laqua, T. Stange and S. Marsen contributed as responsible of the ECRH heating system, M. Hirsch and U. Höfel contributed as main responsible of the electron cyclotron emission diagnostic. H. Thomsen, C. Brandt, J. Schilling contributed as main responsible of the x-ray tomography system. K. Rahbarnia contributed as main responsible of the magnetic diagnostics. J. Knauer and K.J. Brunner contributed as responsible of the dispersion interferometer. The final editing involved all the co-authors.

Peer-reviewed publications as co-author

In this section, the most relevant Peer-reviewed publications in which I contributed as co-author are highlighted.

1. Q. Yu, E. Strumberger, V. Igochine, K. Lackner, H.P. Laqua, **M. Zanini**, H. Braune, M. Hirsch, U. Höfel, S. Marsen, T. Stange, R.C. Wolf, S. Günter and the W7-X Team. “Numerical modeling of the electron temperature crashes observed in Wendelstein 7-X stellarator experiments,” *Nuclear Fusion*, vol. 60, p. 076024, (2020).

In this work the first author performs numerical calculations based on nonlinear two-fluid equations, in order to model the sawtooth crashes during ECCD experiments at W7-X. Using input parameters similar to the experiment, numerical calculations show two types of crashes of the central electron temperature depending on the growth of the internal kink mode coupled to double tearing modes.

M. Zanini contributed to the introduction of the publication,provided the experimental data. He also contributed to the discussion of the results in the light of the experimental results.

2. Y. Gao, J. Geiger, M. W. Jakubowski, P. Drewelow, M. Endler, K. Rahbarnia, S. Bozhenkov, M. Otte, Y. Suzuki, Y. Feng, H. Niemann, F. Pisano, A. Ali, A. Puig Sitjes, **M. Zanini**, H. P. Laqua, T. Stange, S. Marsen, T. Szepesi, D. Zhang, C. Killer, K. Hammond, S. Lazerson, B. Cannas, H. Thomsen, T. Andreeva, U. Neuner, J. Schilling, A. Knieps, M. Rack, Y. Liang and the W7-X Team. "Effects of toroidal plasma current on divertor power depositions on Wendelstein 7-X," *Nuclear Fusion*, vol. 59, p. 106015, Aug. 2019.

   In this work the first author presents experimental observations and simulations for the effects of toroidal plasma current on divertor power depositions on W7-X. It is shown how the toroidal current produces changes in the edge island geometry, which in turn results in a sweep of the strike line and a redistribution of the heat flux footprints. The author compares experiments in which the toroidal current is produced only by the bootstrap current with electron cyclotron current drive experiments and verifies that ECCD shows the same strike line changes as the experiments with the freely evolving current, i.e. bootstrap current alone. This suggests that ECCD may be a possible candidate for the strike-line control in the future.

   M. Zanini contributed to the planning of the ECCD experiments.

3. R. C. Wolf, S. Bozhenkov, A. Dinklage, G. Fuchert, Y. O. Kazakov, H. P. Laqua, S. Marsen, N. B. Marushchenko, T. Stange, **M. Zanini**, I. Abramovic, A. Alonso, J. Baldzuhn, M. Beurskens, C. D. Beidler, H. Braune, K. J. Brunner, N. Chaudhary, H. Damm, P. Drewelow, G. Gantenbein, Y. Gao, J. Geiger, M. Hirsch, U. Höfel, M.

Jakubowski, J. Jelonnek, T. Jensen, W. Kasparek, J. Knauer, S. B. Korsholm, A. Langenberg, C. Lechte, F. Leipold, H. Trimino Mora, U. Neuner, S. K. Nielsen,D. Moseev, H. Oosterbeek, N. Pablant, E. Pasch, B. Plaum, T. Sunn Pedersen, A. Puig Sitjes, K. Rahbarnia, J. Rasmussen, M. Salewski, J. Schilling, E. Scott, M. Stejner, H. Thomsen, M. Thumm, Y. Turkin F. Wilde and the W7-X Team. "Electron-cyclotron-resonance heating in Wendelstein 7-X: A versatile heating and current-drive method and a tool for in-depth physics studies," *Plasma Physics and Controlled Fusion*, vol. 61, p. 014037, Nov. 2018.

In this work the first author describes the ECRH system at W7-X. The main heating schemes used at W7-X as well as the power deposition effects are described. A description of the ECCD experiments is provided. In this section, the author discusses the main achievements of ECCD experiments for strike line control. He also outlines the main effects of ECCD on the plasma stability and the presence of central temperature crashes during ECCD experiments.

M. Zanini contributed to the planning of the ECCD experiments. He also contributed to discuss the implication of localised ECCD which are outlined in the corresponding section.

4. R. C. Wolf, A. Alonso, S. Äkäslompolo, J. Baldzuhn, M. Beurskens, C. D. Beidler, C. Biedermann, H.-S. Bosch, S. Bozhenkov, R. Brakel, H. Braune, S. Brezinsek, K.-J. Brunner, H. Damm, A. Dinklage, P. Drewelow, F. Effenberg, Y. Feng, O. Ford, G. Fuchert, Y. Gao, J. Geiger, O. Grulke, N. Harder, D. Hartmann, P. Helander, B. Heinemann, M. Hirsch, U. Höfel, C. Hopf, K. Ida, M. Isobe, M. W. Jakubowski, Y. O. Kazakov, C. Killer, T. Klinger, J. Knauer, R. König, M. Krychowiak, A. Langenberg, H. P. Laqua, S. Lazerson, P. McNeely, S. Marsen, N. Marushchenko, R. Nocentini, K. Ogawa, G. Orozco, M. Osakabe, M. Otte, N. Pablant, E. Pasch, A. Pavone, M. Porkolab, A. Puig Sitjes, K. Rahbarnia, R. Riedl, N. Rust, E. Scott, J. Schilling, R. Schroeder, T. Stange, A. von Stechow, E. Strumberger, T. Sunn Pedersen, J. Svensson, H. Thomson, Y. Turkin, L. Vano, T. Wauters, G. Wurden, M. Yoshinuma, **M. Zanini**, D. Zhang and the W7-X Team. "Performance of Wendelstein 7-X stellarator plasmas during the first divertor operation phase," *Physics of Plasmas*,

vol. 26, p. 082504, Aug. 2019.

In this work the first author describes the performance of W7-X plasmas during the first divertor operation phase. The author also outlines the main issues related to the application of localised ECCD, i.e. the presence of repetitive temperature crashes, which are analysed in detail in this thesis.

M. Zanini contributed to the planning of the ECCD experiments. He also contributed to discuss the implication of localised ECCD which are outlined in the corresponding section.

Acknowledgements

I would like to thank Prof. Dr. Robert Wolf for giving me the opportunity to carry out my Ph.D research at IPP. I appreciated the time and the support he gave me during his supervision. I would also like to thank Dr. Heinrich Laqua for his support and enthusiasm in this work. Although it turned out to be not exactly a thesis on ECRH physics, he always showed interest and proposed new ideas to improve this work. I think that a good supervisor is the one that knows when students should put an end to their work and I am grateful he reminded me several time to not get lost in details. My gratitude goes to Dr. Torsten Stange for the endless discussions and the several suggestions he proposed. I am deeply indebted to Dr. Matthias Hirsch for his patience and precious help regarding the interpretation of the ECE data. A special thanks also to Dr. Udo Höfel for the ECE mapping reconstructions. I am grateful to Dr. Henning Thomsen and Dr. Christian Brandt for providing the x-ray tomography and for the long and fruitful discussions regarding this topic. I extend my gratitude to Dr. Kian Rahbarnia for the long discussion regarding the Mirnov coil data and Dr. Tamara Andreeva for the discussions regarding VMEC and the field line tracing. My deepest gratitude to Dr. Valentine Igochine (IPP Garching) for his patience and for having taught me a lot regarding the physics of sawteeth. It was not always possible to apply the same methods for the W7-X data, but his suggestions have been extremely important for this work. The enthusiasm, curiosity and the deep theoretical knowledge of Dr. Alessandro Zocco have been crucial for the completion of this work and I am extremely grateful for this. A special thanks goes to Dr. Kai Jakob Brunner, who helped me at the beginning of this journey to get started.

I would like to thank several people I met during these four years. Directly or indirectly they contributed to this work and therefore I would like to thank Alëna G., Andrea T., Andrei G., Carlos M. M., Francesco V., Nerea P., Jorrit L., Sara M., Primoz P. and Andrea M.. My gratitude goes to Marco K., who helped me in different occasions. I would like to thank my office mates Jan Paul K., Neha C. and Juan G.A. for their company, the coffee/tea breaks and the spanish lessons. I would like to thank Annabelle S. for her friendship and for being an (almost) infinite source of happiness and Linda P. for having withstand the complaints of mine in these last months of writing. Furthermore, a special thanks to my friends Tiziano F. and Fabian W.. Your friendship and the time spent in Greifswald meant a lot. Tiziano, thanks for having found our Alice. Fabian, thanks for all the covfefe.

I would also like to mention several friends, not directly related to the institute, but equally important. Thanks to Giulia Antonia R. for the database of horrible photos and for the evenings spent singing stupid songs. Thanks to Anna I. for your support and help in different situations. We have to go to Azores for our birthday, do not forget it. Thanks to whole Italian community. In particular to Corinna Maria G., for the indisputably useful complaints about the weather, Eleonora H. and Marc S. Yes, you were naturalised.

Thanks to Anna F. (my german has really improved with your help) and Annett E. (you are an exceptional cat sitter).

Thanks to Isabella M. and Federico d'I. for the Catan evenings, to Pier S.R. for having managed to reach Greifswald, to Nicoló C. and Alice B. for their support. Thanks to Gianluca G., *un giovanotto interessante, nonostante ancora in lutto per la punta del compasso.*

Finally, I would like to thank my family for their support. Of course, the biggest thank you goes to my love, Margherita. I am indebted for all the support you have given me during this thesis and the others. In these years, we shared so many adventures and happy moments and many to come.